

Chemical-Mechanical Polishing of Tungsten: Electrochemical and Tribocorrosion Approach

THÈSE N° 4427 (2009)

PRÉSENTÉE LE 12 JUIN 2009

À LA FACULTÉ SCIENCES ET TECHNIQUES DE L'INGÉNIEUR
LABORATOIRE DE MÉTALLURGIE CHIMIQUE
PROGRAMME DOCTORAL EN SCIENCE ET GÉNIE DES MATÉRIAUX

ÉCOLE POLYTECHNIQUE FÉDÉRALE DE LAUSANNE

POUR L'OBTENTION DU GRADE DE DOCTEUR ÈS SCIENCES

PAR

Jelena STOJADINOVIC

acceptée sur proposition du jury:

Dr D. Damjanovic, président du jury
Dr S. Mischler, Prof. M. Declercq, directeurs de thèse
Prof. C. Comninellis, rapporteur
Dr E. Jacquinot, rapporteur
Prof. M. M. Stack, rapporteur



ÉCOLE POLYTECHNIQUE
FÉDÉRALE DE LAUSANNE

Suisse
2009

Acknowledgments

Firstly, I would like to thank my thesis director, Dr Stefano Mischler and co-director Prof. Michel Declercq, for providing me the opportunity of performing this work. I am also grateful to Dr Stefano Mischler for his guidance, encouragement during my thesis work, and for teaching me so much.

I would like to thank Dr Didier Bouvet from General Electronics Laboratory 1 at EPFL, for his many useful suggestions and ideas during our meetings. Further thanks are due to Dr Eric Jacquinet and Michael Meier from AZ Electronic Materials for providing me the information regarding industry requirements during our regular discussions.

I would like to thank the members of my thesis jury: Prof. Margaret Stack from University of Strathclyde, Glasgow, Dr Eric Jacquinet from AZ Electronic Materials, Prof. Christos Comninellis from EPFL, and the president of jury Prof. Dragan Damjanović.

I would like to thank the current and ancient members of LMCH for all their help over the last four years. I would like to acknowledge: Prof. D. Landolt for useful discussions, Dr Samuel Debaud who introduced me in the field of corrosion testing; Nicolas Xanthopoulos for XPS and AES analyses and his constant good humour; Pierre Mettraux for SEM analysis and for solving computer problems and Jean Daniel Neuvécelle for general help in the lab. Special thanks to Mrs Nadia Ruch and Mrs Sylvie Vaucher for their time, effort and kindness in handling the administrative part. Not least, I would like to thank my office mate Julian Perret, for many useful tribocorrosion discussions during our academic research and a pleasant office atmosphere. I am grateful to all the members of the Materials Department workshop for building my designs and for helpfully suggesting ways to improve them.

Many thanks for all my friends from Material Institute and the whole EPFL for a wonderful atmosphere which helped us to deal with scientific challenges. Also, many thanks to my grandma, family, and friends back home for their encouragement.

Finally, thanks to my parents and my sister for all their love and support.

Abstract

The chemical-mechanical polishing process (CMP) is an essential part of the production of integrated circuits. Metal to be polished in the CMP reacts with the oxidants from the aqueous suspension (slurry) and the passive film is formed on the metal surface. Suspended abrasive nano particles from the slurry cause detachment of the formed friable passive films.

The CMP represents the tribocorrosion process where material deterioration results from the interaction of wear and corrosion which takes place in tribological contact exposed to an aggressive environment. Due to increasing number of the materials to be polished in the modern integrated circuits it is necessary to gather fundamental understanding of the removal mechanism of each material.

The aim of this work is to elucidate the removal mechanisms of tungsten (W), as a typical microelectronic metal (chosen as a model system), under different oxidising conditions (represented by electrochemically imposed potential). Also, we want to evaluate the effect of the slurry composition (chelating agents lactic and phosphoric acid) on material removal.

To achieve this electrochemical techniques (chrono amperometry, cyclic voltametry, passivation kinetics measurements under mass transport control), and tribocorrosion techniques (tests on tribometer with electrochemical cell with reciprocating sliding motion of alumina ball) were used. Surface analysis techniques (SEM, XPS, AES) were used to assess worn and unworn surfaces' morphology and chemistry. In addition, electrochemical tests and polishing tests on the CMP machine were performed with technical CMP slurries.

The sliding action of the alumina ball on tungsten in the 0.01 M H₂SO₄ solution was found to cause three distinct wear responses depending on imposed electrode potential. Below the first threshold potential the wear is low due to negligible oxide film formation. In the following wear region, up to the second threshold potential, materials deterioration in the rubbed area proceeds by cyclic mechanical removal of the WO₃ passive film followed by repassivation of tungsten. The amount of anodic oxidation corresponds to the

overall removed metal volume. Beyond the second threshold potential a compact tribolayer of WO_3 (more than 400 nm thick), probably formed by agglomeration of oxide particles detached from the metal surface, forms and covers the wear track. Similar tribocorrosion behavior of tungsten was also observed in the presence of 0.1 M H_3PO_4 .

The presence of chelating agents, lactic acid and phosphoric acid, in the 0.01 M H_2SO_4 solution does not change the volume of material wastage at potentials below the second threshold potential. Beyond this electrode potential, lactic acid promotes WO_3 dissolution and thus impedes the third body formation and enhances wear.

Electrochemical factors have a strong influence on the tungsten CMP removal rate. It was found that CMP removal rate increases with the open circuit potential (electrode potential) and with passivation charge density.

A good correlation of tribocorrosion results and CMP practice was observed. Tribocorrosion models can be successfully applied to the tribocorrosion of tungsten and as well can be fairly used for modelling the material removal in CMP.

Key words: Tribocorrosion, Tungsten, CMP, Electrochemistry, Passivation

Version Abrégée

Le procédé de polissage mécano-chimique (CMP – Chemical Mechanical Polishing) est devenu indispensable à la fabrication des circuits intégrés pour des technologies sub-microniques. Nous distinguons 2 types de polissages: le polissage des diélectriques (TEOS, BPSG, HDP ...) et le polissage des métaux (Ti, TiN, W, Cu ...). Dans le cas des diélectriques, le polissage est principalement contrôlé par les aspects mécaniques (concentration d'abrasif et pression de polissage), par contre pour le polissage des métaux, les mécanismes de polissage sont beaucoup plus subtils. En effet, pour la majorité des métaux, le polissage résulte d'une réaction avec des oxydants contenus dans le liquide de polissage (slurry) générant un film passif sur la surface métallique. Ce film passif friable est ensuite détaché de la surface métallique par les nanoparticules abrasives suspendues dans la solution. D'un point de vue purement scientifique, le polissage du métal résultant d'une usure du matériau associé à des phénomènes de corrosion est assimilable à un processus de tribo-corrosion.

Le but de ce travail est de comprendre les mécanismes d'enlèvement au cours du polissage en prenant comme matériau d'étude le tungstène (W), métal largement employé en microélectronique. Une attention particulière est portée sur la formation (nature chimique et épaisseur) de l'oxyde de tungstène en fonction des conditions d'oxydation avec l'utilisation de potentiels électro-chimiquement imposés. Dans un deuxième temps, l'influence de la nature d'agents chélatants, acides lactique et phosphorique, sur le taux d'enlèvement du matériau a été étudié.

Dans cette optique, des techniques électrochimiques (chrono - ampérométrie, voltamétrie cyclique, mesure de la cinétique de passivation sous contrôle de transport de masse), et des techniques de tribo-corrosion (essais sur le tribomètre "bille-sur-disque" avec la cellule électrochimique) ont été utilisées. Les techniques d'analyse SEM, XPS et AES ont été employées pour évaluer la morphologie et la chimie des surfaces usées et non usées. Enfin, des essais électrochimiques et de polissages sont réalisés sur machine CMP avec des solutions de tests.

L'action du glissement de la bille d'alumine sur le tungstène dans une solution de H_2SO_4 0.01 M a mis en évidence trois régions distinctes d'usure selon le potentiel d'électrode imposé. Au dessous d'un premier potentiel seuil, l'usure est faible parce que la formation d'oxyde est négligeable. Dans la région d'usure suivante, (du premier au deuxième potentiel seuil), la détérioration du matériau dans la trace d'usure résulte de l'enlèvement cyclique du film WO_3 passif, suivi d'une repassivation du tungstène. La quantité d'oxydation anodique correspond au volume d'usure global du métal. Au delà du deuxième potentiel seuil, une tribo-couche compacte de WO_3 (plus de 400 nanomètres d'épaisseur) se forme par agglomération des particules d'oxyde détachées de la surface du métal, et recouvre la trace d'usure. Le même comportement est observé en présence de 0.1 M H_3PO_4 .

La présence d'agents chélatants (acide lactique et acide phosphorique) dans la solution de 0.01 M H_2SO_4 , ne change pas le volume d'usure pour des potentiels inférieurs au deuxième seuil. Au delà de ce potentiel, l'acide lactique favorise la dissolution de WO_3 , empêche la formation du troisième corps (tribo-couche) et augmente l'usure.

Les facteurs électrochimiques ont une influence déterminante sur le taux d'enlèvement du tungstène au cours du procédé de polissage. Il a été constaté que le taux d'enlèvement augmente avec le potentiel en circuit ouvert (potentiel d'électrode) et avec la densité de charge de passivation.

Enfin, une bonne corrélation entre les résultats de tribo-corrosion et les vitesses de polissage sur machine CMP a été observée. Cela a permis de développer des modèles de tribo-corrosion du tungstène applicable à la modélisation de l'enlèvement du tungstène par CMP.

Mots-clés: Tribocorrosion, Tungstène, CMP, Électrochimie, Passivation

Table of Contents

1. INTRODUCTION	1
2. LITERATURE REVIEW	5
2.1. CHEMICAL – MECHANICAL POLISHING	5
2.2. CORROSION OF TUNGSTEN	9
2.3. TRIBOLOGY	19
2.4. TRIBOCORROSION	22
2.4.1. <i>Modelling Tribocorrosion</i>	26
2.4.2. <i>Chemical and Electrochemical Effects in the CMP and Tribocorrosion of Tungsten</i>	29
2.5. RATIONALE OF THE THESIS	34
3. ELECTROCHEMICAL BEHAVIOR OF TUNGSTEN IN H₂SO₄ SOLUTIONS	37
3.1. EXPERIMENTAL TECHNIQUES	37
3.1.1. <i>Electrochemical Experiments</i>	37
3.1.2. <i>Surface Characterisation</i>	41
3.2. RESULTS	43
3.2.1. <i>Passivation Behavior of Tungsten in Different Solutions. Potentiodynamic Polarization</i>	43
3.2.2. <i>Potentiostatic Polarization</i>	44
3.2.3. <i>Passivation Transients</i>	49
3.2.4. <i>Passive Film Composition and Thickness</i>	55
3.3. DISCUSSION	61
3.4. CONCLUSIONS	66
4. EFFECT OF EXPERIMENTAL PARAMETERS IN TRIBOCORROSION	67
4.1. TRIBOCORROSION EXPERIMENTS	67
4.2. CATHODIC CLEANING PRE-TREATMENT	72

Table of Contents

4.3. DURATION OF RUBBING	76
4.4. DURATION OF PASSIVATION	78
4.5. FREQUENCY OF RUBBING	79
4.6. NORMAL LOAD	80
4.7. STANDARD TEST CONDITIONS	82
5. INFLUENCE OF ELECTRODE POTENTIAL ON THE TRIBOCORROSION OF TUNGSTEN IN SULPHURIC ACID	83
5.1. EXPERIMENTAL TECHNIQUES	83
5.2. RESULTS	84
5.2.1. <i>Friction Behavior</i>	84
5.2.2. <i>Current in Tribocorrosion Tests</i>	85
5.2.3. <i>Mass Transport Effects in Tribocorrosion Experiments</i>	88
5.2.4. <i>Wear Track Characterisation</i>	92
5.3. DISCUSSION	100
5.4. CONCLUSIONS	103
6. INFLUENCE OF THE CHELATING AGENTS ON THE TRIBOCORROSION OF TUNGSTEN IN SULPHURIC ACID	105
6.1. EXPERIMENTS	106
6.2. RESULTS	106
6.2.1. <i>Influence of the Chelating Agents on the Friction Behavior and Current During Rubbing</i>	106
6.2.2. <i>Influence of the Chelating Agents on the Mass Transport Effects in Tribocorrosion Experiments</i>	109
6.2.3. <i>Wear Track Characterisation</i>	111
6.3. DISCUSSION	118
6.4. CONCLUSIONS	121
7. TUNGSTEN ELECTROCHEMICAL PARAMETERS AND REMOVAL RATES IN THE CMP PRACTICE	123
7.1. EXPERIMENTAL TECHNIQUES	123
7.1.1. <i>Electrochemical Experiments</i>	123
7.1.2. <i>Polishing on the CMP Machine</i>	124

Table of Contents

7.2. RESULTS	126
7.2.1. <i>Open Circuit Potential Measurements for Technical CMP Slurries</i>	126
7.2.2. <i>Passivation Kinetics for Technical CMP Slurries</i>	127
7.3. DISCUSSION	129
7.4. CONCLUSIONS	134
8. GENERAL DISCUSSION	135
8.1. MODELLING OF TRIBOCORROSION OF W IN 0.01 M H ₂ SO ₄	135
8.2. CORRELATION OF TUNGSTEN TRIBOCORROSION RESULTS AND CMP PRACTICE	143
8.3. MODELLING OF TRIBOCORROSION IN CMP	146
8.4. CONCLUSIONS	151
9. CONCLUSIONS	153
9.1. CONTRIBUTION OF THIS WORK	153
9.2. OUTLOOK	156
10. REFERENCES	157
APPENDIX A: OHMIC DROP INFLUENCE	161
APPENDIX B: TUNGSTEN SAMPLES PREPARATION PRIOR TO TRIBOCORROSION EXPERIMENTS	163
APPENDIX C: HERTZIAN INITIAL POINT CONTACT AND PRESSURE	164

CHAPTER 1

1. Introduction

Tribocorrosion is a material deterioration process which results from the interaction of wear and corrosion, taking place in tribological contact exposed to aggressive environment [1]. The lifetime and performance of many mechanical devices, such as orthopaedic implants, food processing equipment and pumps for chemicals, are limited by tribocorrosion. However, in some applications tribocorrosion can be conveniently used for manufacturing and finishing purposes, as in the chemical-mechanical polishing (CMP) process, used in the fabrication of integrated circuits.

Integrated circuits are produced by deposition and modification of different oxide and metal layers on a silicon wafer. Since the year 1991, the CMP of each deposited layer has become an essential part of integrated circuits (IC) production.

The number of materials found in modern integrated circuits is constantly increasing. The adjustment of the parameters controlling material removal (oxidizing power of the slurry, chelating agents) to different metals to be polished requires a fundamental scientific approach. It involves the understanding of the relevant tribocorrosion phenomena and the identification of critical mechanical and (electro-) chemical factors. In this study, tungsten as a typical microelectronic metal, subjected to the process of chemical - mechanical polishing (CMP), was chosen as a model system.

In the CMP process suspended abrasive nano particles cause detachment of friable surface layers formed by reaction between the oxidizing aqueous suspension (slurry) and the material to be polished [2][3]. Oxidizing agents and chemical additives such as

chelating agents are added to the slurry in order to obtain better removal rate and surface finish. Removal rate (RR) is defined as the average thickness change of a deposited layer during polishing on the CMP machine divided by polishing time. Kaufman's mechanism [4] explains the removal of specific metals used in microelectronics. It describes the material removal in the CMP as a cyclic sequence of abrasion of the passive oxide film covering the metal (depassivation) followed by anodic oxidation of the bare metal exposed to the oxidizing slurry (repassivation). By adjusting the oxidizing power of the CMP slurry it is possible to increase the thickness of the passive oxide film formed on the metal and to accelerate the material removal rate and thus the CMP process rate. The electrode potential (electric potential difference between metal electrode and electrolyte) is a relevant factor directly related to the oxidising properties of the slurry, which in turn depends on the nature and concentration of the oxidising agents, on the pH and on the temperature. In particular we want to elucidate the effect of the electrode potential and solution chemistry (chelating agents) on the tribocorrosion mechanisms of tungsten, as a typical microelectronic metal, using the combination of electrochemical, tribocorrosion and CMP techniques. This is expected to help developing the scientific criteria for the optimization of the CMP slurries.

The literature will be reviewed first (Chapter 2) in order to fix the state of the art in the field of corrosion and tribocorrosion of tungsten and to review the present understanding of the CMP process.

Electrochemical behavior of tungsten in 0.01 M H_2SO_4 , whose pH corresponds approximately to the technical CMP slurries' pH, will be studied in Chapter 3. Passivation kinetics during the oxide formation and the composition and thickness of the formed oxides on tungsten surface will be studied. The electrochemical behavior will be characterised using potentiodynamic, quasi potentiostatic polarization and potential step techniques combined with rotating disk electrodes (RDE), to control mass transport. Also, the corrosion behavior of tungsten in the presence of different chemicals (chelating agents) in the slurry composition, such as lactic acid ($C_3H_6O_3$) and phosphoric acid (H_3PO_4) will be studied.

A complete description of the experimental set-up for the tribocorrosion testing will follow in Chapter 4. In order to optimize the tribocorrosion testing technique, the influence

of experimental parameters on the test output values will be investigated and the standard experimental procedure will be defined.

The effect of imposed electrode potential on the tribocorrosion behavior of tungsten in 0.01 M H₂SO₄ will be presented in Chapter 5. For this a model tribological system involving an alumina ball sliding against a tungsten plate kept under electrochemical potential control will be used. Surface analysis techniques (XPS, AES) will be used as auxiliary techniques to assess surface chemistry. The laser profilometry, optical microscopy and SEM will serve to assess the surface topography and morphology.

The influence of solution chemistry i.e. the presence of C₃H₆O₃ and H₃PO₄ on the tribocorrosion behavior of tungsten will be evaluated in Chapter 6. Tungsten electrochemical parameters for the technical CMP slurries and the removal rates on the real CMP machine will be investigated in Chapter 7.

The application of existing electrochemical models of passivation phenomena to the tribocorrosion of tungsten will be presented in Chapter 8. The correlation between tungsten tribocorrosion and CMP practice was established, which helped applying tribocorrosion models to the CMP process.

Finally, Chapter 9 provides the conclusions resulting from this work.

CHAPTER 2

2. Literature Review

The aim of this literature review is to give an overview of the current understanding of the mechanisms of tungsten removal in the chemical-mechanical polishing. Firstly, the CMP phenomena will be depicted. The state of the art in the corrosion of tungsten and the theoretical overview of the wear mechanisms will be followed by the tribocorrosion part, including the tribocorrosion phenomena, techniques and existing models. Finally, the objective of this work will be described with the respect to the present understanding of the chemical and electrochemical effects in the CMP and to the tribocorrosion of tungsten.

2.1. Chemical – Mechanical Polishing

Chemical-mechanical process (CMP) is a tribocorrosion process where material loss or transformation is a result of simultaneous action of wear and corrosion. [5]

Integrated circuit (IC) is produced by deposition and modification of different metals layers (Figure 2.1). The IC density is constantly increasing and the dimensions are decreasing. Therefore, instead of building a chip in the form of a printed circuit board with wires taking up most of the chip area, the patterned metal layers are placed above the chip. The layers are separated by insulators creating multilevel interconnect system required for high-density integrated circuits. This is the one of the reasons for introducing the planarization into IC fabrication process. Other reasons are related to the fact that the optimal photolithography is achieved on flat surfaces and also planarization is necessary

for shallow trench isolation and damascene technologies [3]. Two terms have been used in this field, the Chemical-Mechanical Planarization and the Chemical-Mechanical Polishing. The Chemical-Mechanical Planarization is related to the polishing for the purpose of planarizing integrated circuit structures and other microelectronic devices. The Chemical-Mechanical Polishing is a more general term, including traditional polishing for example optics, semiconductor wafer preparation and metal polishing. Both terms are used for integrated circuits applications.

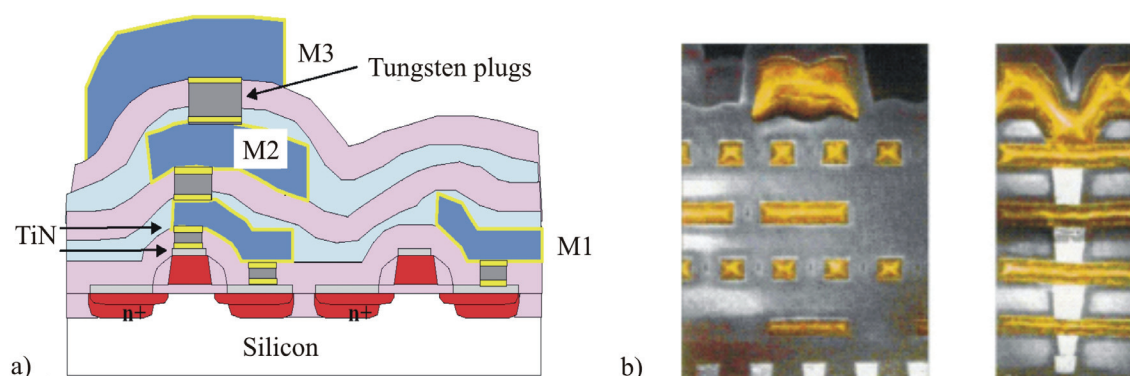


Figure 2.1 Schema of the integrated circuit produced: a) without CMP process and b) using the CMP process. [3]

The IBM was the first to introduce the CMP process in the micro-electronic industry (IC fabrication) in 1990's when the number of metal layers was 2. Nowadays this number increased to 9. In the recent time, the overall market for the CMP is growing at a rate of ~50% per year. This tempo of process integration far exceeds the fundamental understanding of interactions among the equipment, consumables and process parameters [6]. Materials that undergo CMP process are: dielectrics (the famous in this group is SiO_2), metals W, Cu, Cu alloys, Al, Al alloys, then Ti, TiN, Ta, TaN (which are used for barrier layers), superconductors, ferroelectrics, and high k dielectrics.

Three main elements of the CMP system are wafer, pad and slurry (Figure 2.2). A rotating wafer is pressed against a rotating polishing pad. An aqueous suspension of abrasive (slurry) is supplied to the wafer surface by pad. The wafer surface reacts with chemicals in the slurry and is abraded by slurry particles. Chemistry alone will not achieve planarization because most chemical reactions are isotropic. [7] Mechanical action alone, should theoretically, achieve the planarization but this is not desirable because of the

extensive associated damage of the material surface. [8] Therefore, a combination of chemical and mechanical effects is convenient for the removal of the material from the wafer surface. [3] Chemical action is taken by oxidants from the slurry which enhance metal dissolution and control passivation (formation of the protective layer on metal surface) in metal CMP. Oxidants used in the CMP process are usually H_2O_2 , KIO_3 and $Fe(NO_3)_3$. Abrasive particles from the slurry perform mechanical action through polisher rotation and pressure. Slurry abrasives are silica (fumed and colloidal), alumina or ceria particles. Mean diameter of the spherical colloidal particles in the abrasive slurries is in the range from a few tens up to a few hundreds of nm. They are much smaller than pad asperities and fluid thickness which are in the range of tens of microns. Additives as chelating agents, lactic [9], phosphoric acid [10] and potassium pyrophosphate are added to slurries in order to improve the removal rates and surface finish.

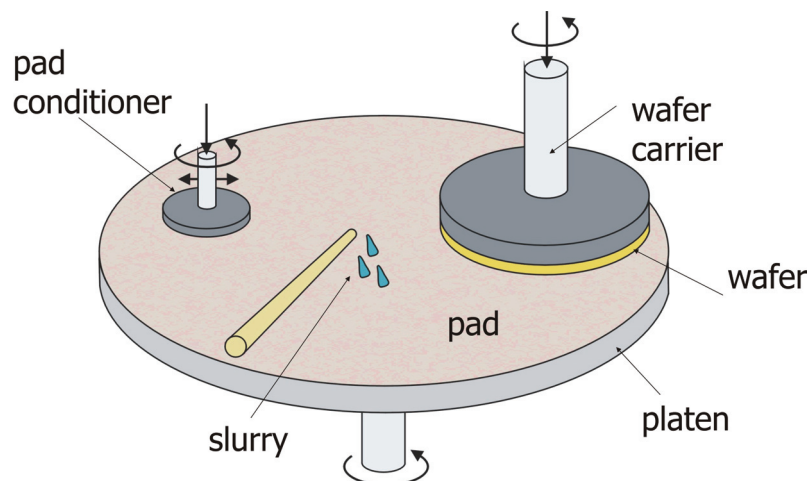


Figure 2.2 Schema of polishing on the CMP machine.

Pads are made of cast polyurethane foam, with a thickness of 1-3 mm. Pads wear out quickly (100-1000 wafers can be polished with one pad). Harder pads cause higher removal rates and higher defect densities. Since pad also experiences abrasive wear, a rotating tool, conditioner with diamond-covered face maintains pad surface roughness, counteracting abrasive wear, removing debris and exposing new pad surface.

The removal mechanisms in the CMP process vary with the type of material. [3] The generally accepted removal mechanism for the majority of the metals in the CMP (Figure 2.3) is proposed by Kaufman. [4] The passive film is formed on the metal surface as a

result of the reactions between the chemicals and the metallic surface. The oxide film is removed by mechanical abrasion due to the contact with the polishing pad and slurry abrasives. The next step represents the repassivation of the mechanically activated metal surface. However, the repassivation takes a finite time during which metal dissolution (corrosion) occurs. Through a repetitive process of the oxide film formation, removal and reformation, the global planarization of the metal is achieved.

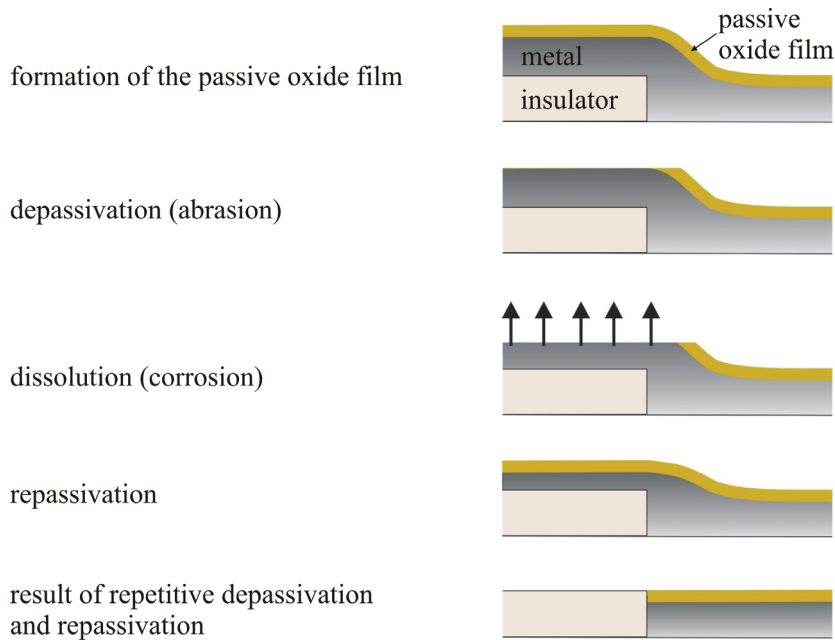


Figure 2.3 Schema of the material removal in the CMP according to Kaufman's mechanism.

Removal rate (RR) is an important parameter for the CMP process. As mentioned in Chapter 1, it represents an average thickness change during polishing divided by polishing time. Preston's empiric equation expresses removal rate as proportional to the applied downward pressure, P , and linear velocity of the wafer relative to the polishing pad, V [3]:

$$RR = K_p PV \quad (2.1)$$

In this equation K_p is the Preston coefficient, which is inversely proportional to elastic modulus of the material being polished. Increase in pressure and platen speed results in a linear increase in removal rate, according to Preston's equation.

Other parameters influencing *RR*, besides pressure and platen speed, are related to three main elements of the CMP system (wafer, pad and slurry). Parameters concerning slurry are: slurry chemistry (pH, buffering agents, oxidizers, chelating agents, and concentration), abrasives in the slurry (type, dimensions, concentration, and suspension stability), slurry flow rate (150-300 ml/min), and temperature ($5 \times RR / 20^\circ\text{C}$).

2.2. Corrosion of Tungsten

Tungsten (or wolfram), W, is a metal with atomic number 74. It is a very hard metal (Vickers hardness 3.4 GPa), with the atomic mass of 183.84 g/mol and density of 19.25 g/cm³. Tungsten can be found in ores such as wolframite, scheelite and others. The Young's modulus and Poisson's ratio of tungsten are 411 GPa and 0.28, respectively. Besides its high hardness, tungsten is also well known for its high melting point and resistance against oxidation and corrosion. [11]

In the pure form, tungsten is mainly used in electrical and microtechnique applications. Its compounds are widely used in many applications such as in light bulb filaments, X-ray tubes and in superalloys.

Tungsten is a corrosion resistant metal, because of the formation of a passive oxide films on the metal surface. The notions of the corrosion and passivity phenomena will follow before providing the state of the art of the tungsten passive film formation and dissolution (corrosion).

Corrosion

Corrosion of the metal is the spontaneous reaction between metal and its environment (gas, aqueous solution, dissolved salt) and happens simultaneously with reduction of the oxidant. In the system metal/environment often many reactions occur simultaneously and that system is classified as the mixed electrodes system. A classic corrosion reaction is the reaction of the metal oxidation (metal W, Fe, Zn, Al...) in an acid solution. Two electrode reactions (partial reactions) are observed, anodic (Equation 2.2) and cathodic reaction (Equation 2.3):



In the system of the mixed electrodes (Equations 2.2 and 2.3) the total current density, i , at the metal-solution interface is equal to the sum of anodic (i_a) and cathodic (i_c) partial current densities of the two electrode reactions:

$$i = i_a + i_c \quad (2.4)$$

Electrode Potential

The equilibrium potential or the reversible potential (E_{rev}) of an electrode is the difference in electric potential between an electrode and the electrolyte in which the electrode is immersed at equilibrium. Electrode potentials are always measured in respect to a reference electrode whose potential is known on an arbitrary scale. The Nernst equation permits the calculation of E_{rev} for the electrodes at equilibrium ($M^{n+} + ne^{-} = M$) [12]:

$$E_{rev} = E^{\circ} + \frac{RT}{2F} \ln a_{M^{n+}} \quad (2.5)$$

where E° is the standard potential of the metal electrode, R is the gas constant, T is the temperature, F is the Faraday's constant (96485 C/mol), n is the oxidation valence and $a_{M^{n+}}$ is the activity of the oxidized species. If we assume that the activity corresponds to the concentration $c_{M^{n+}}$ (diluted solutions), and also take the T as equal to 25°C, after conversion to log base, the Nernst equation will become:

$$E_{rev} = E^{\circ} + \frac{0.059}{2} \log c_{M^{n+}} \quad (2.6)$$

The electrode potential spontaneously acquired by metal in a corrosive environment, which contains oxidizing agents H^{+} or O_2 , in open circuit conditions is the open circuit potential (OCP). In open circuits conditions the current value is equal to zero. For a single

electrode, the open circuit potential is equivalent to the equilibrium potential E_{rev} . The open circuit potential of a mixed electrode undergoing corrosion is called the corrosion potential, E_{cor} . Its value is situated in between the equilibrium potentials of the partial electrode reactions. The equilibrium potential is thermodynamic quantity while a corrosion potential is determined by kinetics. The E_{cor} depends on the rates of anodic and cathodic partial reactions. Changes in corrosion potential can give an indication of active/passive behavior of the metal. When viewed in the context of Pourbaix diagrams [13], the corrosion potential can additionally give a fundamental indication of the thermodynamic corrosion risk. Factors that influence corrosion potential are: concentration and nature of the oxidizing agents, reaction kinetics, mass transport conditions, corrosive environment characteristics, metal properties, temperature, surface film layer formation, galvanic contact with other metals etc.

Passivity

In practice, many metals form an oxide layer on their surface as they corrode. If the oxide layer inhibits further corrosion, the metal is said to passivate. When these films are formed, the corrosion rate may decrease by several orders of magnitude. The formation process of the above-described film is called *passivation*. [12] The surface becomes passive for its environment with increase of the aggressive properties of the environment (increased concentration of oxidizing agents). A thin (few nm) dense oxide layer at the surface of passive metals prevents contact of the metal with the electrolyte leading to rapid dissolution.

During the dissolution of an active metal (active dissolution) the charge transfer takes place at the interface metal-electrolyte. Active dissolution reaction shows that soluble ions are formed and dissolved into electrolyte, according to the reaction (2.2). The released electrons may flow towards the cathode or may be taken by an oxidizing agent. The dissolution of a passive metal (passive dissolution) involves cations formed by a charge transfer reaction at the metal-film interface. The cations migrate through the passive film to the film-electrolyte interface. There they dissolve into solution in the form of hydrated or complexed ions. The charge number may be different for active and passive dissolution depending on metal, but the overall stoichiometric equation is the same for both types of dissolution.

The polarization curves represent the total current, the sum of the anodic and cathodic currents, measured after sweeping the potential of the metal electrode by potentiostat. Figure 2.4 shows the anodic partial current density of passivating metal as a function of potential. Polarization behavior of passivating metals can be described using the quantities of passivation potential, E_p (separates active from passive region), passivation current density, i_p (current density at the maximum), passive current density, i_{pp} (dissolution behavior of the metal in the passive potential region) and the transpassivation potential, E_b (transition from passive to transpassive region). The dissolution rate of a passive metal at a given potential is much lower than that of an active metal. The rate of dissolution decreases abruptly during passivation after reaching the current density maximum point i_p corresponding to the end of active dissolution region. For some materials in particular environments, it is not possible to form passive films for corrosion protection (iron in HCl solution). In this case, the corrosion rate continues to increase with increasing oxidizing conditions.

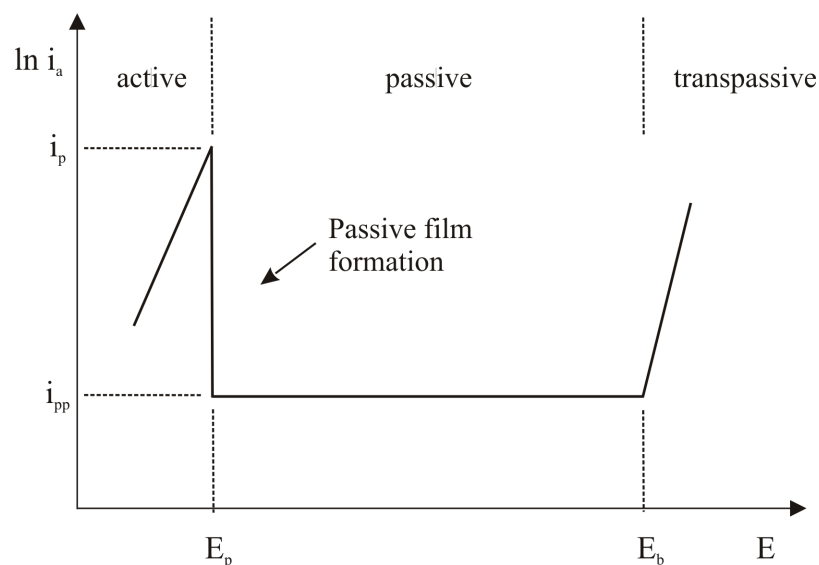


Figure 2.4 Variation of partial anodic current density with potential for a passivating metal. [12]

Growth and Dissolution of Tungsten Passive Films

Tungsten forms a wide range of oxides. [14] Its most stable oxide is WO_3 , with a molecular mass of 231.85 g/mol and the density of 7.16 g/cm³. Other nonstoichiometric oxides formed on tungsten are mostly result of thermal oxidation of tungsten or reduction

treatments of WO_3 . [15][16] According to Figure 2.5 and confirmed by experiments, tungsten is hardly corroded by most acid solutions, only the complexing acids attack it. [13] The CMP process of tungsten involves the slurries with the pH 2. At this pH, according to Pourbaix diagram, tungsten surface should passivate through the formation of either WO_2 , W_2O_5 or WO_3 . [13] Akonko [17] showed that the dominant oxidation state of W in passive films formed in acidic solution is 6+, while lower valence oxides can be observed at higher pH values.

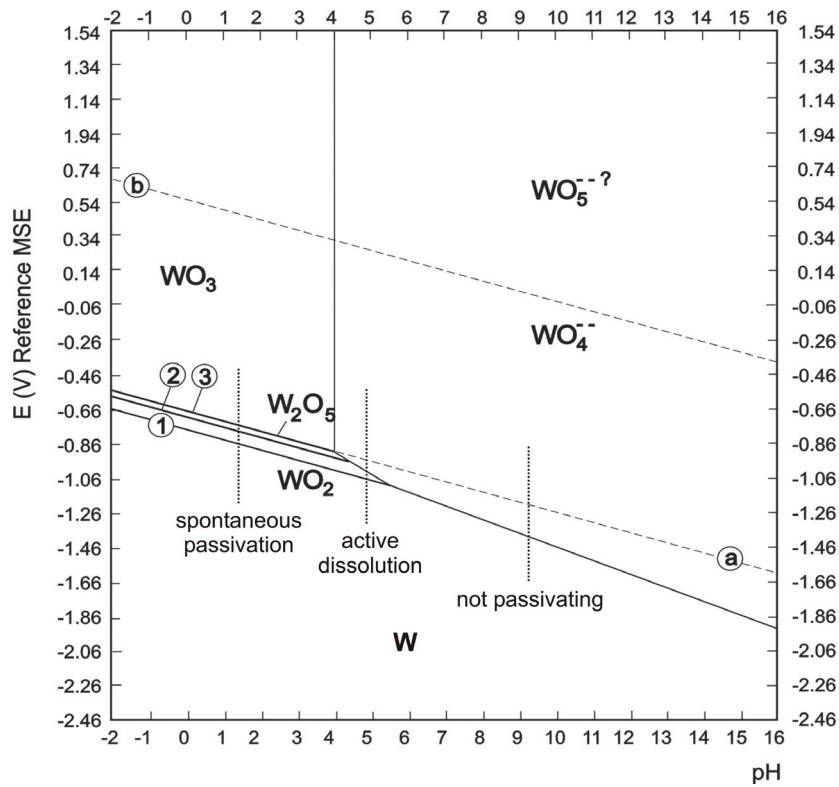
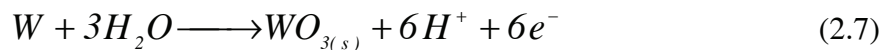


Figure 2.5 Pourbaix diagram for tungsten ($25^{\circ}C$, $[WO_4^{2-}] 10^{-6} mol/l$) [13]. The line a expresses the reduction equilibrium of water $E_{0a} = -0.0591pH [V]$ at a hydrogen or oxygen pressure of 1 atm [13]. The line b expresses the oxidation equilibrium of water $E_{0b} = 1.228 - 0.0591pH [V]$.

In strongly acidic solutions the tungsten film growth can be presented by the following reaction [13]:



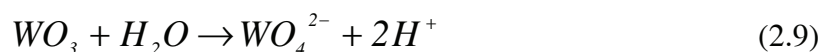
Thermodynamically, tungsten trioxide WO_3 (yellow color) is reported to be stable in acidic environments. In acidic solution the passive film formed by anodisation of tungsten (which is usually WO_3) is not easily soluble. [13] In strongly acidic electrolytes tungstate cations may be formed.

Many authors studied the tungsten oxide dissolution in acidic solutions but, thus far, no general agreement on the mechanism has arisen. Di Paola et al. [16] proposed the dissolution model of tungsten in acidic solutions through the formation of intermediate species (as WO_2^{2+}). The WO_2^{2+} are not stable and do not appear in the Pourbaix diagram of tungsten (Figure 2.5).



The same author pointed out that for $pH > 1$ the passive dissolution of tungsten could be obtained as conversion of species more stable than WO_2^{2+} [16], such as WO_4^{2-} .

Anik et al. [18][19][20] investigated influence of pH on the anodic behavior of tungsten. They suggested that between pH 1 and 2.6 (which corresponds to the point of zero charge of the tungsten oxide surface) both H^+ and H_2O assist the WO_3 dissolution. When approaching the pH 2.6 the contribution of H^+ assisted dissolution diminishes and the passive dissolution of tungsten follows the reaction:



Metallic tungsten is believed to dissolve as WO_4^{2-} . This reaction likely proceeds through the formation of oxide. We have accepted the model of the tungsten passivation in acidic solutions from the literature [21], given in Figure 2.6. The model depicts the anodic reactions in the presence of a passive film (passive dissolution). These reactions govern the growth of the passive film. The passive dissolution rate depends on the properties of the passive film (ion transport).

Gradient of the WO_4^{2-} ions concentration in the Nernst diffusion layer of a thickness δ determines the dissolution rate (Figure 2.6). The concentration of WO_4^{2-} in the bulk solution is expected not to be stationary with increasing time. Thermodynamical data

imply equilibrium for the reaction (2.9). However, in the CMP the equilibrium does not occur, except in the case of adding the WO_4^{2-} to the solution.

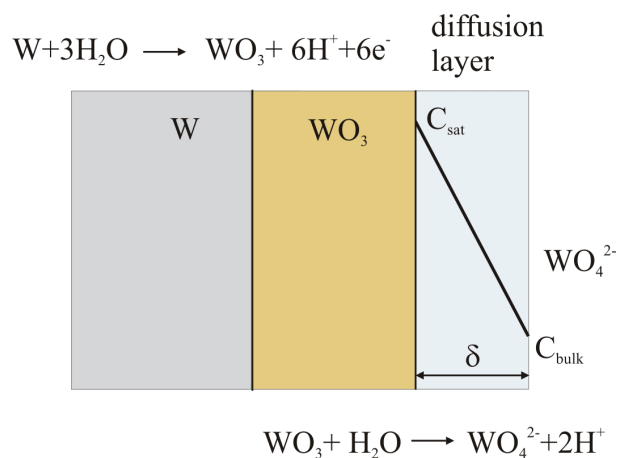


Figure 2.6 Tungsten oxidation model in acidic solutions. Gradient of the WO_4^{2-} ions concentration in the Nernst diffusion layer determines the dissolution rate.

Only few studies on characterization of the electrochemically formed passive oxide films on tungsten surface are published. The growth of passive oxide could proceed through the mechanisms presented in Figure 2.7. At the beginning the current flow is governed by Ohm's law in the electrolyte (explained in Appendix A) rather than by electrode polarization [12], possibly followed by high field conduction and mass transport mechanism.

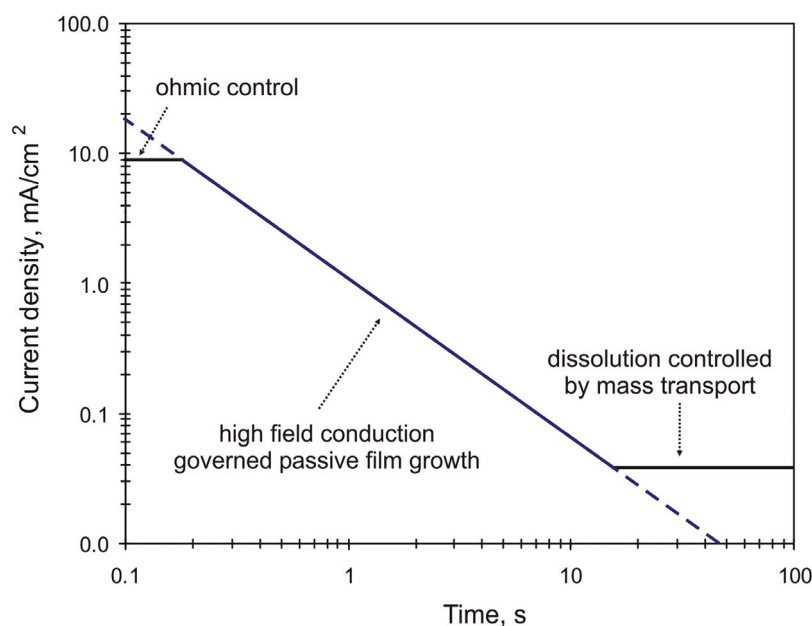


Figure 2.7 Mechanisms of the oxide growth on tungsten.

Ohmic controlled current density at the beginning of polarization is attributed to the change of potential in the potentiostatic polarization technique (see Chapter 3.1.1). The ohmic drop in the solution prevents the potential to instantly reach the prefixed value. Therefore, the current exhibits a plateau in the log-log scale, instead of having a higher value followed by the linear decrease, as shown in Figure 2.7. This phenomenon is less pronounced at lower current densities and in the solutions of sufficient conductivity to keep the ohmic effects small.

High field conduction model (HFM, variable field) [12][22] describes the oxide growth through the thickening of the oxide films due to migration of ions in the solid (WO_3) under the effect of a strong electric field (Figure 2.8), according to the equation [22]:

$$i = i'_0 \exp\left(B' \frac{\Delta\Phi_2}{L}\right) \quad (2.10)$$

where i'_0 is a constant proportional to the mobility of ions in the absence of the electric field, B' is the constant proportional to the charge number and lattice constant, $\Delta\Phi_2$ is the potential difference through the film and L is the film thickness. When the potential is

changed and electric field increases, the film growth is limited by ion conduction through the oxide film.

According to HFM the potential differences at the metal-film and film-electrolyte interfaces do not change significantly during growth. Current density, i , at the interface film-electrolyte can be presented with the reaction:

$$i = i_{gr} + i_{diss} \quad (2.11)$$

where i_{gr} is the current density leading to film growth and i_{diss} is the current density corresponding to metal-ion dissolution. [12] In the case when $i_{gr} = i_{diss}$ the film growth is limited. The study of Vergé et al. [25] showed that the oxide growth of tungsten in acidic solutions was controlled by high field conduction (HFM). Other oxide growth models are also suggested in the literature [23][24]. When an anodic potential is imposed to already passive metal electrode, HFM predicts a decreasing growth rate (i) with time [24]. In practice, that can be explained using the Equation (2.10). The thickness L increases with time leading to decrease of the growth rate (i) over time. As shown in the literature [12] a linear relationship between the current density and the passivation time, in double log scale, is predicted during potentiostatic polarization:

$$\ln i = A_1' - A_2' \ln t \quad (2.12)$$

where A_1' and A_2' are the constants depending on the imposed potential. The current will stop decreasing if the dissolution of the oxide takes place.

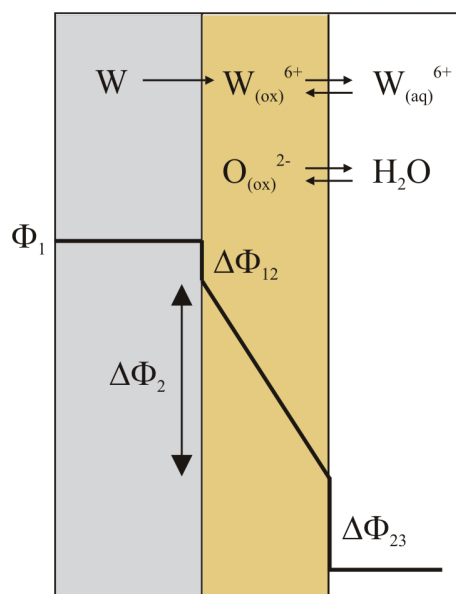


Figure 2.8 Reactions on the metal-film and film-electrolyte interfaces leading to the growth and dissolution of the passive oxide films and variation of potential across the passive film.

Mass transport is the transport of reactants and products to and from the electrode. The rate of reactants and products transport is influenced by the difference in concentration of the reactants and products in the bulk electrolyte and at the electrode surface. Nernst's diffusion layer simplifies the modelling of the mass transport phenomena by taking into account the concentration of the products. [12] The Nernst model separates clearly two transport mechanisms, diffusion and convection. It assumes the total absence of convection inside the Nernst diffusion layer ($y < \delta$) and an absence of diffusion outside the Nernst diffusion layer ($y > \delta$). The maximum rate of partial anodic reactions, named limiting current density, i_l , is mass transport controlled and can be expressed with the following equation [12]:

$$i_l = \pm nFD_B \frac{c_{B,sat} - c_{B,b}}{\delta} \quad (2.13)$$

where D_B is the coefficient of diffusion, $c_{B,sat}$ is the saturation concentration of the product B at the electrode surface, $c_{B,b}$ is the concentration of the product B in the bulk solution and δ is the thickness of the Nernst diffusion layer. The thickness of the Nernst diffusion layer depends on the hydrodynamic aspects. Therefore, a mass transport

phenomenon in the electrochemistry and corrosion is studied using the rotating-disk electrodes, RDE (see Figure 3.1). Mass transport is observed to be uniform over the whole rotating disk electrode surface. Thickness of the diffusion layer and current density are dependent on convection phenomena. With a rotating electrode mass transport conditions are considered as forced convection conditions. Levich equation represents an analytical solution for the mass transport to a rotating-disk electrode (the flux to the electrode under laminar flow conditions) [12]:

$$|i_l| = 0.62nFc_{B,b}D_B^{2/3}\nu^{-1/6}\omega^{1/2} \quad (2.14)$$

where ω is the angular velocity and ν is the kinematic viscosity.

Vergé et al. [25][26] showed that the film formation on tungsten is accompanied by a mass transport controlled dissolution reaction. Their investigation on anodic oxide growth on tungsten showed double sized thickness of the oxide film on a stationary electrode comparing to the oxide thickness formed at the electrode rotating at 600 rpm. The difference is due to the higher dissolution rate at the rotating electrode. On the stationary disk electrode the film continues to grow over longer period while with rotation a steady state film thickness (potential dependent) is reached after shorter period. The thickness of the passive WO_3 film was reported to increase at the growth rate of approximately 2 nm/V when increasing the imposed electrode potential, starting from the potential value of 1.5 V MSE [25]. Lower potentials were not investigated.

Osseo-Asare et al. [27] investigated the effect of tungstate ion, WO_4^{2-} , on the electrochemical behavior of tungsten. At pH 2.8 Anik [28] showed that the anodic current decreases in the presence of added tungstate ions. This decrease in current can be attributed to the increased concentration of metal ions in the bulk solution, $c_{B,b}$, according to Equation 2.13.

2.3. Tribology

Tribology is the science and technology of interacting surfaces in relative motion and embraces the study of friction, lubrication and wear [29]. The bodies forming a tribological contact (Figure 2.9) are often exposed to corrosive environment, leading to both mechanical and chemical degradation.

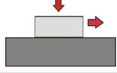
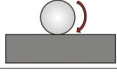
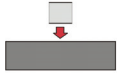
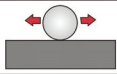

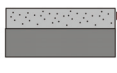
ELEMENTS	WEAR MECHANISM		FATIGUE	ABRASION	ADHESION	TRIBO-CHEMICAL WEAR
	TYPE OF THE RELATIVE MOTION					
SOLIDS		SLIDING	✓	✓	✓	✓
	SLIDING WEAR					
		ROLLING	✓	✓	✓	✓
	ROLLING WEAR					
SOLIDS		IMPACT	✓	✓	✓	✓
	IMPACT WEAR					
SOLIDS		OSCILATION	✓	✓	✓	✓
	FRETTING					
SOLID/FLUID		FLOW	✓	✓		✓
CAVITATIONAL WEAR						
SOLID/FLUID +PARTICLES		FLOW	✓	✓		✓
FLUID EROSION						

Figure 2.9 Different types of tribological contacts and wear mechanisms classification.

[30]

In our study the evaluation of tungsten wear mechanisms is of great importance. Wear can be defined as damage to a solid surface that generally involves progressive loss of material and is due to relative motion between that surface and a contacting substance or substances. [31] Four principal wear mechanisms (Figure 2.9) are: fatigue, abrasion, adhesion and tribo-chemical (oxidative) wear. Four of them occur in all relative motion types except solid/fluid and solid/fluid plus particles elements combinations in flow motion. Even though new models are being developed in order to explain wear phenomena, classical theories developed decades ago are being continuously used. Material loss from the solid surface can only occur in three ways: by melting, by chemical dissolution or by physical separation of atoms from the surface. Mechanical and chemical processes may take place separately or together (such as abrasion in a corrosive environment).

Wear due to surface fatigue can be characterized by crack formation and flaking of material caused by repeated alternating loading of solid surfaces. [32]

Abrasive wear is due to hard particles or hard protuberances that are forced against and move along a solid surface. Depending on the type of contact two-body or three-body abrasion can take place. [31]

Adhesive wear refers to transference of material from one surface to another during relative motion due to a process of solid state welding.

One of the most widely used equations to describe the wear process is the Archard's equation:

$$V_w = k_w \frac{F_n v_s}{H_s} \quad (2.15)$$

where V_w is the wear rate, k_w is the wear coefficient depending on specific wear mechanism, F_n is the normal load, v_s is the sliding velocity, and H_s is the hardness of the softer of the two materials in contact.

Tribo-chemical wear can be characterized by rubbing contact between two solid surfaces reacting with the environment and leading to a removal of the metal and chemical reaction products from the surfaces in contact.

Oxidative wear is the most common tribo-chemical wear process. It is usually, but not always, a beneficial form of corrosion in which oxide films form on the metal surface. [33] The wear process proceeds by continual removal and reformation of thin oxide films, as presented in Figure 2.10. The film breaks when it reaches the critical thickness, L_{crit} .

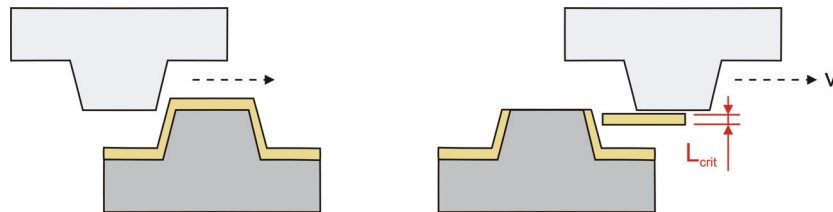


Figure 2.10 Oxidative wear mechanism. [12]

The model proposed by Quinn [31] suggests that the oxide is removed whenever it reaches a critical thickness after having grown according to the parabolic law. The wear volume can be expressed by equation [12]:

$$V_{ox} = \frac{k_L}{v_s L_{crit}} \frac{F l_{sl}}{H_s} \quad (2.16)$$

where k_L is the oxidation rate constant, v_s is the sliding velocity, L_{crit} is the critical thickness of the oxide layer, l_{sl} is the sliding distance. The shortcoming of this model is that it takes into account only the passivation phenomena and neglects the possible dissolution.

2.4. Tribocorrosion

Tribocorrosion can be defined as the material deterioration process which results from the interaction of wear and corrosion that takes place in tribological contact exposed to aggressive environment. [34]

The examples of tribocorrosion in sliding contacts exposed to aqueous solutions can be found in the mining equipment, food processing devices, biomedical implants, chemical-mechanical polishing (CMP), etc.

The passivation behavior of metals is particularly important for tribocorrosion [35]. Passive metals are particularly susceptible to tribocorrosion because rubbing can destroy the protective properties of the passive film and lead to a high corrosion rate before the surface repassivates. It is well known in tribology that a corrosive environment can accelerate the wear rate. [1] Tribocorrosion behavior can not be predicted by using separately the knowledge of tribological behavior in the absence of corrosive medium or that of the electrochemical behavior in the absence of wear because friction and wear modify the sensitivity of the material to corrosion and inversely corrosion modifies the friction conditions. For a mechanistic interpretation of the tribocorrosion phenomena one must be able to distinguish the metal loss due to chemical or electrochemical oxidation from the metal loss due to mechanical wear (Figure 2.11). The total volume of removed material (wear track volume), V_{wt} , is equal to the sum of oxidized metal during rubbing (wear accelerated corrosion), V_{ch} , and mechanical wear volume (material removed mechanically), V_m :

$$V_{wt} = V_{ch} + V_m \quad (2.17)$$

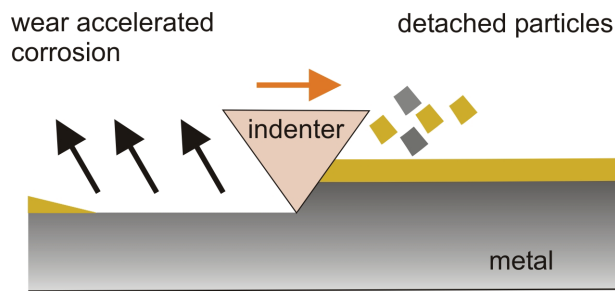


Figure 2.11 Material loss in tribocorrosion system.

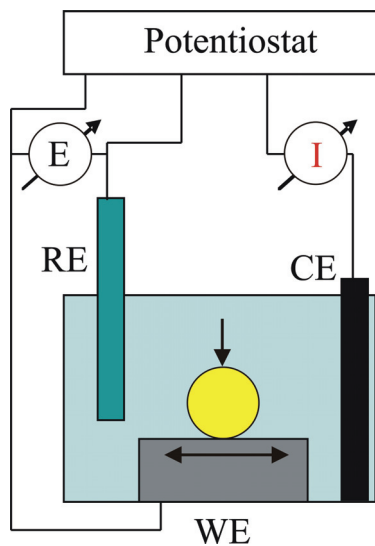


Figure 2.12 Schema of potentiostatic set-up for tribocorrosion experiments. [5]

The coupling of mechanical and electrochemical methods offers the possibility to carry out friction tests under well defined corrosion conditions. Suitable electrode potentials simulating oxidising powers of the solution are imposed by potentiostat. In the potentiostatic set up for tribocorrosion measurements (Figure 2.12), current (I) passes between working (WE) and counter electrodes (CE) and potential (E) is measured between working and reference electrode (RE). Mischler [5] has reviewed the different electrochemical-controlled tribocorrosion techniques published in the recent years. Electrochemical techniques are well suited for the study of tribocorrosion mechanisms, because they offer the possibility to directly measure the contribution of oxidation to the overall material loss. [5][36] Electrochemical polarization allows one to impose an anodic

or cathodic potential to simulate specific corrosion conditions in a tribological contact, in order to study the effect of potential on the wear behavior.

One of the first studies in this area, the investigation of corrosion influence on the wear behavior of passivating metals in aqueous solutions, was undertaken by Mischler et al. [37]. Over the past years an increasing interest has arisen on the possibility to investigate the combined corrosion–wear degradation of materials by electrochemical polarization in conjunction with wear testing under sliding conditions. [38]

It has been observed that in tribocorrosion the material removal usually exceeds the sum of mechanical and corrosion contributions measured separately. [2] The increased interest on combined electrochemical and friction tests also led to few round robins undertaken. [39] They showed the satisfying reproducibility of the results performed in different laboratories.

In a tribo-electrochemical experiment the amount of anodically oxidized metal is calculated from the measured current using Faraday's law:

$$V_{ch} = \frac{QM}{nF\rho} \quad (2.18)$$

where V_{ch} is the volume of metal transformed by anodic oxidation, $Q = \int I_r dt$ is the electric charge passed that is obtained by integrating the current enhancement due to rubbing, I_r , over the time of the experiment (Figure 2.13), M is the atomic mass of the metal, n is the charge number for the oxidation reaction (apparent valence), F is the Faraday constant and ρ is the density of the metal.

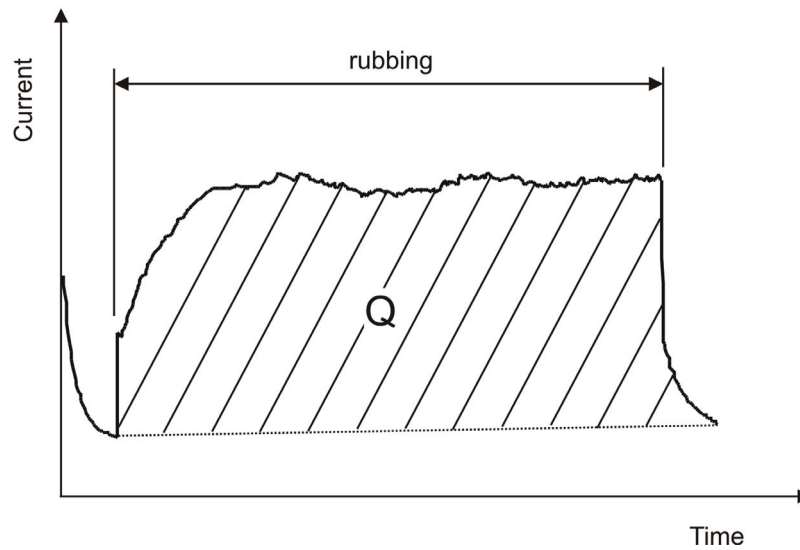


Figure 2.13 Determination of the electric charge in the tribocorrosion test.

The total wear volume, V_{wt} , can be evaluated by measuring the volume of the wear track after an experiment or by measuring the rate of descent of the pin during rubbing. The latter method provides the instantaneous rate of wear, but is applicable only if no significant amounts of solid reaction products, such as third body particles accumulate in the contact during the experiment. From the total wear volume, V_{wt} , and the chemical wear volume, V_{ch} , calculated from the electric charge, the mechanical wear volume, V_m , which is the volume of metal removed mechanically, is obtained by subtraction [1]:

$$V_m = V_{wt} - V_{ch} \quad (2.19)$$

It may be mentioned that this equation is valid independent of whether anodic oxidation leads to formation of dissolved metal ions or of solid reaction products, such as oxide films.

2.4.1. Modelling Tribocorrosion

Mischler et al. [40] and Landolt et al. [1] proposed a model for the prediction of the rate of wear accelerated corrosion in a two body sliding contact (passive metal and inert indenter) taking into account both the effect of normal load and the repassivation behavior of the metal.

Mechanical wear leads to thinning or local removal of the passive film, which subsequently repairs itself by oxidation of the metal. As a consequence, rubbing leads to a substantial increase of the anodic partial current. Assuming that the anodic partial current is equal to the measured repassivation current I_p one can write:

$$I_p = R_{dep} Q_p \quad (2.20)$$

In this equation R_{dep} is the rate of generation of depassivated area due to rubbing (m^2/s) and Q_p is the passivation charge density (C/m^2), which represents the charge per surface area leading to reformation of the original passive film on the abraded surface. The value of Q_p can be evaluated by independent electrochemical experiments using the formula

$$Q_p = \int_0^{1/2f} i_p dt, \text{ valid for pin-on-disk devices with reciprocating motion [40], where } f \text{ is the}$$

frequency of rubbing. For a given metal–electrolyte combination the Q_p value depends on imposed potential. According to model [1], repassivation current I_p can be calculated using the equation:

$$I_p = K_{st} v_s (F_n / H_{wt})^b Q_p \quad (2.21)$$

where K_{st} is the proportionality factor including probability of depassivation of a contacting surface element and number of asperities in contact, v_s is the sliding velocity, F_n applied normal load and H_{wt} is the micro hardness in the wear track.

Current increases with the applied normal load according to a square root or a linear relationship, which is expressed with the exponent b . The behavior of real systems is expected to lie somewhere in between the values of $b=0.5$ and 1. It depends on the dominant mechanism and the surface topography. The linear relationship between the repassivation current and applied normal load is predicted in the case of smooth hard body

sliding on a rough ductile body. The exponent b takes the value of 0.5 for the contact between two rough bodies and when a hard rough body is sliding on a smooth ductile body. [1]

The described model does not take into account the possible effect of third body particles. Third body particles formed in the contact area may significantly affect the friction and wear behavior. The exact values of wear-accelerated corrosion current can not be predicted using the Equation (2.21), thus it can allow the prediction of the effect of hardness, frequency, load and stroke length on the wear-accelerated corrosion rate of passive metals [40].

Barril et al. [41] showed the applicability of the models [1][40], developed for the sliding contacts and based on cyclic depassivation-repassivation of the metal surface, in the fretting of Ti_6Al_4V . The effect of the normal load on the anodic current could be described using these models.

The tribocorrosion experiments performed by Stemp et al. [42] using passive stainless steel aimed in evaluating the effects of normal load, sliding velocity, applied potential and counter part alumina ball roughness on wear, friction and anodic current. The depassivation rate due to rubbing was found to be the critical parameter controlling the anodic current. Repassivation kinetics do not play a relevant role as long as the time between two strokes is sufficiently large to allow the complete repassivation of the exposed metal.

Jemmely et al. [36] made the first attempt in mathematical modelling of current transients measured in an electrochemically controlled reciprocating motion tribometer taking into account film formation kinetics and ohmic effects (explained in Appendix A). The important factors such as electrochemical conditions prevailing in the contact zone, the role of the third body particles and selective dissolution of iron were not included in the model. This led to important quantitative discrepancies between simulated and measured transients. However, it was found that repassivation kinetics of the alloy determines the chemical degradation rate in a tribocorrosion system, rather than the corrosion resistance.

Jiang et al. [43] developed wear models for sliding wear in both gaseous and aqueous environments, as well as wear-corrosion maps from the model corresponding to aqueous conditions. Important factor in determining the dominant material loss regime for a given

tribo-system is a ratio between the contact frequency and the corrosion passivation rate. If the values of the mentioned ratio are high, the corrosion induced wear becomes the dominant regime for material loss.

Third Body

Tribocorrosion system involving a passive metal (first body), an inert counter body (second body) and a third body is presented in Figure 2.14 [5].

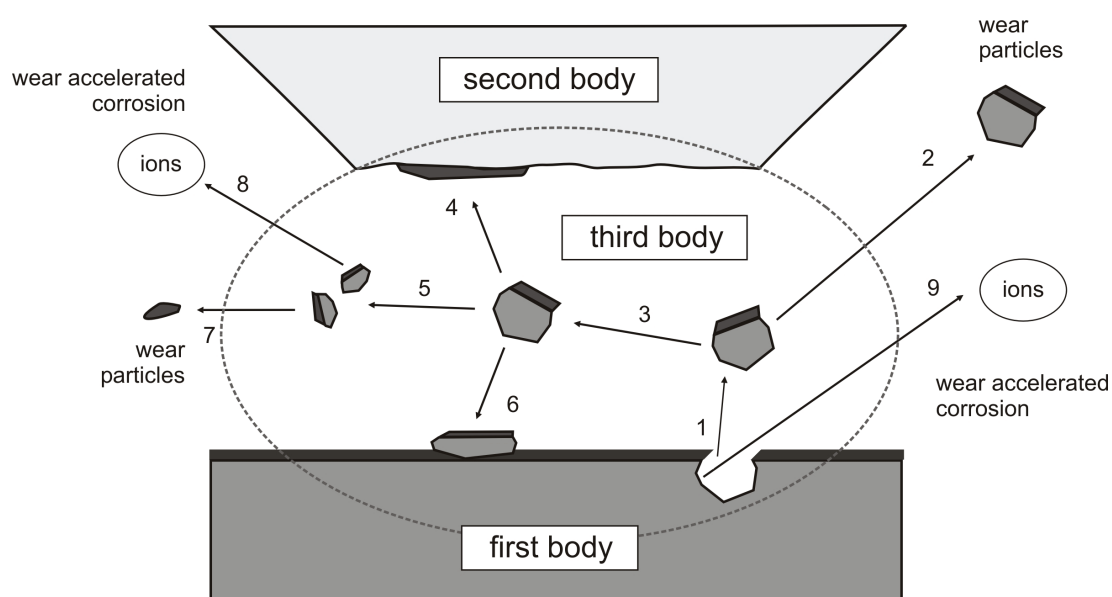


Figure 2.14 Schema of the tribocorrosion contact with the third body approach. [5]

The contact is immersed in electrolyte. In order to explain material flows and reactions in such a tribocorrosion system the approximation that second body does not undergo any wear is made. The material removal during rubbing occurs through the action of both mechanical and electrochemical mechanisms. Initially, due to the action of counter body, the wear particle detaches from the metal surface (Figure 2.14 flow 1) by any of the classical wear mechanisms (given in Figure 2.9). Material can be removed from the contact in two ways. Firstly, through direct ejection of particles and ions (Figure 2.14 flow 2 and 9) detached from the metal surface. Secondly, detached metal particles may undergo the transfer to the third body (flow 3) and later be ejected in the form of particles or ions (Figure 2.14 flow 7 and 8) after transformations in the contact. The transformations of the third body particle include adhesion to the counter body (flow 4), fragmentation to smaller particles (flow 5) or adhesion to the metal (flow 6). Corrosion takes place on the active

metal surface after particle detachment and on third body particles in the process of defragmentation. Depending on the properties of the third body particles, corrosion can accelerate or slow down the rate of mechanical material removal from the first body. [34]

2.4.2. Chemical and Electrochemical Effects in the CMP and Tribocorrosion of Tungsten

The literature survey of the chemical and electrochemical effects in the CMP and tribocorrosion of tungsten is given in Table 2.1.

Table 2.1 Summary of the research in the filed of chemical and electrochemical effects in the CMP and tribocorrosion of tungsten, showing the used solution composition, electrochemical and tribocorrosion techniques.

First author	References	Solution chemistry	Electrochemical techniques	Tribocorrosion techniques
F.B. Kaufman	[4]	mixture of ferricyanide-phosphate in the presence of the free abrasive particles		CMP polishers
M. Ziomek-Moroz	[2]	$K_3Fe(CN)_6$	potentiostatic and potentiodynamic polarization	CMP polisher
C.-W. Liu	[44]	H_2O_2	chemical etching	CMP polisher
R. Singh	[45]	ceria particles and abrasive-free slurry		CMP polisher
P. B. Zantye	[3]	CMP slurries for oxides and metals	potentiostatic and potentiodynamic polarization	CMP polisher
D. Tamboli	[21]	KIO_3 , H_2O_2 , $K_3Fe(CN)_6$	potentiostatic and potentiodynamic polarization	CMP polisher
S. Perry	[46]	KIO_3 , H_2O_2	chemical etching	
E. A. Kneer	[47]	KIO_3 , H_2O_2	potentiodynamic polarization	
Anik	[48]	KIO_3	potentiodynamic polarization	
Y.-J. Seo	[49]-[53]	alumina particles KIO_3 , H_2O_2 , $Fe(NO_3)_3$	potentiodynamic polarization	CMP polisher

C. Raghunath	[54]	alumina slurries containing ferric salts	potentiodynamic polarization, electrochemical quartz crystal microbalance (EQCM)	CMP polisher
H. Liang	[55]	CMP slurries, abrasive Si ₃ N ₄ , citric acid		CMP polishers
M. Biemann	[57]	H ₂ SO ₄ K ₃ Fe(CN) ₆	potentiodynamic polarization and anodic current-time transients measurements	reciprocating sphere-on-plate tribometer
D. J. Stein	[58]	KIO ₃ , Fe(NO ₃) ₃ , (NH ₄) ₂ S ₂ O ₈	dc and ac based electrochemical techniques	polishing apparatus with a modified rotating disk electrode
S. B. Akonko	[17]	K ₃ Fe(CN) ₆	potentiodynamic polarization	pin-on-disk tribometer

Chemical Effects (Oxidizing and Chelating Agents)

According to Kaufmann's mechanism [4] (Figure 2.3) the tungsten removal proceeds through the cyclic formation of the passive film which is subsequently removed by the mechanical action of the particles (as shown in Figure 2.15).

Ziomek-Moroz et al. [2] found out that the presence of passive protective film on tungsten metal surface plays a critical role in successful planarization. Regarding CMP as a one step-polishing process (only one type of metal to be polished in one step) an optimum metal CMP process is the one where the rate of passivation is equivalent to the rate of removal [44]. Sing et al. [45] have stated in their survey of the CMP process that the advantage of the formed passive oxide on tungsten concerning removal is its brittleness. They also pointed out that chemicals in the slurry composition are influencing the dynamics of passive film formation.

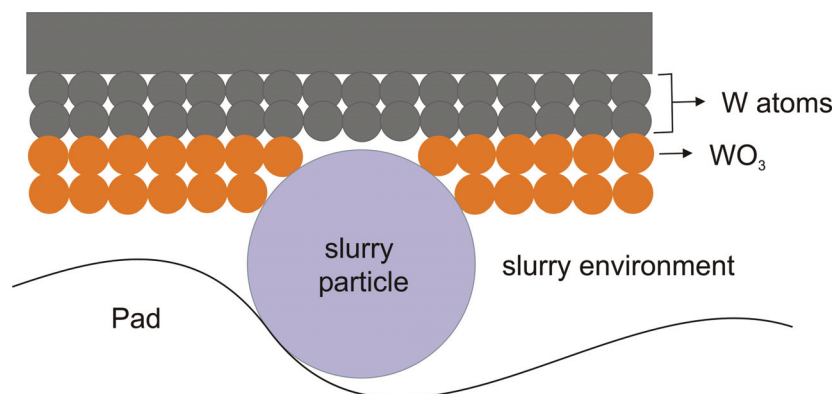


Figure 2.15 Principle of tungsten removal in the CMP process.

Different authors investigated the role of oxidizers in abrasive free and abrasive slurries [3]. Tamboli [21] also showed the existence of significant differences in passive oxide growth processes for tungsten in KIO_3 and H_2O_2 . The passive WO_3 growth rate formation in KIO_3 results in WO_3 film formation with a growth rate increasing with an increase in imposed potential [21]. Also, the increase in absorbed OH^- groups is observed at higher potentials in KIO_3 solution corresponding to higher initial oxide growth rates. During the oxidation of tungsten in the presence of H_2O_2 high current densities are observed in the passive region. This can be attributed to high oxide dissolution at the oxide-solution interface. Passive region existence can be related to current limited by mass transport process during dissolution of oxides.

Perry and al. [46] investigated the influence of four aqueous solutions (KOH , KIO_3+NaOH , $\text{H}_2\text{O}_2+\text{NH}_4\text{OH}$ and $\text{H}_2\text{O}_2+\text{HCl}$) of varying pH and oxidizing power, on dissolution of thin tungsten films. The tungsten oxide film treated with $\text{NH}_4\text{OH}+\text{H}_2\text{O}_2$ solution exhibited the highest removal rate and the greatest change of the surface morphology. These findings highlight the multiple and complex dependence of the oxide film dissolution on the solution composition. Kneer et al. [47] showed that the addition of H_2O_2 at pH 2 or 4 resulted in increased tungsten dissolution.

Anik et al. [48] investigated the reduction behavior of iodate ion, IO_3^- , on tungsten. They suggested that oxide film formation on tungsten was considerably accelerated in the presence of IO_3^- . Also, they found out that increase in IO_3^- concentration is increasing the dissolution rate and polishing rate at pH 4, but it has no effect at pH 2. This is probably due

to the fact that in the case of pH 2 the cathodic and anodic curves intercept under conditions where the anodic current is independent on potential.

Seo et al. [49] confirmed that fast and effective formation of a surface oxide layer is the key factor for achieving a high removal rate and better tungsten CMP performance. They also studied the effects of mixed oxidizers on tungsten chemical-mechanical polishing process, using three different types of oxidizers: $\text{Fe}(\text{NO}_3)_3$, KIO_3 and H_2O_2 . [50] By comparing the CMP performance and electrochemical behavior of the tungsten film as a function of mixed oxidizer they showed that the oxidizer corresponding to the highest removal rate implied high dissolution rate. Apparent difference among removal rates achieved with different oxidizers is due to the modified chemical reaction and surface passivation as a function of each oxidizer. [51] Tungsten metal CMP characteristics are strongly dependent on the amounts of H_2O_2 oxidizer additive. [52][53] When increasing the amount of H_2O_2 from 1 vol % up to 9 vol % the removal rate increases up to the H_2O_2 concentration value of 5 vol %, which represents the critical point between the electrochemical corrosion and passivation state. For the 5 vol % of H_2O_2 corresponding to the highest removal rates both chemical and mechanical actions simultaneously occur due to formation of the passive WO_3 layer. [53]

Seo et al. [52], as well as Akonko and al. [17], stated that the hardness of the passivation layer of WO_3 formed by the oxidizer in the slurry solution is lower than hardness of tungsten metal. Nevertheless, they did not present the exact hardness' values.

Raghunath et al. [54] investigated the combined effect of oxidizing agents and particles from the slurries on the passivation of tungsten surface during CMP process. The addition of Fe^{3+} salt to a dispersion of high purity alumina particles can passivate tungsten forming FeWO_4 . The beneficial effect of the Fe^{3+} is to reduce the deposition of alumina particles onto tungsten and FeWO_4 surfaces and reduce contamination.

As shown in this subchapter, the oxidizing agents are influencing the tungsten removal in a high extent. Their interactions are complex, depending on the concentration, pH and also on the type of the abrasives present in the slurries.

The studies on the influence of chelating agents (particularly lactic and phosphoric acid) are lacking. Liang et al. [55] showed that addition of chelating agent citric acid [56] increases the amount of tungsten chemical removal by 133 %.

Electrochemical Effects (Electrode Potential)

Bielmann et al. [57] conducted electrochemical and wear experiments in order to shed some additional light on the tribo-chemical phenomena occurring during tungsten CMP. They performed measurements of the wear track volumes with the same value of potential, once obtained chemically, during rubbing in the $K_3Fe(CN)_6$ at OCP (free potential) and after with electrochemically imposed equivalent potential during rubbing in H_2SO_4 . The wear was identical for both experiments and this result suggested that electrochemical polarization can be used to simulate the oxidizing action of a corrosive environment by imposing a controlled potential. Potentiodynamic measurements indicated passive film formation, especially when applying an anodic potential. The current measurements taken during tribocorrosion experiments, coupled with the wear track depths measurements, confirmed the earlier observation regarding the passivation of the tungsten surface and also indicated that this passivation is necessary in order for any significant abrasion to take place. These results seem to support the Kaufman's mechanism for tungsten CMP.

Nevertheless, Stein et al [58] used electrochemical techniques to investigate the effect of electrode potential in CMP processing of tungsten. Those authors found no difference in removal rate when tungsten was kept at anodic or at cathodic potential.

Akonko et al. [17] concluded that application of an anodic potential appears to be a promising approach to make CMP of tungsten more effective with higher removal rates and smaller roughness. They found an increase in wear when increasing potential from OCP to 1.2 V MSE. Also, Akonko stated that wear of tungsten in the $K_3[Fe(CN)_6]$ solution increased with slurry's pH value (in the range from pH 4 to pH 6).

As presented above, the number of studies on the influence of the electrochemically imposed potentials on the tungsten removal rate is limited. Therefore, and also due to discrepancies in the results and conclusion, the influence of electrode potential is still not clear.

2.5. Rationale of the Thesis

Most of the studies performed in order to investigate the role of electrochemical and/or mechanical action in the CMP of tungsten indicated that tungsten removal rate was controlled by tribocorrosion.

Kaufmann's mechanism suggested that global planarization of tungsten can be achieved in slurries that help the formation of WO_3 passive oxide film. The planarization of tungsten is a tribocorrosion process of successive abrasion of the oxide film, which continuously forms on the surface activated mechanically by particle abrasion and exposed to the slurry. The process of repetitive passivation-abrasion-repassivation leads to global planarization of the metal surface. The removal of tungsten is affected by the thickness and formation kinetics of the passive film, which depends on oxidizing properties and chemical composition of the solution. Literature survey [57] showed that wear of tungsten under an electrochemically imposed potential is equivalent to wear under the same potential but established by adjusting the oxidizing power of the solution. High electrode potential usually leads to thicker passive films and thus, according to Kaufman's mechanisms, to higher removal rates. It was found [17] that wear of tungsten was significantly increased when applying an anodic potential. On the contrary, some authors [58] showed no difference in the wear of tungsten when cathodic or anodic potential was imposed.

Concerning all the facts given in the previous paragraph, the necessity to further and systematically investigate the effect of the imposed potential corresponding to oxidizing power of the solution (electrode potential) and of the solution chemistry (especially chelating agents) on the tribocorrosion of tungsten, have been recognized and set as an objective of this PhD thesis. Especially, the investigation of electrochemical and tribocorrosion behavior of tungsten in the larger range of electrode potentials is needed in order to explain the observed discrepancies on the effect of potential. We know that the thickness of the oxide film is affected by the mass transport, electrode potential and by the presence of chelating agents. According to the accepted tungsten corrosion model (Figure 2.6) we expect to have lower values of oxide thickness on the tungsten surface in the presence of chelating agents. Chemical effect in the CMP of tungsten is not well understood and the systematic investigation is needed.

This study should also help understand how far electrochemical parameters play a role in the CMP. This could help simplifying the complex slurry composition and optimizing the slurry performances (to improve the removal rate, selectivity of the slurries and the quality of the surface finish), which is imposed as well by ecological aspects.

In order to investigate the influence of potential and solution chemistry of tungsten, the sliding wear test rigs coupled with an electrochemical control (tribocorrosimeter) will be used. The advantage of the tribocorrosion technique is the possibility to control the electrochemical parameters easily without the use of complex chemistry, by imposing the electrode potential (corresponding to the oxidizing power of the solution) by potentiostat. The alumina ball as a counter body was chosen due to its chemical inertness and hardness. The difference between the CMP and tribocorrosion technique lies in the fact that in the first one the three body contact (wafer, pad, abrasives) is present, and in the later one the two body sliding contact (alumina ball, tungsten disk) takes place. Despite the differences among the CMP practice and the tribometer tests, the conditions in both systems are not far. Other techniques, such as micro abrasion tests [59], are in principle more convenient for this study, since they are closer to the mechanical conditions found in CMP. However, a short coming of their use in this type of study is the limitation of controllability of the electrode potential.

Because of the limitations of the tribocorrosion approach, we have also carried out the tests on the real CMP machine in attempt to correlate the results from both techniques and to model them.

CHAPTER 3

3. Electrochemical Behavior of Tungsten in H₂SO₄ Solutions

In order to investigate the influence of the electrode potential, mass transport and solution chemistry (lactic and phosphoric acids) on the electrochemical behavior of tungsten, different electrochemical techniques are used.

Potentiodynamic polarization enables the determination of tungsten passivation behavior with the change of electrode potential. Potentiostatic and quasi potentiostatic techniques can improve the understanding of the passivation behavior with polarization time. Potential step techniques combined with rotating disk electrodes (RDE) allow the measurement of the passivation kinetics, under mass transport control.

Surface analysis techniques (XPS, AES) are used to assess surface chemistry.

3.1. Experimental Techniques

3.1.1. Electrochemical Experiments

Tungsten samples with diameter of 5.3 mm, supplied by GoodFellow, were embedded in an epoxy resin, as presented in Figure 3.1. The purity of the samples was 99.95 %. These samples were used as a working electrode (WE) for all electrochemical experiments except were otherwise stated. These samples are convenient for use in both modes, as a stationary (SDE) and as a rotating disk electrode (RDE) (Figure 3.1), which allow the variation of mass transport conditions.

For the electrochemical experiments, the tungsten electrodes were mirror polished on the manual polishing machine Struers with the carbon grit paper (grain size 500, 1000, 2400, 4000). In the last polishing stage Struers DP Mol was used with the diamond spray of 1 μm and lubricant Red. Afterwards, samples were rinsed with alcohol and distilled water and dried with argon.

Reference electrode (RE) for all experiments in this PhD research project was mercury sulphate electrode (MSE) which potential vs. the standard hydrogen electrode (SHE) is 0.658 V at 25°C. All the potentials in this thesis are given with respect to this standard mercury sulphate electrode and all the tests were performed at room temperature. Two graphite electrodes were used as counter electrodes (CE) in electrochemical experiments. Schema of the electrochemical cell is given in Figure 3.1.

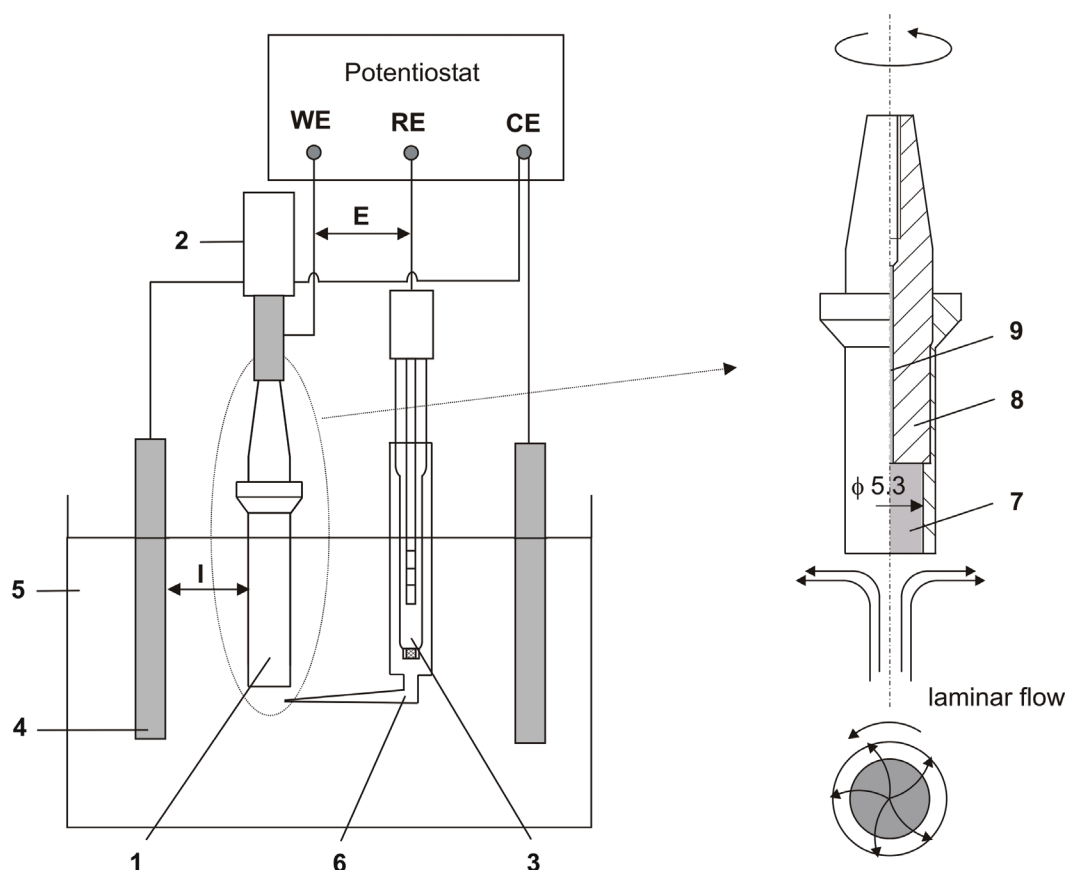


Figure 3.1 Electrochemical cell consisted of a rotating disk electrode (RDE) (1), connected to a motor (2), mercury sulphate reference electrode (3), two graphite counter electrodes (4), immersed in a solution (5) and a Luggin capillary (6). RDE is composed of tungsten cylinder (7) embedded in epoxy resin (8). Metal rod (9) serves for electrical contact.

Different electrochemical experiments and solutions used in this study are presented in Table 3.1. All the solutions had a pH value of 1.5 ± 0.2 . Solution quantity for each experiment was 75 ml. The conductivity κ of the used solutions, measured using the CM 210 Conductivity Meter, is given in Table 3.2.

Table 3.1

Composition of the solutions and type of the experiment carried out.

Solution 0.01 M H ₂ SO ₄ +...	Potentiodynamic polarization	Potentiostatic polarization (SDE)	Potentiostatic polarization (RDE)	Current transients	Surface analysis
	x	x	x	x	x
0.1 M C ₃ H ₆ O ₃	x	x	x	x	x
0.25 M C ₃ H ₆ O ₃	x	x			
0.1 M H ₃ PO ₄	x	x	x	x	x
0.25 M H ₃ PO ₄	x	x			

Table 3.2

Conductivity of the solutions, κ .

Solution 0.01 M H ₂ SO ₄ +...	κ , mS/cm
	6.2
0.1 M C ₃ H ₆ O ₃	6.5
0.25 M C ₃ H ₆ O ₃	7.2
0.1 M H ₃ PO ₄	12.8
0.25 M H ₃ PO ₄	19.2

Potentiodynamic Polarization

Potentiodynamic polarization is obtained by imposed linear potential scan. Potentiodynamic anodic polarization was performed using Autolab potentiostat PGSTAT

30, Cyclic voltametry method (Normal staircase). The potentiodynamic scan began at a cathodic potential of -1 V and was increased to an anodic potential of 2 V at a scan rate of 2 mV/s. The scan rate represents a rate at which the potential is changed while the potentiodynamic scan is being performed. Current density, i , was calculated as a ratio between the measured anodic current, I , and tungsten electrode's surface (0.221 cm^2).

Potentiostatic Polarization

Potentiostatic polarization refers to a measurement of a current as a response to an imposed constant potential. The time to reach steady state depends on the specific conditions of the experiment.

Quasi potentiostatic polarization of tungsten was performed using an Autolab PG STAT 30 potentiostat (Chronomethod, Amperometry). The quasi potentiostatic scan began at the cathodic potential of -1 V. After 120 seconds permanence at the given potential, the potential was stepwise increased by 200 mV. This procedure was repeated up to a potential of 0.8 V. The measurements were carried out on a rotating disk electrode apparatus at 0 rpm, 900 rpm and 1600 rpm.

Current Transients

Short passivation period (1 s of passivation) potential step experiments were performed with rotating disk electrodes at 0 rpm and 1200 rpm. The used measurement equipment consisted of Wenking LB 95L Auto Range Laboratory Potentiostat and Lab View software for passivation kinetics measurements, which enabled high acquisition rates. Potential was kept at the cathodic potential of -1 V for 3 ms and then switched to the selected potentials (-0.5 V, -0.2 V, -0.1 V, 0.2 V, 0.5 V, 1 V or 1.5 V) in separated experiments. Due to the configuration of the scan generator used to switch the potential, the potential rise time was approximately 2 ms. Instantaneous current and potential values were measured continuously at a sampling interval of 0.0001 s. Each experiment was performed three times.

Also, long passivation period (120 s of passivation) potential step experiments were performed with rotating disk electrodes at 0 rpm and 900 rpm and the passivation period of 120 s. The used measurement equipment was Autolab PG STAT 30 potentiostat (Chronomethod, Amperometry). The potentiostatic scan began at the cathodic potential of

-1 V for 5 s and potential was then switched to the selected potentials (0.2 V or 1 V) for 120 s in separated experiments. Each experiment was performed twice.

3.1.2. Surface Characterisation

Samples for Surface Analysis

In order to determine the quantitative and qualitative chemical composition of the sample surface, tungsten samples with diameter of 10 mm and thickness of 3 mm were used. Samples of the 99.95 % purity were supplied by GoodFellow. Surface preparation was the same as in the previous electrochemical experiments. The samples were fixed in the sample holder, as presented in Figure 3.2. At the beginning, the surfaces of the samples were exposed to cathodic cleaning at imposed potential of -1.7 V during 300 s, followed by the stabilisation at open circuit potential during 300 s and polarization at chosen potential during 3600 s. After polarization the samples were rinsed with distilled water and dried with compressed air. For each potential two samples were prepared and analysed. The composition of the surface oxide layer for these experiments was determined by XPS and the oxide thickness was measured by depth profile AES.

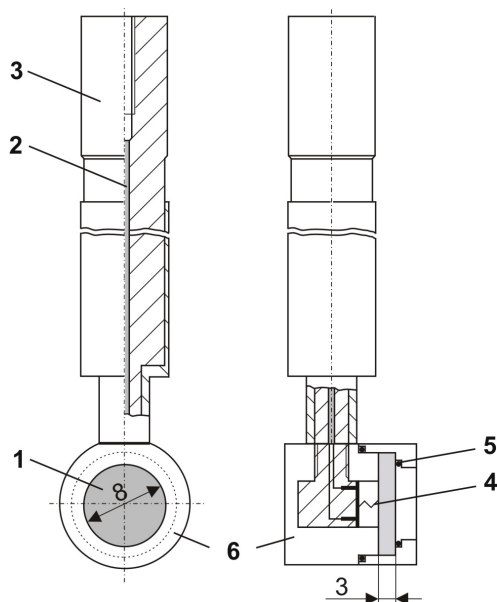


Figure 3.2 Schematic illustration of the electrode body and the holder for the stationary electrode: (1) tungsten sample, (2) electrical contact, (3) PVC rod, (4) spring electrical contact, (5) O-ring and (6) PVC electrode support.

X-ray Photoelectron Spectroscopy (XPS)

The oxidation state of tungsten was determined by X-ray Photoelectron Spectroscopy (XPS). XPS enables detection of metal in various chemical states and is valuable in the analysis of passive oxide films under the action of various oxidizers. The used device was Kratos AXIS Ultra system with monochromatized Al K α X-ray source. The analysed area had the dimensions 700x350 μm and the analysis angle was 90° with the respect to the surface. Curve fitting was performed in the CasaXPS software v. 2.3.12.

The film thickness L_{XPS} can be determined by using the peak area ratio R between metallic and oxidized W signal in the W_{4f} spectrum according to equation [60]:

$$L_{XPS} = -\lambda_{ox} \cos \Theta \ln \left(\frac{R}{R + R^*} \right) \quad (3.1)$$

where λ_{ox} is the electron mean free path in the tungsten oxide, Θ is the escape angle with respect to the surface normal (0° in the present case) and $R^* = \lambda_{met} \sigma_{met} C_{met} / \lambda_{ox} \sigma_{ox} C_{ox}$ where λ is the electron mean free path, σ the photo-electron cross section, C the atomic concentration and the subscript *met* and *ox* representing the metallic tungsten and WO₃ oxide, respectively. The electron mean free path are $\lambda_{met} = 2.0$ nm and $\lambda_{ox} = 2.3$ nm as calculated using TPP-2 formula [61]. The cross section ratio between oxide and metal was assumed to be 1 and the atomic concentration was calculated by dividing the density by the molecular weight of the concerned species.

Auger Electron Spectroscopy (AES)

Sputtering of the surface by an ion beam together with AES analysis allows the acquisition of depth profiles. After XPS analyses Auger depth profiling was performed with a Perkin Elmer PHI 660 Scanning Auger Microprobe using a 2 keV argon ions. Primary electron beam potential and current were 5 kV and 10 nA respectively. The electron beam diameter was approximately 1 μm . Sputtering was performed in a raster mode with sputtered surface of 2 mm x 2 mm. The sputtering rate was 1.2 nm/min as calibrated with 100 nm Ta₂O₅ / Ta NPL standard. Thus, sputter time was converted in sputter depth by considering that the sputter rate of tungsten oxide is 1.5 times higher that the one of Ta₂O₅ [25].

The WO₃ thickness L_{AES} was determined by taking the depth at half height of oxygen atomic content in the film, using the equation:

$$L_{AES} = 1.5 \cdot t_{WO_3}^{AES} \cdot \nu_{Ta_2O_5} \quad (3.2)$$

where $t_{WO_3}^{AES}$ is the sputtering time estimated at the half height of oxygen atomic content, and $\nu_{Ta_2O_5}$ is the sputtering rate of Ta₂O₅, measured on a standard sample with oxide thickness of 100 nm.

3.2. Results

3.2.1. Passivation Behavior of Tungsten in Different Solutions. Potentiodynamic Polarization

The recorded potentiodynamic curves are shown in Figure 3.3. For the curve measured in the 0.01 M H₂SO₄ solution (Figure 3.3 a), during the forward measurement, a current peak is placed in between -0.5 V and 0.5 V. Passive region is situated beyond the potential of 0.5 V and current stabilizes at approximately 0.01 mA/cm². During the reverse measurement, the current density decreases compared to the values in the passive plateau of the forward measurement and the peak does not form.

Polarization curves of tungsten, measured in the presence of 0.1 M C₃H₆O₃ (Figure 3.3 b) and 0.25 M C₃H₆O₃ (Figure 3.10 c), show higher current density values compared to the 0.01 M H₂SO₄ solution, shown in Figure 3.3 a. Current densities in the passive region in the presence of both concentrations of H₃PO₄ (0.1 M and 0.25 M) are higher than ones measured in the 0.01 M H₂SO₄ solution, but lower than ones measured in the presence of lactic acid. In the presence of phosphoric acid the curves are less reproducible.

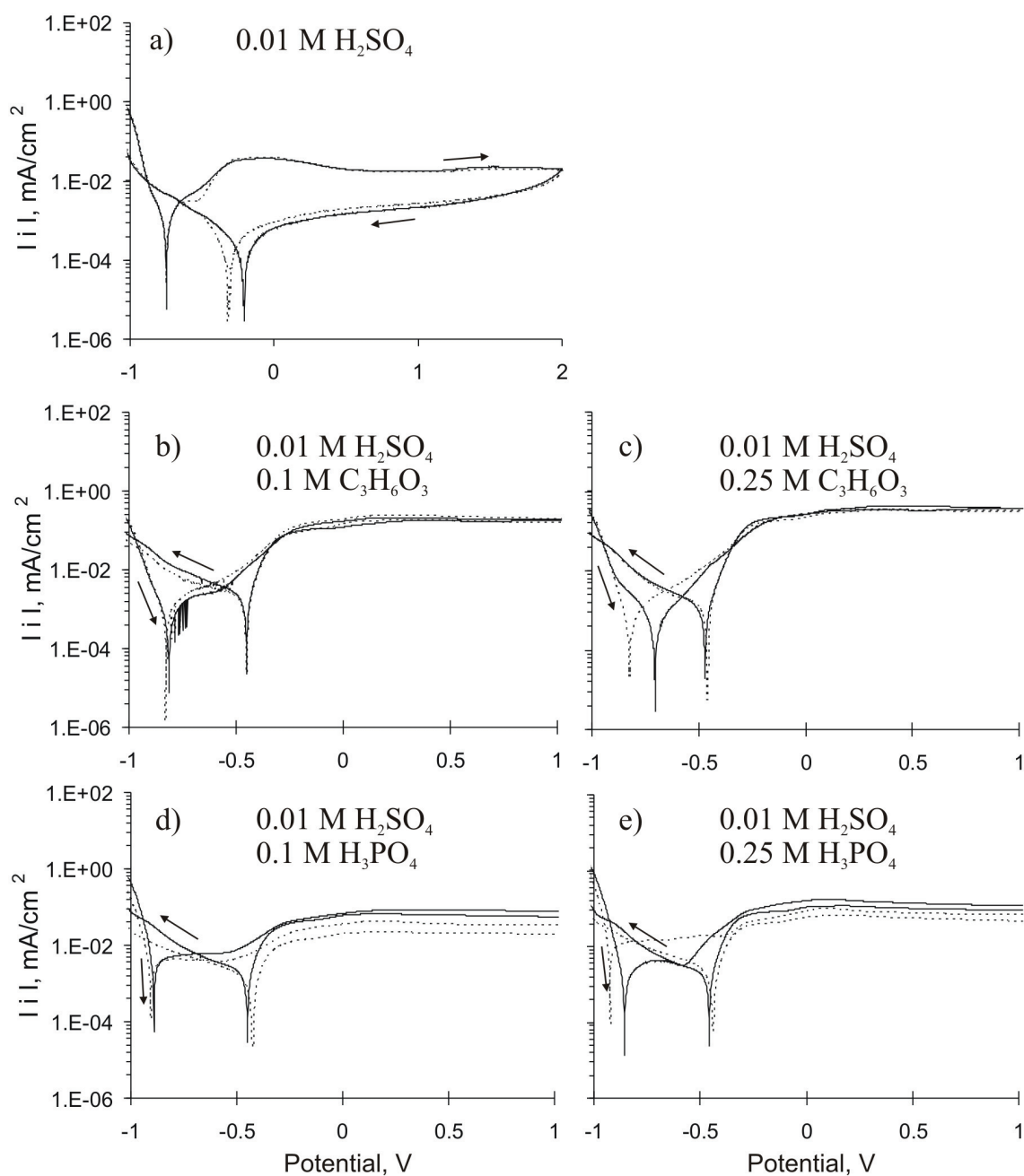


Figure 3.3 Tungsten polarization curves in different solutions with upwards and backwards measurement directions. The results of two independent measurements in each solution are plotted.

3.2.2. Potentiostatic Polarization

Quasi potentiostatic polarization curves are given in Figure 3.4 and Figure 3.5. The potential was increased from -1 V up to 0.8 V, every 120 s with a potential step of 0.2 V.

The presence of both phosphoric and lactic acid affects the shape of quasi potentiostatic polarization curves during the longer period of passivation (120 s) and leads to the augmentation of the current (Figure 3.4). Explained effect is more pronounced for lactic acid than for phosphoric acid. Rotating disk electrode was used to investigate the influence of mass transport on the passivation kinetics. Values of current density increase for all examined solutions in the tests with rotating electrode (Figure 3.5) comparing to the tests with static disk electrode (Figure 3.4). This is caused by higher dissolution rates at rotating disk electrode.

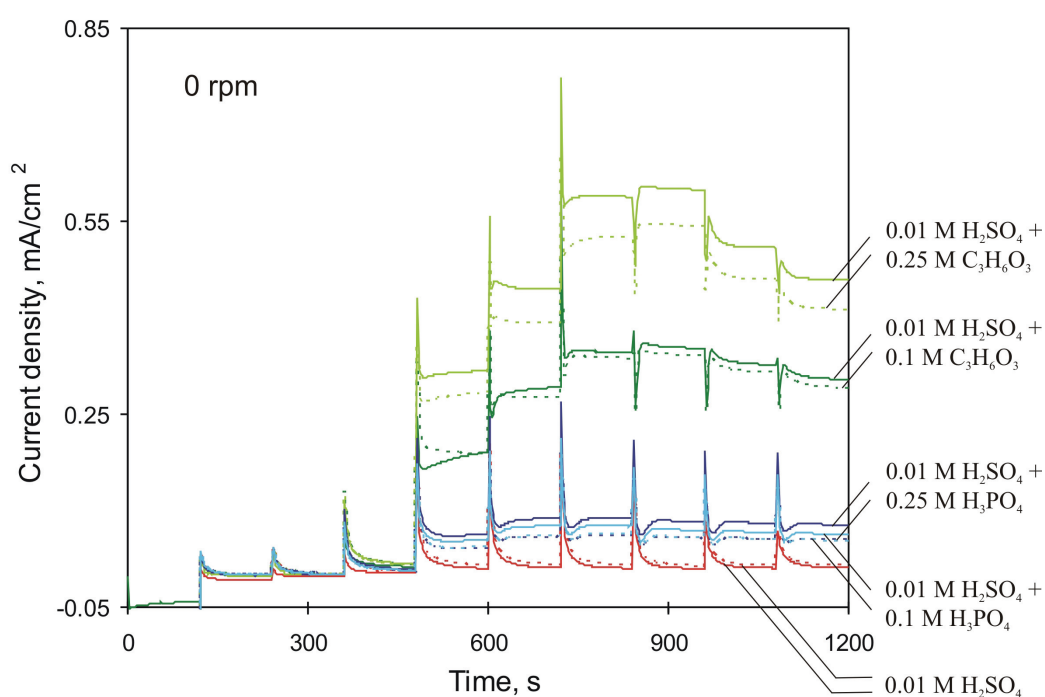


Figure 3.4 Quasi potentiostatic polarization of tungsten in different solutions (0 rpm).

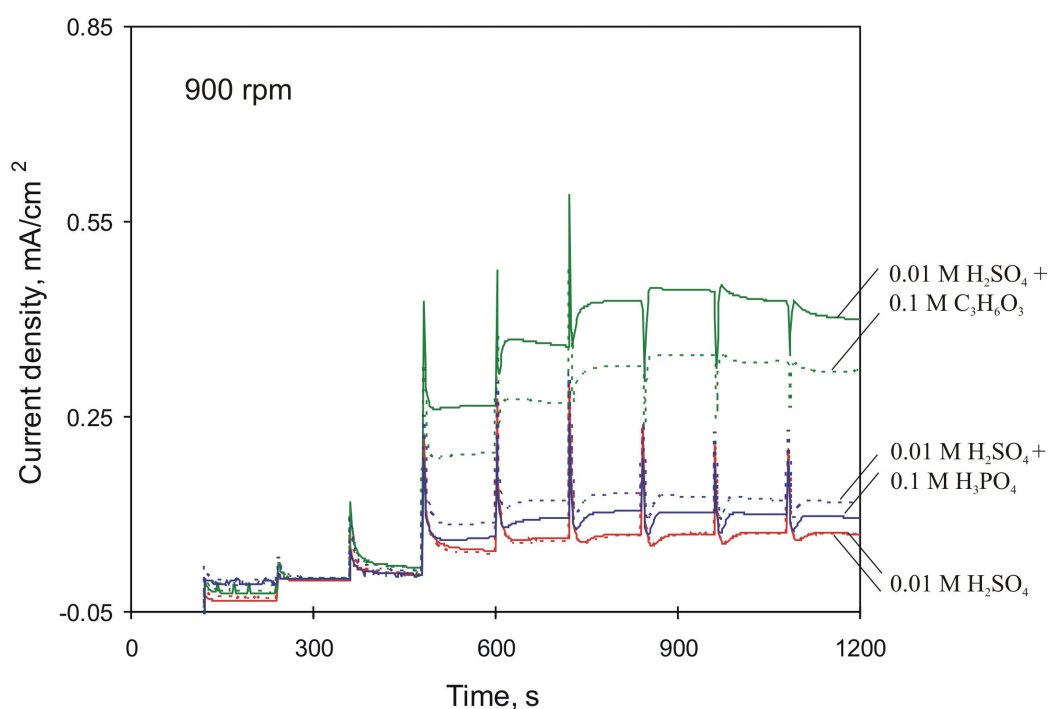


Figure 3.5 Quasi potentiostatic polarization of tungsten in different solutions (900 rpm).

Figure 3.6 shows typical polarization curves of tungsten in 0.01 M H_2SO_4 obtained using the stabilised passive current values at the end of each period of 120 s (Figure 3.4 and Figure 3.5) of the quasi potentiostatic measurements, at 0 rpm, 900 rpm and 1600 rpm. The current is negative up to a potential of -0.6 V. Above -0.4 V the current transient exhibits the typical passive behavior characterised by an initial very high current followed by a decrease to the final steady state value plotted in Figure 3.6. The polarization curve in Figure 3.6 at 0 rpm does not exhibit a peak and corresponds to the reverse direction of the curve given in Figure 3.3 a. When the polarization is performed with the sufficient time for passivation the peak does not appear. The current density in the passive region at 0 rpm has the value of an approximately 0.02 mA/cm^2 .

Rotation significantly influences the current in the passive plateau. The effect of rotation is pronounced above a potential of -0.2 V where the current at 900 rpm is approximately 5 times higher than the current on static electrodes. The enhancement of anodic current by electrode rotation was already reported in the literature and related to the increased dissolution reaction of the WO_3 passive films which kinetics is under mass

transport control [25]. Current is increasing when increasing rotation rate from 900 rpm up to 1600 rpm.

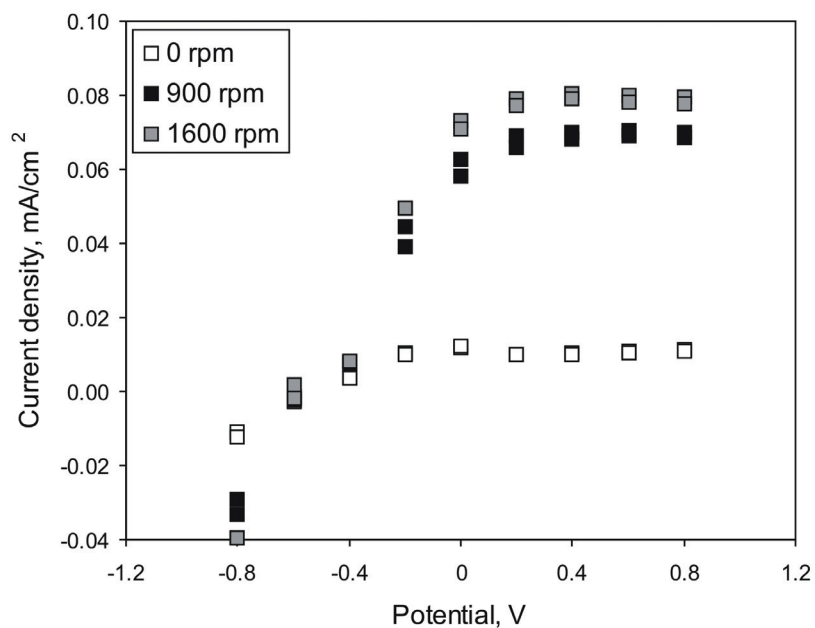


Figure 3.6 Tungsten polarization curve in 0.01 M H_2SO_4 measured at 0 rpm, 900 rpm and 1600 rpm.

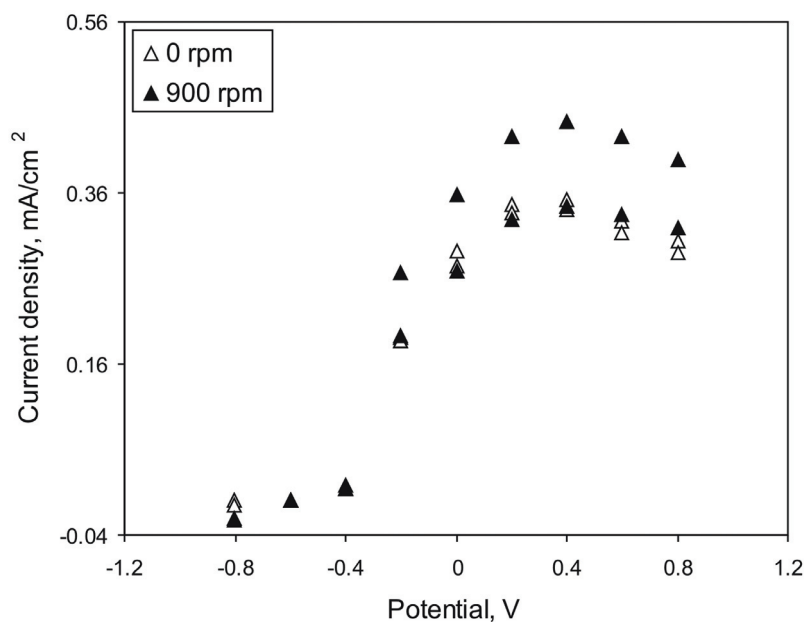


Figure 3.7 Tungsten polarization curve in the presence of 0.1 M $C_3H_6O_3$ measured at 0 rpm and 900 rpm.

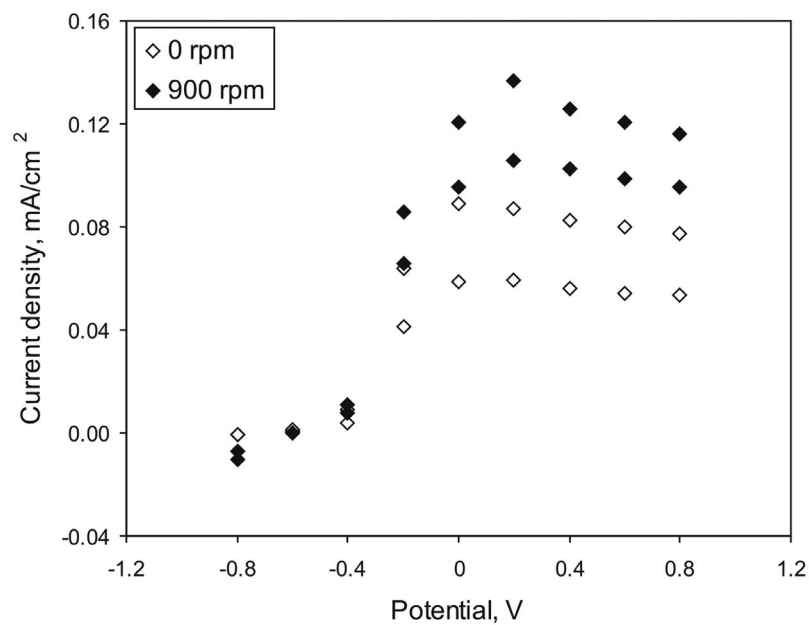


Figure 3.8 Tungsten polarization curve in the presence of 0.1 M H₃PO₄ measured at 0 rpm and 900 rpm.

The polarization curves of tungsten shown in Figure 3.7 and Figure 3.8 (obtained in the same way as the curves in Figure 3.6) show that the effect of rotation is less pronounced in the presence of lactic and phosphoric acid.

3.2.3. Passivation Transients

Short Passivation Period (1 s)

The passivation transients measured by switching potential from -1 V to 0.2 V in 0.01 M H_2SO_4 are given in Figure 3.9. The current density decreases and the passivation of the surface takes place. The reproducibility of the three independent measurements is good.

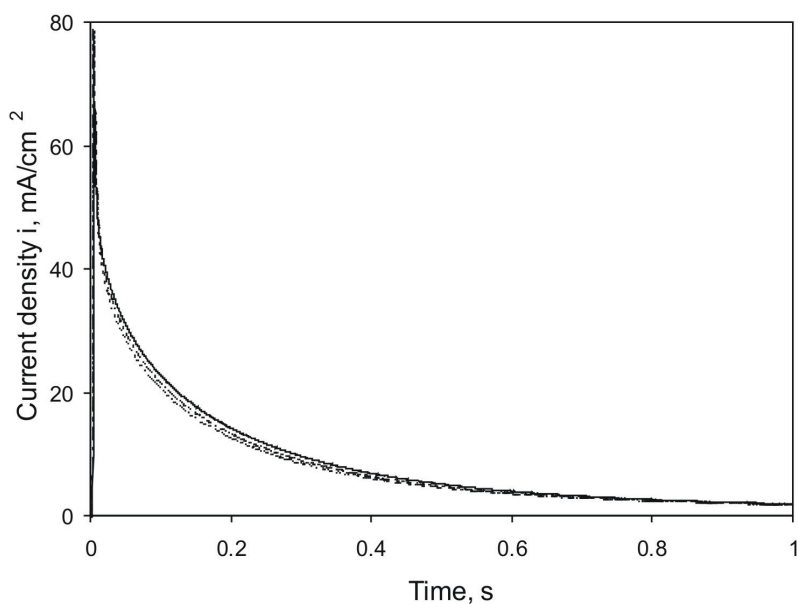


Figure 3.9 Passivation transients of the stationary tungsten electrode measured in the 0.01 M H_2SO_4 solution by switching potential from -1 V up to 0.2 V. The results of three independent measurements are plotted.

Figure 3.10 shows potential step passivation transients measured in different solutions for different imposed electrode potentials, at the rotation rate of 0 rpm. In the presence of lactic and phosphoric acid the measurements were performed by switching potential from cathodic -1 V to only three chosen potentials in separated experiments. The shapes of transients in all solutions are typical for passivating electrodes, where the initial high current decreases rapidly because of the formation and growth of the passive film. According to the shape of the transients, the passivation in the presence of phosphoric acid is faster, but the peak current is higher, compared to other two solutions. The double peak is observed for the passivation transient measured in the presence of phosphoric acid at 1 V (Figure 3.10 c). This is due to the higher conductivity and lower values of the ohmic drop

in this solution, which led to reach the limit of the measuring equipment and to the saturation of current. Instead of a double peak, only one higher peak should exist.

The passivation charge density, Q_p , represents the amount of metal that need to be oxidized to form the passive film at the selected potential. It was calculated by integrating the current density, i , from 0.003 s up to a time of 0.5 s (see Chapter 2.4.1):

$$Q_p = \int_{0.003}^{0.5} i dt \quad (3.3)$$

The calculated passivation charge densities are given in Table 3.3 and Table 3.4 and represent average value over three experiments. In practice the determination of passivation charge densities, Q_p , presents great difficulties. The values of passivation charge densities measured in independent electrochemical experiments depend not only on a given metal, environment and imposed potential but also on geometrical and experimental factors. [40] The tungsten sample used for passivation kinetics measurements had a surface larger than a contact surface in the tribocorrosion tests. Therefore, the values of passivation charge densities given in Table 3.3 and Table 3.4 do not represent the absolute values, but are of the same order of magnitude as the real passivation charge densities and can be suitably used for comparison purposes. The results given in Table 3.3 and Table 3.4, show that the calculated passivation charges are similar for a given potential in all three solutions for the integration period of 0.5 s. Within this time frame the critical factor is the electrode potential. Interestingly, mass transport conditions do not significantly affect the passivation charge densities (Table 3.3) in the short passivation period. This can be explained by the fact that during the very initial passivation time, film dissolution does not contribute significantly to the overall current.

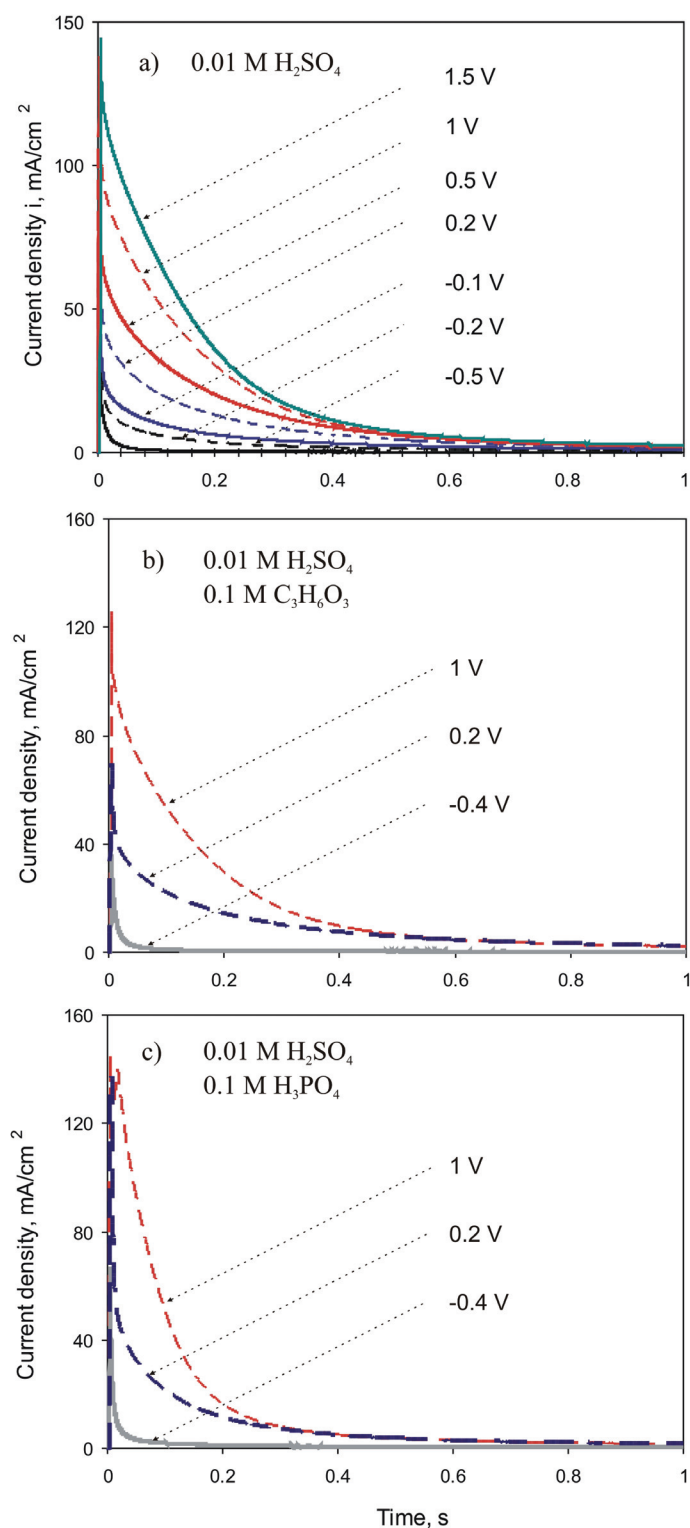


Figure 3.10 Potentiostatic current transients measured on cathodically prepolarised tungsten electrodes in different solutions at the rotation rate of 0 rpm.

Table 3.3

Influence of the electrode potential and rotation rate on the passivation charge densities measured in 0.01 M H₂SO₄.

Potential, V	0 rpm Q _p , μC/mm ²	1200 rpm Q _p , μC/mm ²
-0.5	5 ± 0	6 ± 1
-0.2	25 ± 0	28 ± 2
-0.1	33 ± 3	36 ± 3
0.2	72 ± 3	67 ± 4
0.5	107 ± 3	99 ± 1
1.0	157 ± 1	155 ± 8
1.5	193 ± 11	192 ± 14

Table 3.4

Influence of the electrode potential and solution chemistry on the passivation charge densities measured at 0 rpm.

Potential, V	0.01 M H ₂ SO ₄	0.01 M H ₂ SO ₄ + 0.1 M C ₃ H ₆ O ₃	0.01 M H ₂ SO ₄ + 0.1 M H ₃ PO ₄
	Q _p , μC/mm ²	Q _p , μC/mm ²	Q _p , μC/mm ²
-0.5	5 ± 0		
-0.4		7 ± 1	8 ± 2
0.2	72 ± 3	71 ± 3	68 ± 4
1.0	157 ± 1	147 ± 9	141 ± 1

Long Passivation Period (120 s)

The passivation transients measured for the passivation period of 120 s in the 0.01 M H₂SO₄ at the imposed potentials of 0.2 V and 1 V and the rotation rate of 0 rpm and 900 rpm are given in Figure 3.11. Good reproducibility of the measurements was observed. The dissolution rate, according to Figure 3.11, depends on the rotation rate, but not on the electrode potential. Olsson et al. [22] found that the growth fraction of tungsten, a factor characterising the part of anodic current serving for film growth, varies during passivation from an initial value of 100% to a steady state value of approximately 0.5 attained after 10 seconds.

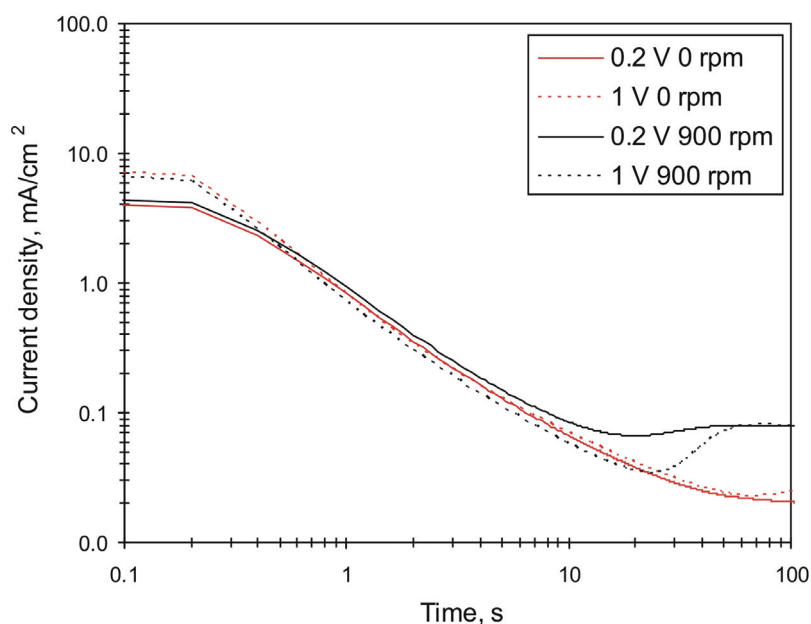


Figure 3.11 Typical passivation transients in the 0.01 M H_2SO_4 for the imposed potentials of 0.2 V and 1 V (rotation rate 0 and 900 rpm).

The passivation transients measured for the passivation period of 120 s (as explained in Chapter 3.1.1) in the 0.01 M H_2SO_4 + 0.1 M $C_3H_6O_3$ and in the 0.01 M H_2SO_4 + 0.1 M H_3PO_4 at the imposed potentials of 0.2 V and 1 V and the rotation rate of 0 rpm are given in Figure 3.12 and Figure 3.13, respectively. The current density in the first second of passivation for all the solutions and both potentials (0.2 V and 1 V) has the same decreasing trend. After the initial period of passivation the current density continues to decrease in the 0.01 M H_2SO_4 but in the presence of 0.1 M $C_3H_6O_3$ and 0.1 M H_3PO_4 current density starts to increase. The passivation kinetics mechanisms controlling the oxide growth and dissolution shown in Figure 3.11, Figure 3.12 and Figure 3.13 (ohmic drop, high field conduction and mass transport [12]) will be discussed later in Chapter 3.3.

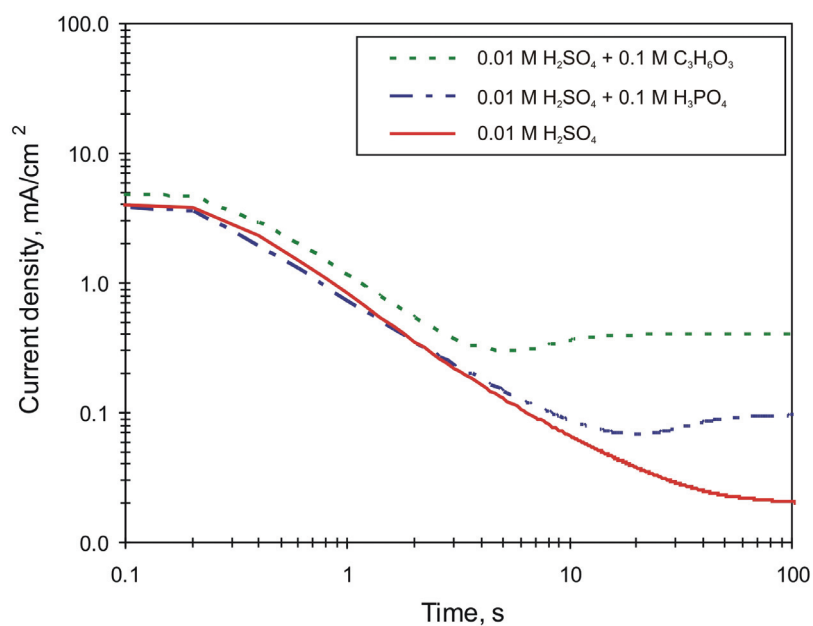


Figure 3.12 Typical passivation transients for different solutions at the imposed potential of 0.2 V.

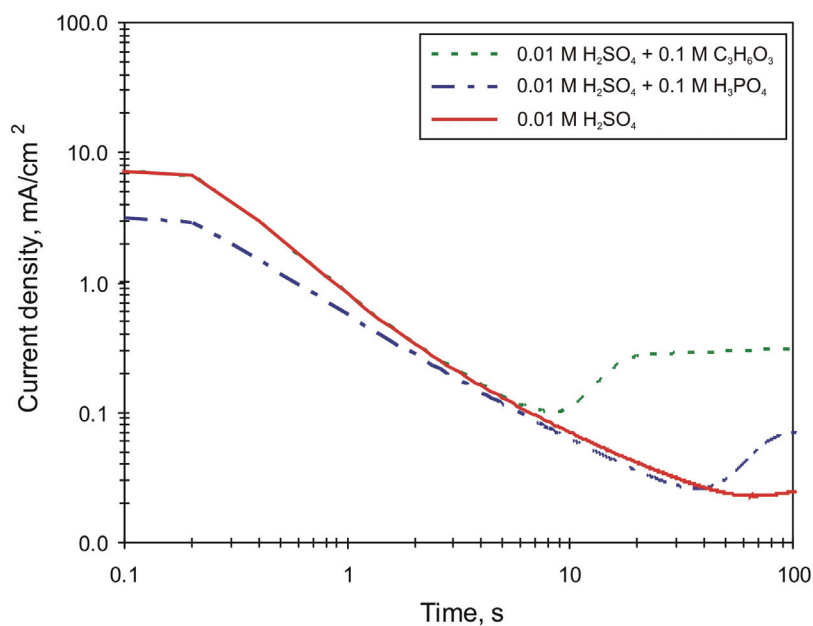


Figure 3.13 Typical passivation transients for different solutions at the imposed potential of 1 V.

3.2.4. Passive Film Composition and Thickness

Surface Characterization in 0.01 M H₂SO₄

The potentials of -0.5 V, -0.2 V, -0.1 V, 0.2 V, 0.5 V, 1 V and 1.5 V, which lie in the anodic part of the curve measured in the 0.01 M H₂SO₄ solution (Figure 3.3 a), were selected for the surface analysis. The potential of -1 V was also selected as reference for the cathodic domain. The AES and XPS survey spectra revealed the presence of tungsten, oxygen and carbon. The presence of the latter element usually results from surface contaminations occurring during sample transfer. Thus, this element was not considered for further analysis.

The XPS W_{4f} peak could be divided in two contributions corresponding to the W⁶⁺ oxide (passive film) and the metallic tungsten signal (metal underneath the oxide film), as presented in Figure 3.14. The binding energies for metallic W and W⁶⁺ are 31.4 eV and 36 eV, respectively. [62]

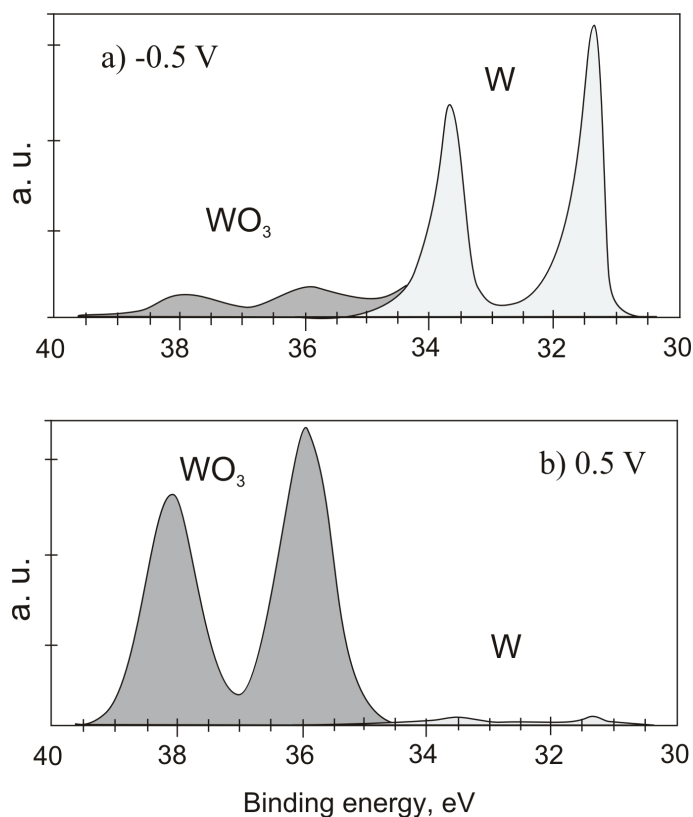


Figure 3.14 Tungsten XPS spectrum for imposed potentials of: a) -0.5 V and b) 0.5 V.

Table 3.5

Influence of the electrode potential on the signal peak area of metallic tungsten and WO_3 .

Potential, V	W, %	WO_3 , %
-1.0	99.0	1.0
-1.0	98.0	2.0
-0.5	88.6	11.4
-0.5	87.9	12.1
-0.2	84.2	15.8
-0.2	85.1	14.9
-0.1	78.1	21.9
-0.1	53.2	46.8
0.2	16.1	83.9
0.2	25.3	74.7
0.5	0.9	99.1
0.5	1.1	98.1
1.0	3.4	96.8
1.0	1.9	98.1
1.5	1.2	98.8
1.5	0.2	99.8

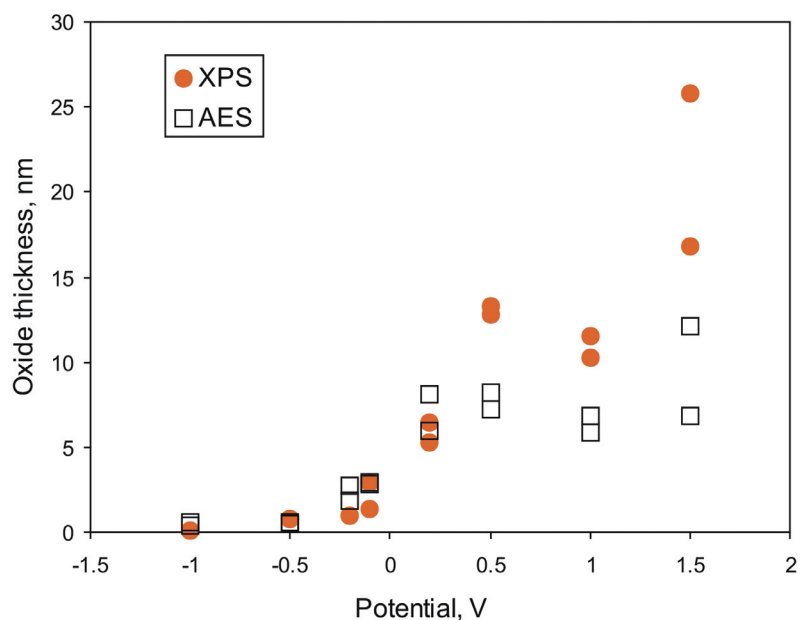


Figure 3.15 Evolution of the oxide thickness on tungsten with potential.

No other tungsten oxidation state than 0 and 6+ could be identified. Peak areas of the metallic tungsten and WO_3 signals are given in Table 3.5. The L_{XPS} film thickness is plotted in Figure 3.15 and in Table 3.6 as a function of potential.

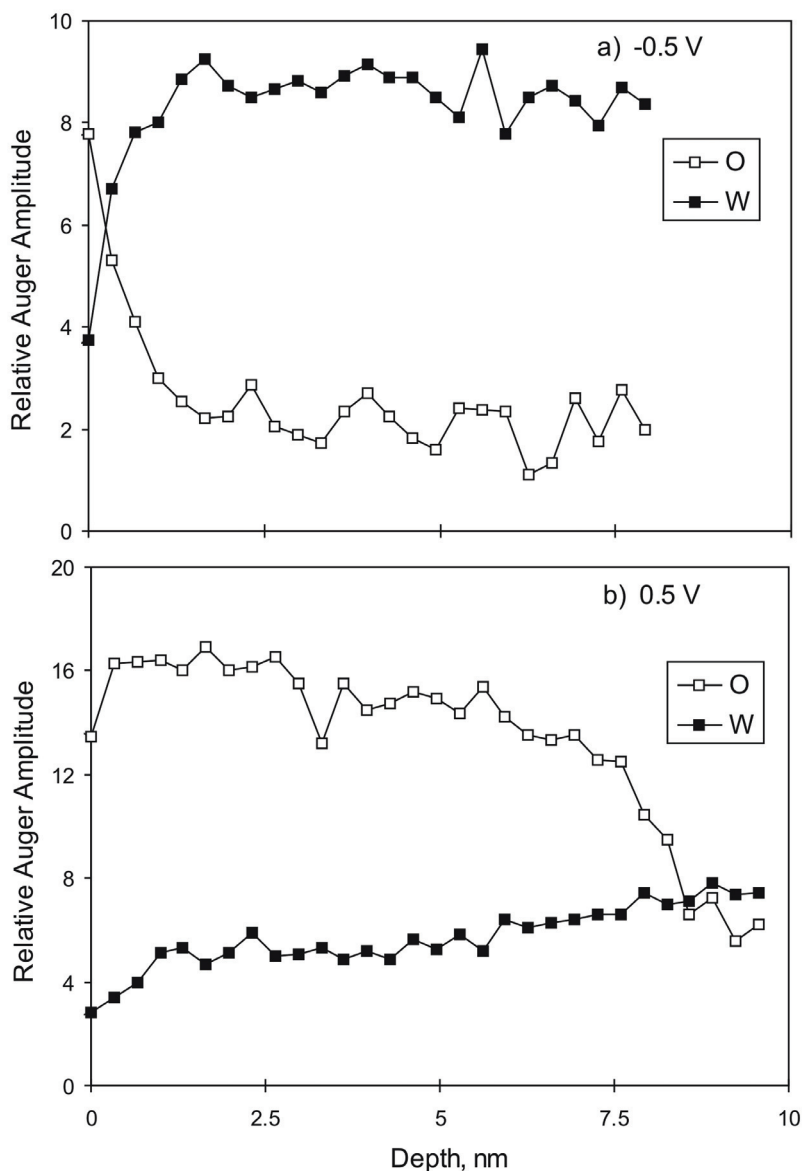


Figure 3.16 AES depth profiles of tungsten samples polarised at -0.5 V and 0.5 V.

Figure 3.16 presents typical Auger depth profiles for samples polarised at potential of -0.5 V and 0.5 V. All the profiles show a transition from the oxygen rich passive film to the base metal. Thickness L_{AES} values are plotted in Figure 3.15 and in Table 3.6. Three domains can be identified in Figure 3.15 regarding the L_{AES} . At the potentials below -0.5 V the thickness value is lower than 1 nm. From -0.5 V the AES thickness increases linearly

with the potential. Above the imposed potential of 0.5 V, the thickness does not vary significantly with potential.

Table 3.6

Influence of the electrode potential on the WO_3 thickness (L), calculated from the XPS and AES measurements.

Potential, V	L_{XPS} , nm	L_{AES} , nm
-1.0	0.1	0.6
-1.0	0.1	0.4
-0.5	0.7	0.6
-0.5	0.8	0.5
-0.2	1.0	2.7
-0.2	1.0	1.9
-0.1	1.4	2.9
-0.1	2.9	2.8
0.2	6.4	6.0
0.2	5.2	8.1
0.5	13.3	8.2
0.5	12.8	7.2
1.0	10.2	5.9
1.0	11.6	6.8
1.5	16.8	6.8
1.5	25.8	12.1

Good agreement is found between AES and XPS film thickness values. Only at higher potentials, discrepancies appear probably due to the uncertainties in the quantification of the very small XPS peaks of metallic W found at higher potential (Figure 3.14). The scattering at the potentials beyond 0.5 V does not permit the evaluation of the clear trend and the slope of the thickness' increase.

The thickness of the native oxide is the thickness of the oxide formed on the surface of electrochemically not treated sample. That is the thickness of the oxide on the sample previously mirror polished, then rinsed with distilled water, dried with compressed air and exposed to the air. To determine the native oxide thickness we can use the oxide formed at the surface of the sample subjected to polarization tests at the imposed cathodic potential of -1 V. When applying this cathodic potential, the oxide film does not form during the

test. The oxide is formed after the test, during the exposure to the air and the storage of the sample until the moment when XPS and AES analysis were performed. The native oxide thickness value, L_{AES} , determined this way is 0.5 ± 0.1 nm (Table 3.6).

Surface Characterization in the Presence of Chelating Agents

According to XPS analysis after polarization at 0.2 V during 3600 s in 0.01 M H_2SO_4 + 0.1 M $C_3H_6O_3$ and in 0.01 M H_2SO_4 + 0.1 M H_3PO_4 , the tungsten surface remains mainly metallic, as shown in Figure 3.17 b and c. The amount of formed oxide film, WO_3 , in both solutions is not significant. On the contrary, at the same imposed electrode potential of 0.2 V in the 0.01 M H_2SO_4 the WO_3 peak is more pronounced than metallic W_{4f} peak (Figure 3.17 a).

For the samples polarised in the presence of 0.1 M $C_3H_6O_3$ (Figure 3.17 b) the same surface composition is observed compared to the samples polarised in the presence of 0.1 M H_3PO_4 (Figure 3.17 b). In the presence of phosphoric acid no absorption of phosphate was detected on the tungsten surface using XPS. It is necessary to mention that all the samples were rinsed with distilled water after polarization and before XPS analyses.

Thicknesses of the WO_3 formed on the tungsten surface in presence of 0.1 M $C_3H_6O_3$ and 0.1 M H_3PO_4 at the imposed electrode potentials of 0.2 V and 1 V are given in Table 3.7.

Thickness L_{AES} of the WO_3 in the presence of 0.1 M $C_3H_6O_3$ after 10 s of passivation (the lowest point of the transient in Figure 3.12 for the 0.01 M H_2SO_4 + 0.1 M $C_3H_6O_3$) is 1.5 ± 0.1 nm. No difference in the oxide thickness is found for the same conditions in the region after 100 s where L_{AES} is 1.4 ± 0.2 nm.

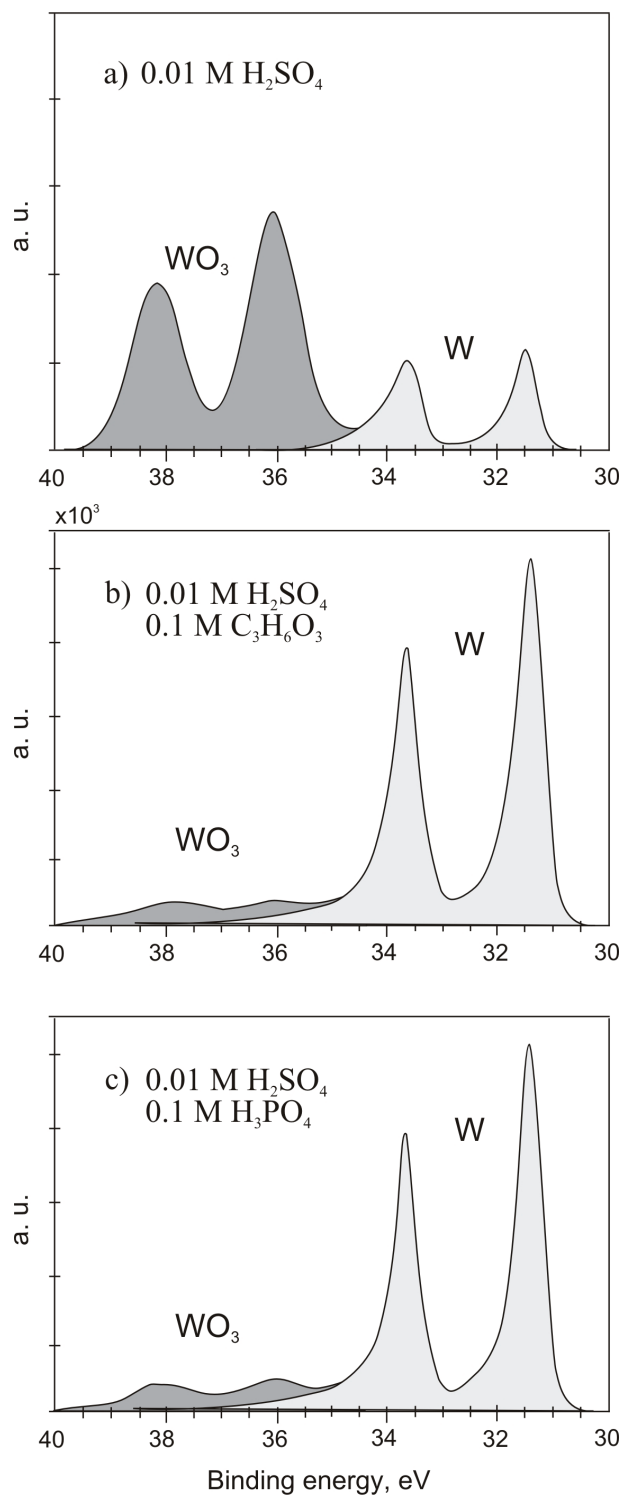


Figure 3.17 Tungsten spectrums for imposed potential of 0.2 V in the solutions: a) 0.01 M H_2SO_4 , b) 0.01 M H_2SO_4 + 0.1 M $\text{C}_3\text{H}_6\text{O}_3$ and c) 0.01M H_2SO_4 + 0.1 M H_3PO_4 .

Table 3.7

Influence of the solution's composition and electrode potential on the WO_3 thickness (L) calculated from the XPS and AES measurements.

Solution	L_{XPS} , nm	L_{AES} , nm	L_{XPS} , nm	L_{AES} , nm
0.01 M H_2SO_4 +...	0.2 V		1 V	
	6.4	6.0	10.2	5.9
	5.2	8.1	11.6	6.8
0.1 M $C_3H_6O_3$	0.3	0.7	2.1	1.9
0.1 M $C_3H_6O_3$	0.2	0.6	2.0	1.9
0.1 M H_3PO_4	0.5	1.3	1.0	1.6
0.1 M H_3PO_4	0.4	0.8	0.9	1.7

3.3. Discussion

The quasi potentiostatic polarization curves show that rotation significantly influences the current in the passive plateau (Figure 3.6). Rotation enhances mass transport and thus dissolution of the WO_3 passive film [22]. As a consequence, the passive film becomes thinner and the current increases (Figure 3.6). The rotation rate does not influence the passivation transients measured up to 1 s of passivation (Table 3.3). A possible reason is that during the very initial time the dissolution reaction of the passive film is negligible and the passed current serves essentially for film growth as already observed by Olsson et al [22]. The passivation charge density measured in all solutions and at different rotation rates and calculated for the first 0.5 s of passivation (Equation 3.3), increases linearly with the imposed electrode potential (Figure 3.18). Rotation rate and the presence of chelating agents do not influence the passivation kinetics in the short period of passivation.

$$Q_p = f(E) \quad (3.4)$$

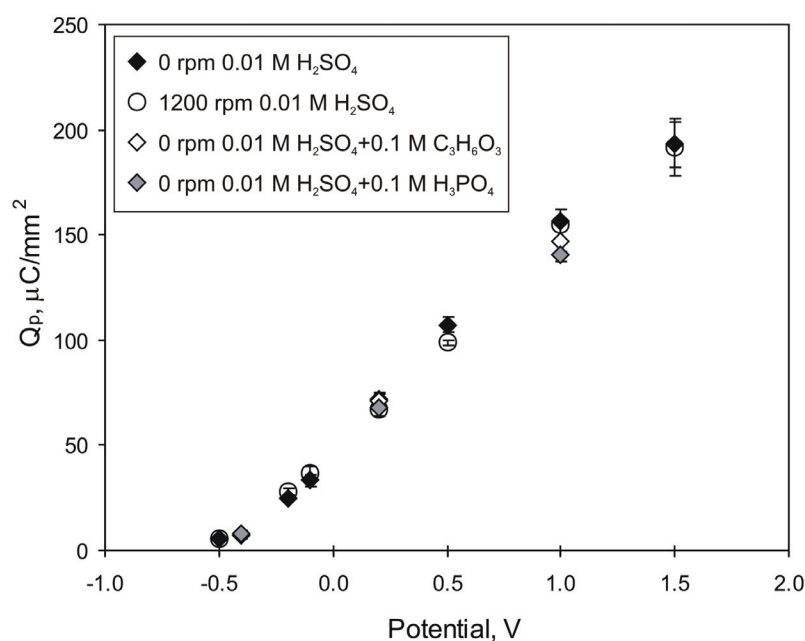


Figure 3.18 Influence of the imposed electrode potential on the passivation charge density of tungsten in different solutions, calculated by integrating the current density up to 0.5 s.

Quasi potentiostatic measurements showed the important influence of the mass transport on the corrosion behavior of tungsten after the initial period of passivation (Figure 3.4 and Figure 3.5).

During the current density – time transients' measurements performed up to 1 s of passivation, the passive current density is approximately equal for both static and rotating electrode (Figure 3.18) and in this period oxide film is growing on the surface. As explained in Chapter 2.2, the current density at the interface oxide-electrolyte can be expressed as the sum of the rate of film formation and the rate of metal-ion dissolution (or oxide dissolution). In principle passivation charge serves for both, for the growth of the passive film as well as for the metal dissolution. Possibly for potentials above 0.5 V the fraction of charge serving for oxide growth remains constant and the excess charge is consumed by dissolution. Therefore, the thickness of the passive film for 0.5 V, 1 V and 1.5 V does not change significantly, while passivation charge increases with potential (Figure 3.15). The rotation provokes passive dissolution during the longer passivation period where not all the charge is converted to oxide film growth. The reaction of WO_3

dissolution (Equation 2.9) does not reach equilibrium and the dissolution process is always present.

The passivation behavior of tungsten shown in Figure 3.11 can be depicted using the schema in Figure 3.19. At the beginning of polarization the current in the initial flat part is limited by the ohmic resistance of the solution. [36] Further on passivation occurs and current density decreases. Passivation transients for both systems, with and without rotation, are similar at the beginning of passivation. After the very short period of ohmic controlled current, further on within the first few seconds of passivation current decreases with and without rotation. Thus, within this period the rotation does not affect the film growth which could be governed by high field conduction [12]. This region characterizes the film growth limited by ion conduction (migration) through the oxide film. On the stationary disk electrode (0 rpm) the film continues to grow over longer period while on rotating disk electrode a potential dependent steady state film thickness is reached rapidly. After initial few seconds of passivation, rotation influences the dissolution of the oxide formed on the tungsten surface. This dissolution is mass transport (diffusion) controlled and it impedes the film growth.

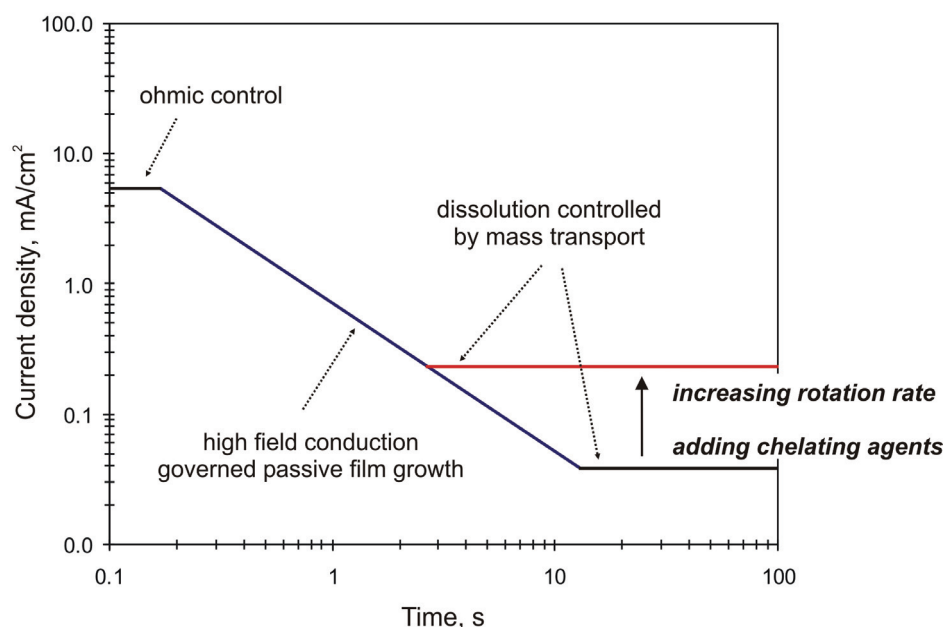


Figure 3.19 Schematic diagram of the influence of electrode rotation on passivation transients in 0.01 M H_2SO_4 .

As previously presented, the reaction of WO_3 formation and dissolution can be expressed by Equation (2.9). Dissolution of the WO_3 depends on the gradient of concentration of the tungstate ions in the Nernst diffusion layer [12] and on the thickness of the layer. With rotation the thickness of the Nernst diffusion layer, δ , decreases (Equation 2.13) [12], and the dissolution of WO_3 and the current density increase.

The passivation behavior of tungsten in the presence of 0.1 M $\text{C}_3\text{H}_6\text{O}_3$ and 0.1 M H_3PO_4 is similar to the behavior observed under rotation in sulphuric acid. In the initial second of passivation the film growth is ohmic controlled till 0.1 s and afterwards controlled by high field conduction. Beyond the initial period of 1 s of passivation, the growth of the oxide in different solutions (Figure 3.12 and Figure 3.13) can be explained schematically using Figure 3.19. After the high field conduction governed growth in the presence of lactic and phosphoric acids the mass transport controlled dissolution of the surface oxide occurs. Chelating agents lactic and phosphoric acids are probably forming complex compounds with the tungstate ions (Figure 2.6). Chelating agents are known as the substances which form chemical complexes with metallic ions, by replacing water molecules in the hydration sphere of a dissolved metal ion. These complexes are always consisted of the metal ion bounded to two or more atoms of the chelating agent. The presence of chelating agents affects the dissolution reaction stoichiometry of the metal, leading to a lower standard potential and facilitating corrosion. [12] By complexing the WO_4^{2-} ions lactic and phosphoric acids are decreasing the $c_{B,b}$, the concentration of WO_4^{2-} ions in the bulk solution (Equation 2.13). The concentration of WO_4^{2-} is not stationary with time. Therefore, the gradient of the tungstate ions concentration in the Nernst diffusion layer increases. The rate of the partial anodic reaction (tungsten oxide dissolution) increases and limiting current density (i_l) increases (Equation 2.13). This leads to thinning of the WO_3 on the surface. Therefore passive oxide film can not grow and can not reach the thickness observed after polarization in the 0.01 M H_2SO_4 solution.

XPS analysis after passivation at 0.2 V in the 0.01 M H_2SO_4 (Figure 3.17 a) are showing intense WO_3 peaks, while in the presence of 0.1 M $\text{C}_3\text{H}_6\text{O}_3$ the WO_3 peak is weak. Thickness of the oxide film formed in the presence of 0.1 M $\text{C}_3\text{H}_6\text{O}_3$ at 0.2 V is similar to the thickness of the native oxide at the tungsten surface formed in the 0.01 M

H_2SO_4 (Table 3.6 and Table 3.7). In the presence of 0.1 M H_3PO_4 at 0.2 V the oxide peak is slightly more intense comparing to the presence of 0.1 M $\text{C}_3\text{H}_6\text{O}_3$.

Even though peaks of current density are different during polarization in different solutions (Figure 3.10), passivation charges calculated for the first 0.5 s of passivation have the similar values. Maximal transient's current density (peak of the current transient) (Figure 3.20) depends on conductivity of the solution and linearly increases with imposed potential. The slope abruptly increases when increasing solution conductivity (Chapter 3.1.1 and Table 3.2). The peak current density is controlled by the ohmic resistance of the solution. [12][36] The highest conductivity (presence of phosphoric acid) implies the steepest slope. The point corresponding to the presence of phosphoric acid at the potential of 1 V can not be placed on the line connecting the points corresponding to -0.4 V and 0.2 V for the same solution (Figure 3.20). As explained before, due to the limitation of the measuring system its measured value is lower than the real value (see Chapter 3.2.3).

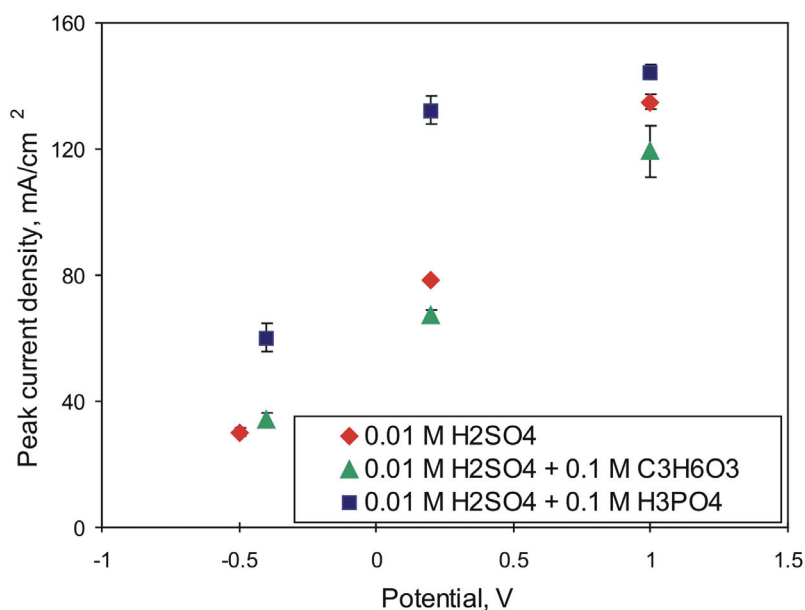


Figure 3.20 Maximal transient's current density, I_{peak} vs. potential.

3.4. Conclusions

XPS analyses suggest that in the passive films formed on the tungsten surface in the whole potential range from -1 V up to 1.5 V MSE, tungsten remains with the valence 6+. Nevertheless, XPS analyses are not taken in situ and maybe the air oxidation could have an influence on the found oxide stoichiometry.

XPS and AES analyses show that the thickness of the WO_3 increases when potential increases in the same range from -1 V up to 1.5 V. The thickness change is not uniform on the whole potential range. Up to the potential of -0.2 V, the thickness remains very low and approximately 1 nm. From -0.5 V up to 0.5 V the thickness increases linearly with potential and above 0.5 V the thickness increase slope is less pronounced.

Rotation influences the thinning of the Nernst diffusion layer and the enhancement of the WO_3 dissolution which is mass transport controlled. But the rotation rate does not influence the passivation kinetics in the initial passivation period of 1 s. This can lead to the conclusion that in the very initial passivation period, film growth dominates over film dissolution.

The presence of chelating agents lactic and phosphoric acid in the 0.01 M H_2SO_4 solution changes the electrochemical (corrosion) behavior of tungsten. Current density increases in the presence of lactic and phosphoric acid depending on acids concentration.

By complexation of dissolved ions from the WO_3 surface film, most probably WO_4^{2-} ions, lactic and phosphoric acids are decreasing the concentration of tungsten ions in the bulk solution. Therefore, the WO_3 dissolution is accelerated and the oxide film formation is limited.

Tribocorrosion should be influenced by electrode potential, while chelating agents should facilitate etching. Chelating agents are decreasing dramatically the thickness of the oxide film formed on tungsten by enhancing the dissolution. This dissolution was found to appear during longer period of passivation (120 s), while one cycle of rubbing in a tribocorrosion test lasts typically 1 s.

CHAPTER 4

4. Effect of Experimental Parameters in Tribocorrosion

The tribocorrosion test procedure optimisation includes the investigation of the effect of functional parameters (frequency, cathodic cleaning, duration of rubbing, pre-passivation duration) on the output parameters of tribocorrosion tests. The output parameters are coefficient of friction (COF), current enhancement due to rubbing (I_r) and wear track volume (V_{wt}). All the tests performed in order to optimize the experimental technique are undertaken in the 0.01 M H_2SO_4 solution.

4.1. Tribocorrosion Experiments

Tungsten disk and Al_2O_3 ball were chosen as rubbing specimen. Tungsten samples were fabricated by machining bars supplied by GoodFellow (purity 99.95 %) in form of 20 mm diameter and 6 mm thick disks. Micro hardness of the samples was 3.7 ± 0.1 GPa measured with a load of 200 g. Samples preparation for the tests consisted of polishing on automatic polishing machine ABRAMINE Struers using carbon grit paper and for finish 1 μm diamond spray Struers, down to a roughness of $R_a = 0.08 \mu m$ (measured on the UBM Telefokus measurement system Messtechnik, UBC 14). The exact polishing procedure is given in the Appendix B. Prior to testing, samples were put in ultrasonic bath for 3 min, first with alcohol and then with distilled water. Afterwards, samples were dried using an argon jet.

Metallographic analyses were performed in order to determine the grain structure of tungsten samples (Figure 4.1) and eventual inclusions. Microetching solution in which the

sample was boiled for 90 s, was prepared of 100 ml distilled water and 1 ml H₂O₂ (30%). The revealed grain size is in the range from 5-40 μm.

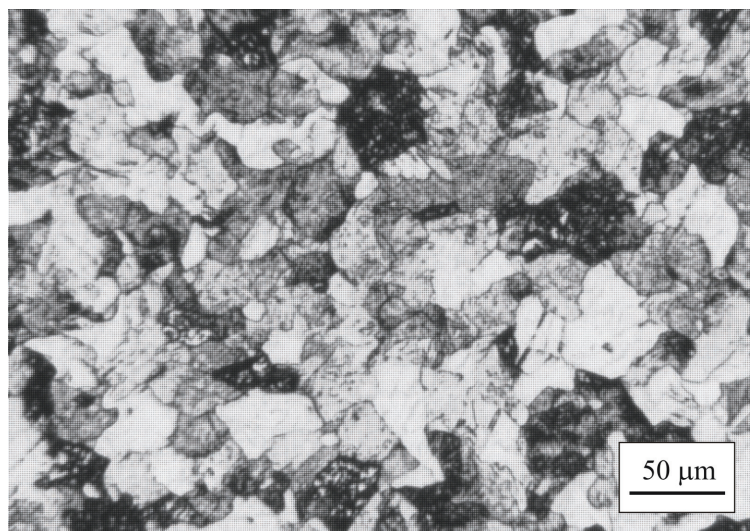


Figure 4.1 Tungsten surface after metallographic attack.

The Al₂O₃ balls (SWIP Brügg, Switzerland) were 6 mm in diameter and had maximum surface roughness of $R_a = 0.02 \mu\text{m}$ (according to manufacturer). Young's modulus and Poisson's ratio of alumina ball are 377 GPa and 0.24, respectively. Used solution for tribocorrosion tests was 0.01 M H₂SO₄. It was chosen as a model solution with a pH 1.5 corresponding approximately to pH values of technical CMP slurries.

Tribocorrosion experiments were performed on the tribometer with an integrated electrochemical setting (three-electrode cell), schematically shown in Figure 4.2. The contact configuration involved an alumina ball sliding in a reciprocating motion against the stationary tungsten plate. The horizontal reciprocating displacement of the ball loaded against the disk, placed inside the cell, is controlled by a linear drive motor (Etel S.A.) as shown in Figure 4.2. The horizontal and vertical displacements of the ball are measured by the relative movement of a laser, mounted on the arm, with respect to a stationary position sensitive detector. This way the stroke length, frequency and type of waveform can be monitored. The normal load is varied by the application of a series of weights to the arm and is measured. Both normal and tangential forces transmitted to the disk were monitored, by a multi-axial piezoelectric transducer Kistler 9152A on which the electrochemical cell is placed. The whole system is mounted on a large steel base that provides stability and certain degree of dumping.

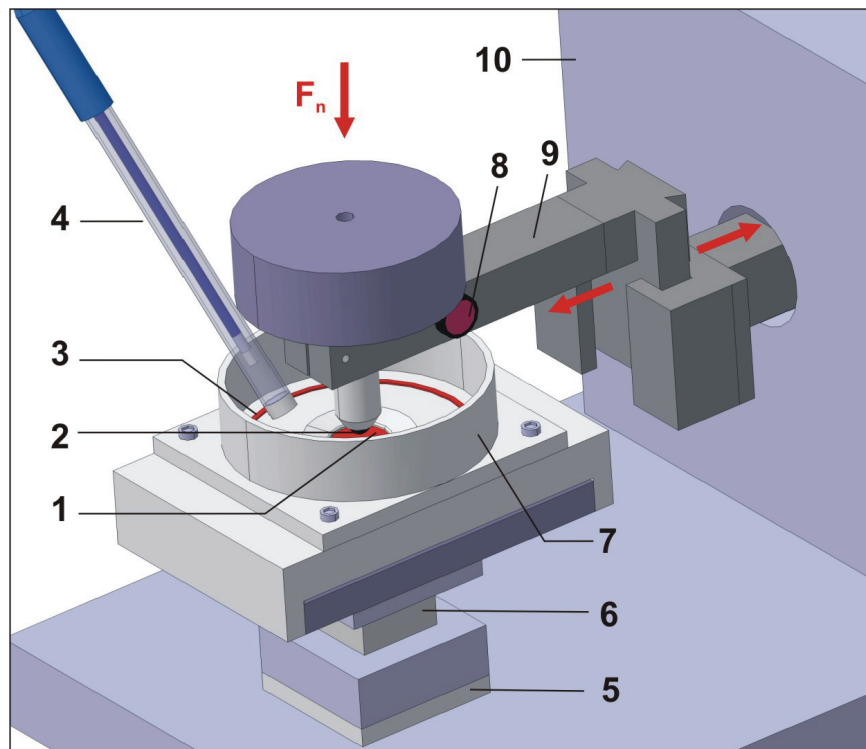


Figure 4.2 Tribocorrosimeter KT – 01: (1) metal sample – working electrode, (2) alumina ball, (3) counter electrode, (4) reference electrode, (5) electrical insulating block, (6) three – axes force transducer, (7) electrochemical cell, (8) laser, (9) drive arm and (10) linear motor.

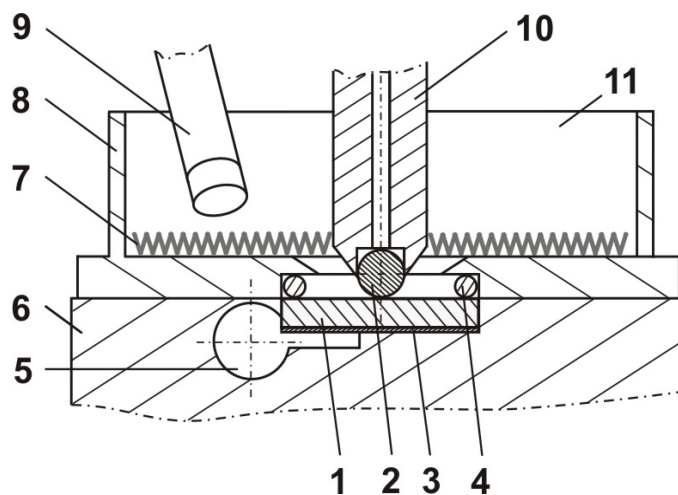


Figure 4.3 Contact geometry in the electrochemical cell: (1) metal sample – working electrode, (2) alumina ball, (3) metal contact plate, (4) O – ring, (5) switch-in for electrical connection to working electrode, (6) cell bottom part, (7) counter electrode, (8) cell upper part, (9) reference electrode, (10) ball holder and (11) electrolyte.

Working electrode (WE), tungsten disk, was kept at a controlled potential, a wound platinum wire was used as a counter electrode (CE) (Figure 4.3), and a standard mercury sulphate electrode (MSE) served as a reference electrode (RE). A Wenking LB 95 L Auto Range Laboratory Potentiostat served to control the potential of the tungsten disk. Electrochemical cell made of PMMA has a volume of 65 ml.

Mackintosh G3 with a National Instruments data acquisition card (NB-MIO-16X) and LabView software permit experimental control of the system and simultaneous acquisition of the normal force, the tangential force, the displacement in x and z direction, the imposed potential and the resultant current. The displacement in x – direction represents the stroke length and the displacement in z – direction represents the wear depth.

Coefficient of friction is acquired as the ratio of the tangential and normal force. Friction may be defined as the resistance encountered by one body in moving over another. [29] The magnitude of the frictional force, F_t , needed to move a body over a stationary counterface is known as coefficient of friction, μ or *COF*:

$$\mu = \frac{F_t}{F_n} \quad (4.1)$$

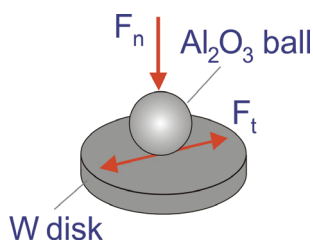


Figure 4.4 Scema of the sliding contact with applied normal load and generated friction force.

The sensitivity of the normal and friction force sensors was $F_t=3.76$ pC/N and $F_n=7.90$ pC/N, respectively. The data for all parameters were acquired in transient time scale (1000 data point per second) and in the mean time scale, as presented in Figure 4.5. Every 5 s the mean value is calculated and stored. Every 270 s a transient file of 1 s duration is stored. The coefficient of friction is determined for each stroke as the ratio of the friction force and normal force, both measured in the centre of the reciprocating path. The linear

motor providing ball motion was driven with a truncated triangular wave form with a pin held stationary for 0.125 s at each stroke end, referred as a dead time, as presented in Figure 4.5. The stroke length was 4 mm corresponding to a sliding velocity of 10.7 mm/s. Frequency of rubbing was 1 Hz. Each measurement was performed twice with new tungsten disk and alumina and ball in order to check for reproducibility.

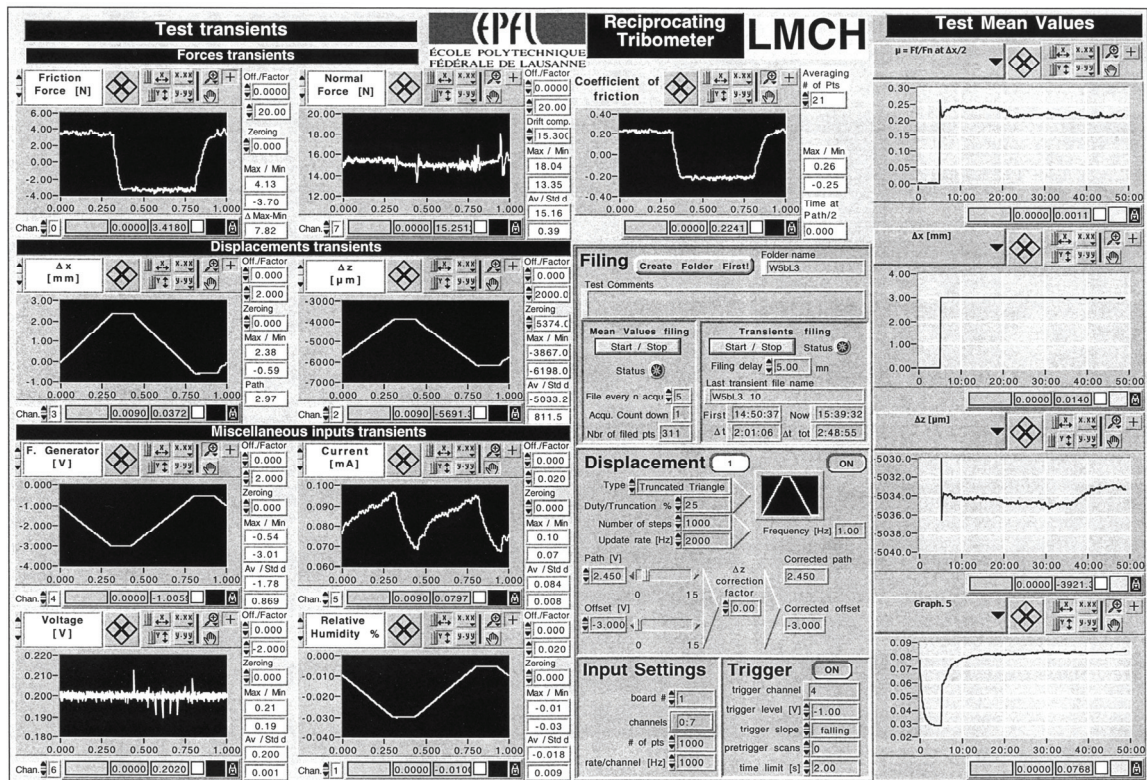


Figure 4.5 LabView software application customization page with possibility of the test transients and the test mean values acquisition.

After tribocorrosion tests, wear track's volumes were quantified using non-contact UBM Telefokus measurement system Messtechnik, UBC 14. Infrared light beam from a semiconductor laser is focused by a lens on the sample surface. The beam is reflected and diffracted by surface irregularities. The reflected beam is monitored by a photodiode. The profiles 2D are monitored by displaying surface height (z - axes) versus scan direction (x - axes). The focused spot diameter is approximately 1 μm . For the measurement range of $\pm 50 \mu\text{m}$ vertical resolution is 10 nm. The 2D profiling was performed with a point density of 1000 points/mm, speed of 0.002 mm/s and measurement rate of 20 points/s. The zero of

the z-axis was set to the unworn surface out of the wear track. Each measured signal was filtered in the Excel software using the formula $AVERAGE_{n=1}^{500}(A_n : A_{n+14})$.

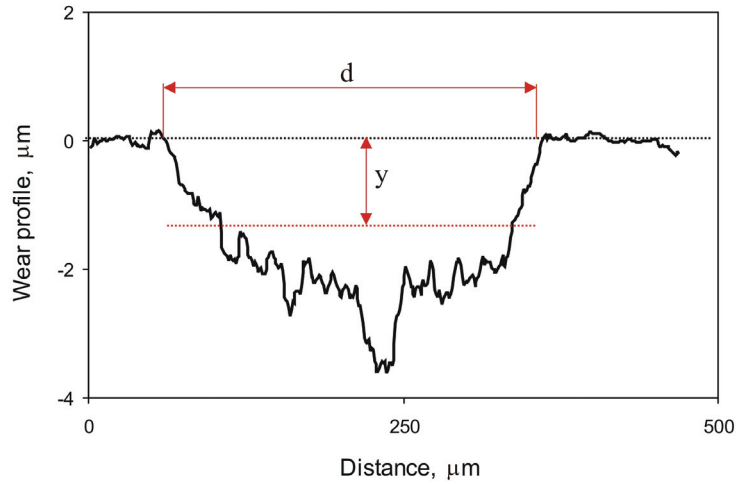


Figure 4.6 Wear track's profile obtained during rubbing at imposed 0.2 V in standard tribocorrosion test conditions.

The average cross section (Figure 4.6) was determined for three profiles across the wear track for each sample at one-fourth, one-half and three-fourth of the track length. Wear track width, d , was determined as the distance between the wear track profile intersections with the x - axes passing through the zero. Mean depth of the wear track profile, y , represents the average value of all wear track profile's points within profile width, d . Wear volume was calculated used the equation:

$$V_{wt} = \frac{l}{3} \left(\sum_{n=1}^3 y_n \cdot d_n \right) \cdot l \quad (4.2)$$

where V_{wt} is the wear track volume, y is the mean depth of the wear track, d is the width of the wear track, l is the length of the wear track (4 mm) and n is the number of measurements.

4.2. Cathodic Cleaning Pre-Treatment

Cathodic cleaning is performed before tribocorrosion tests to remove the native oxide from the tungsten surface, formed due to rinsing with distilled water after sample

preparation and exposure to the air during sample storage. Rubbing tests were undertaken without and with pre-treatment cathodic cleaning in order to investigate its influence on the resulting current. Each type of test was performed twice in order to check for reproducibility. In the tribocorrosion test procedure with cathodic cleaning, the tungsten disk was mirror polished and exposed to cathodic cleaning in the 0.01 M H₂SO₄ solution during 300 s, at imposed potential of -1.7 V. The exposed surface area of tungsten disk is 2.54 cm². Afterwards, the surface was left at open circuit potential during 300 s, and passivated by applying the potential of 0.2 V during 300 s before starting rubbing at the same potential during 3000 s. The rubbing was followed by static exposure of the sample surface at the imposed potential during 300 s. Frequency of rubbing was 1 Hz. Samples for the tests without cathodic cleaning pre-treatment were directly stabilised at open circuit potentials, so only the first step in the above explained test procedure was excluded.

Cathodic pre-treated samples showed similar coefficient of friction and current evolution during time as the non pre-treated samples (Figure 4.7 and Table 4.1). Coefficient of friction (*COF*) was calculated as the average value of acquired coefficient of friction from the moment when rubbing started till the end of rubbing.

In tribocorrosion tests at the onset of rubbing the current increased sharply due to the abrasion of the passive film (depassivation) covering the tungsten surface (Figure 4.7). The repassivation of the bare metal surface requires the oxidation of a certain amount of metal. Cyclic depassivation/repassivation phenomena maintain the current at relatively high values. After stopping rubbing the worn areas repassivate and the current decreases to the values observed before rubbing. The current enhancement due to rubbing (*I_r*) was determined by subtracting to the average current measured during rubbing the average current due to the corrosion of the electrode area outside the wear track. The latter was defined as the mean value of the currents measured just before starting rubbing and 5 minutes after stopping it.

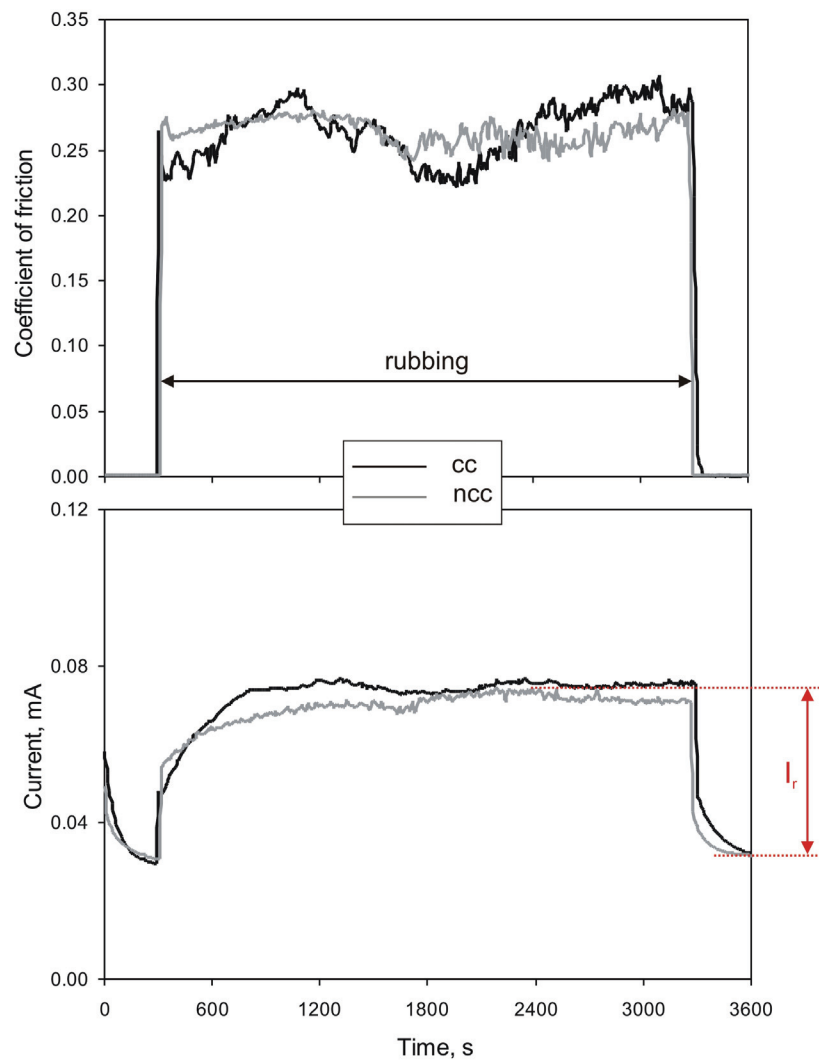


Figure 4.7 Evolution of coefficient of friction and current during rubbing with time for the cathodically pre-treated samples (cc) and non cathodically pre-treated samples (ncc).

In the transient scale corresponding to one cycle of rubbing, the measured current decreases after each stroke (during the dead time of the alumina ball) due to repassivation of the activated tungsten surface (Figure 4.8).

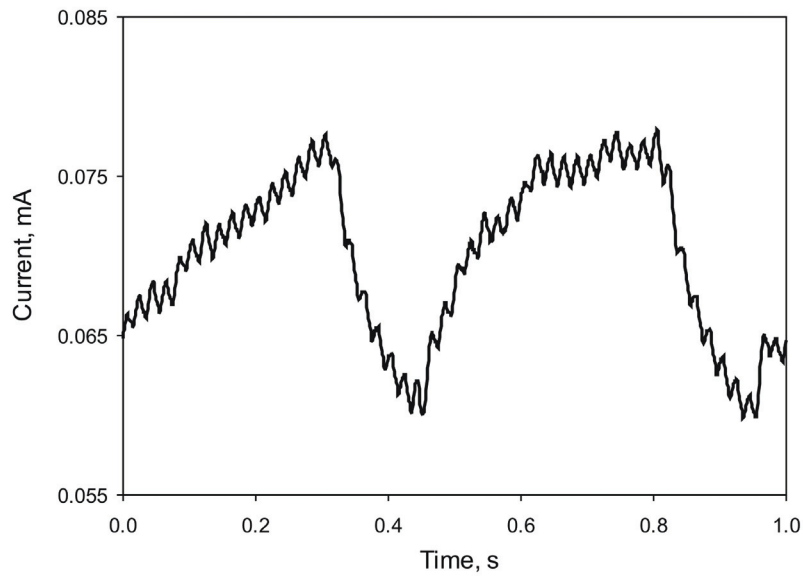


Figure 4.8 Passivation transient of tungsten for the imposed potential of 0.2 V in the 0.01 M H_2SO_4 (cathodically pre-treated sample).

Within the limited number of experiments, the values of measured wear track volume V_{wt} are more reproducible with cathodic cleaning (Table 4.1), thus we have chosen to perform cathodic cleaning pre-treatment before tribocorrosion tests. The noise amplitude (50 Hz) in the current signal is due to the measurement system.

Table 4.1

Effect of the cathodic cleaning on the coefficient of friction, current enhancement due to rubbing and wear track volume (test conditions: imposed potential 0.2 V, normal load 6 N, frequency 1 Hz, duration of rubbing 3000 s).

	COF	I_c , mA	V_{wt} , mm ³
No cathodic cleaning	0.26	0.039	0.00220
	0.27	0.034	0.00161
Cathodic cleaning	0.25	0.036	0.00161
	0.27	0.041	0.00161

4.3. Duration of Rubbing

Tribocorrosion tests were performed for different rubbing periods (60 s, 600 s, 1500 s and 3000 s). Except of the variation in rubbing period, all other tests parameters remained as in the tribocorrosion test procedure including cathodic cleaning pre-treatment from Chapter 4.2.

The evolution of coefficient of friction and current during rubbing with time are given in Figure 4.9 and Figure 4.10. The scattering of current before rubbing started (Figure 4.10) can be observed, as well as the curve's shape scattering during rubbing.

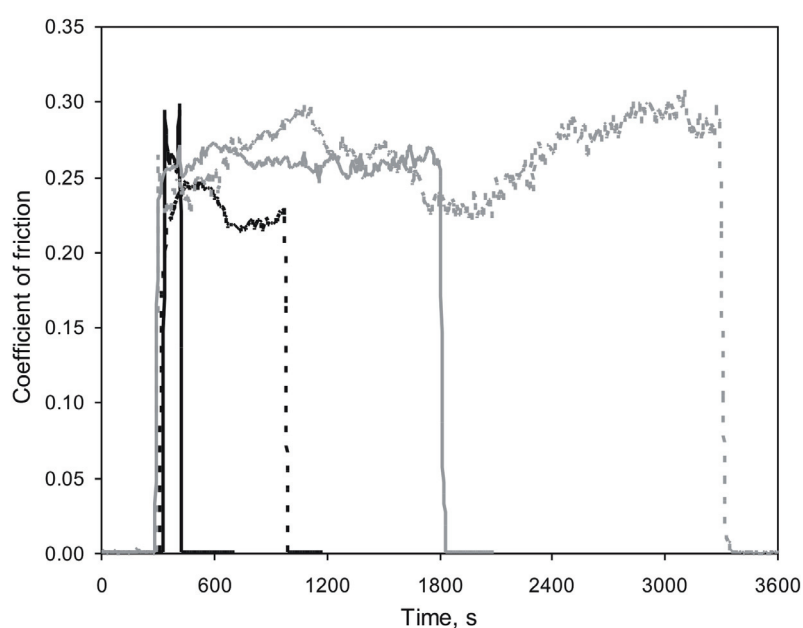


Figure 4.9 Evolution of coefficient of friction with time for different periods of rubbing (60 s, 600 s, 1500 s and 3000 s) at the imposed electrode potential of 0.2 V in the 0.01 M H_2SO_4 .

Coefficient of friction and current enhancement due to rubbing are listed in Table 4.2. The values of COF are reproducible for each period of rubbing and do not change significantly when increasing duration of rubbing. Both current enhancement and total wear volume (Table 4.2 and Figure 4.11) increase when increasing duration of rubbing. The linear trend of V_{wr} increase with duration of rubbing is in agreement with Archard's law (Equation 2.15). The current increase is due to augmentation of the lateral contact with time. The wear volumes corresponding to 3000 s of rubbing are the largest and they enable

to minimize the errors in wear volume measurements. Therefore, the rubbing duration of 3000 s was chosen for the tribocorrosion tests.

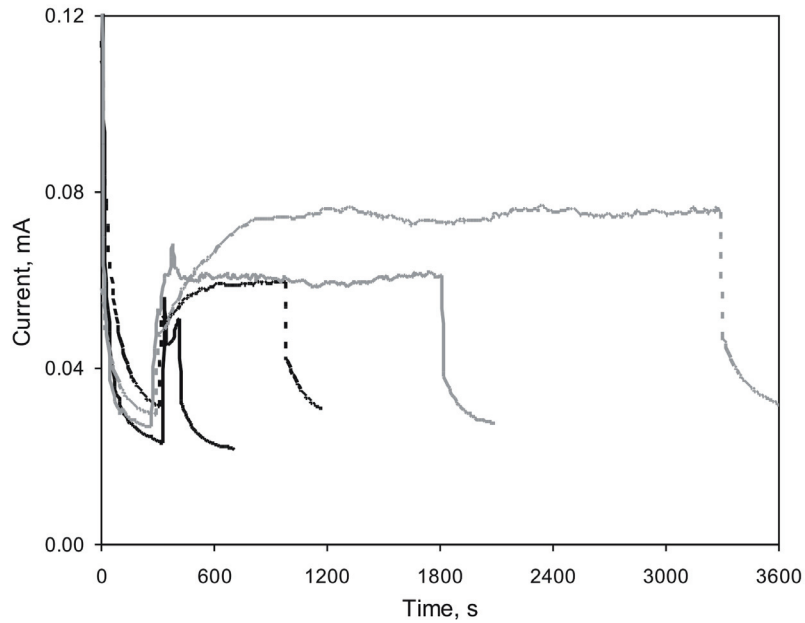


Figure 4.10 Evolution of current during rubbing with time for different periods of rubbing (60 s, 600 s, 1500 s and 3000 s) at the imposed electrode potential of 0.2 V in the 0.01 M H_2SO_4 .

Table 4.2

Effect of the rubbing duration on the coefficient of friction, current enhancement due to rubbing and wear track volume (test conditions: imposed potential 0.2 V, normal load 6 N, frequency 1 Hz).

Duration of rubbing, s	COF	I_r , mA	V_{wt} , mm ³
60	0.27	0.023	0.00004
	0.26	0.017	0.00006
600	0.24	0.029	0.00038
	0.23	0.026	0.00030
1500	0.26	0.032	0.00088
	0.25	0.031	0.00082
3000	0.25	0.036	0.00161
	0.27	0.041	0.00161

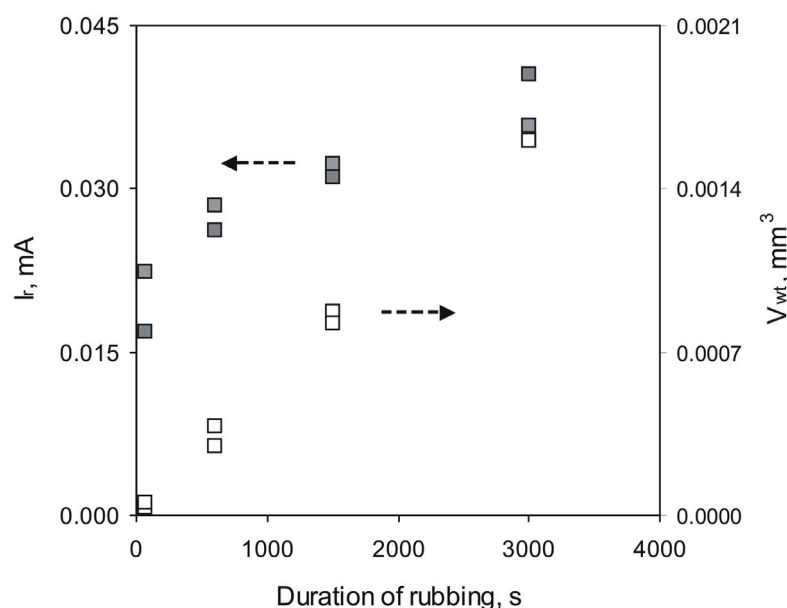


Figure 4.11 Influence of the rubbing duration on the current enhancement due to rubbing and wear track volume (tests conditions: imposed potential 0.2 V, normal load 6 N, frequency 1 Hz).

4.4. Duration of Passivation

Duration of passivation before starting rubbing can influence the value of measured current. In order to evaluate the effect of passivation time we have performed tribocorrosion tests with the passivation periods of 300 s and 7200 s. Imposed potential was 0.2 V, normal load 6 N and frequency of rubbing 1 Hz. Cathodic cleaning was undertaken before testing.

Average currents measured just before rubbing started after 300 s or 7200 s of passivation, reach the values of 0.030 ± 0.001 mA and 0.025 ± 0.000 mA, respectively (Figure 4.12). Current enhancement due to rubbing and wear track volume do not change significantly for different passivation periods, as shown in Table 4.3. Their reproducibility is relatively good, except for the wear track volume corresponding to passivation period of 7200 s. We have chosen the passivation period of 300 s as a standard parameter for tribocorrosion experiments, because it is shorter and the influence of passivation period on the tribocorrosion tests' output values was not significant.

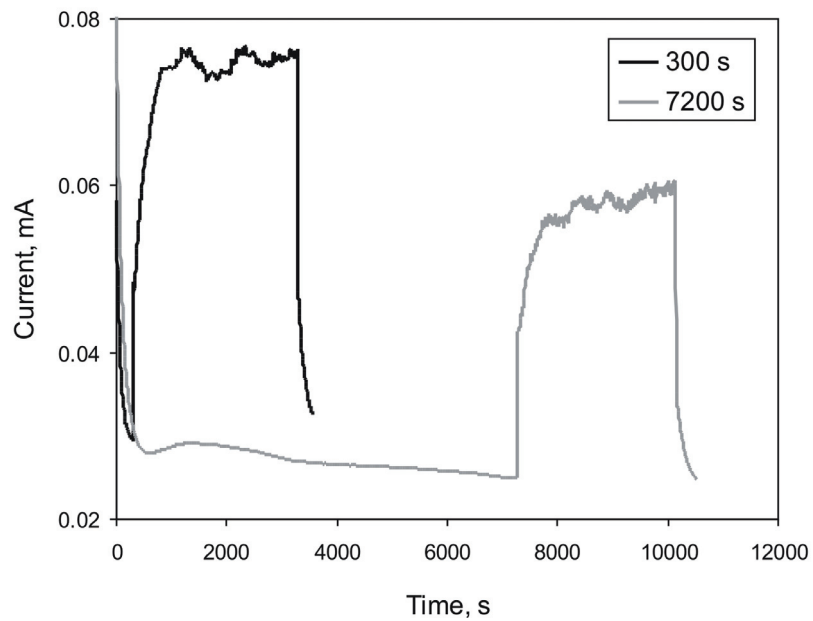


Figure 4.12 Influence of passivation duration on the current before rubbing and current enhancement due to rubbing (tests conditions: imposed potential 0.2 V, normal load 6 N, frequency 1 Hz, duration of rubbing 3000 s).

Table 4.3

Effect of the passivation duration on the coefficient of friction, current enhancement due to rubbing and wear track volume (test conditions: imposed potential 0.2 V, normal load 6 N, frequency 1 Hz, duration of rubbing 3000 s).

Duration of passivation, s	COF	I_r , mA	V_{wt} , mm ³
300	0.25	0.036	0.00161
	0.27	0.041	0.00161
7200	0.27	0.034	0.00164
	0.25	0.033	0.00126

4.5. Frequency of Rubbing

In order to investigate the influence of different rubbing frequencies the rubbing experiments were performed with the frequencies of 0.5 Hz, 1 Hz and 2 Hz, at anodic imposed potential of 0.2 V in the 0.01 M H₂SO₄ solution. The rubbing lasted 3000 s.

Table 4.4

Effect of the rubbing frequency on the coefficient of friction, current enhancement due to rubbing and wear track volume (test conditions: imposed potential 0.2 V, normal load 6 N, duration of rubbing 3000 s).

Rubbing frequency, Hz	Number of cycles	COF	I_r , mA	V_{wt} , mm ³	V_{wt} /number of cycles, mm ³ *10 ⁻⁶
0.5	1500	0.24	0.009	0.00088	0.59
		0.24	0.011	0.00056	0.37
1	3000	0.25	0.036	0.00161	0.54
		0.27	0.041	0.00161	0.54
2	6000	0.30	0.074	0.00333	0.56
		0.30	0.073	0.00348	0.58

The influence of frequency on the wear track volume normalized by number of cycles is given in Table 4.4. These values indicate that no major differences are observed for chosen frequencies. The reproducibility of current enhancement due to rubbing is good for all three frequencies, while the reproducibility of the wear track volume is the best for a frequency of 1 Hz. Thus, 1 Hz was chosen as a standard parameter for tribocorrosion experiments. The I_r augmentation with the frequency follows the tribocorrosion model [1][40], which will be discussed later in Chapter 8.1.

4.6. Normal Load

Three normal loads were chosen for the investigation of their influence, the 1.3 N, 6 N and 15 N. Obtained coefficients of friction, current enhancement due to rubbing and wear track volumes are given in Table 4.5. Significant change of coefficient of friction was not observed. Augmentation of load leads to both current and wear increase (Figure 4.13).

Standard variation of normal load when 15 N are applied increases and influences the scattering of wear volume (Figure 4.13), probably due to higher oscillation observed with the 15 N comparing to 1.3 N and 6 N. According to Archard's law (Equation 2.15), the relationship wear volume vs. normal load should be linear, which is not in agreement with Figure 4.13. This discrepancy could be explained knowing the third body formation is intensified at higher loads.

Table 4.5

Effect of the normal load on the coefficient of friction, current enhancement due to rubbing and wear track volume (test conditions: imposed potential 0.2 V, frequency 1 Hz, duration of rubbing 3000 s).

Normal load, N	COF	I_r , mA	V_{wt} , mm^3
1.3	0.26	0.022	0.00052
	0.23	0.019	0.00050
6	0.25	0.036	0.00161
	0.27	0.041	0.00161
15	0.23	0.053	0.00226
	0.22	0.052	0.00164

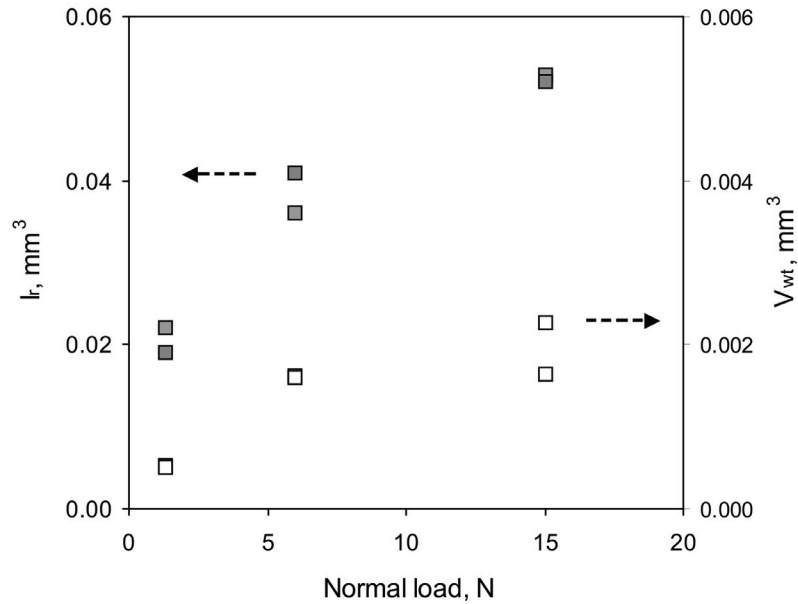


Figure 4.13 Influence of the normal load on the current enhancement due to rubbing and wear track volume (tests conditions: imposed potential 0.2 V, frequency 1 Hz, duration of rubbing 3000 s).

4.7. Standard Test Conditions

The rationale of this Chapter was to evaluate the standard procedure for the tribocorrosion tests. All investigated parameters follow the trend and no discontinuities were found. The standard test parameters, given in Table 4.6, were arbitrarily chosen. Some of the results will be used later in order to elucidate the tribocorrosion phenomena.

Table 4.6

Standard experimental parameters.

Mechanical parameters
Normal load: 6 N
Stroke length: 4 mm
Frequency: 1 Hz
Duration of rubbing: 3000 s

Electrochemical parameters
Electrolyte: 0.01 M H ₂ SO ₄
Cathodic cleaning: 300 s
Passivation time prior to rubbing: 300 s

CHAPTER 5

5. Influence of Electrode Potential on the Tribocorrosion of Tungsten in Sulphuric Acid

The aim of this investigation is to evaluate the effect of electrode potential on the tribocorrosion behavior of tungsten. For this a model tribological system involving an alumina ball sliding against a tungsten plate kept under electrochemical potential control is used. The used solution is the 0.01 M H₂SO₄.

Optical microscopy, UBM and SEM are used as auxiliary techniques to assess surface topography and morphology, and surface analysis techniques XPS and AES to assess surface chemistry.

To assess the effect of the solution stirring induced by the alumina ball's motion, the tests are performed by maintaining the moving ball separated from the tungsten surface (tribocorrosion like tests).

5.1. Experimental Techniques

The tribocorrosion experiments were undertaken using the standard tribocorrosion test procedure, set in Chapter 4. Imposed electrode potentials of -1 V, -0.5 V, -0.2, -0.1 V, 0.2 V, 0.5 V, 1 V and 1.5 V, were selected on the polarization curve (Figure 3.3).

The applied normal load was 6 N for all potentials corresponding to an average Hertzian pressure of 1.19 GPa (calculation given in Appendix C).

Tribocorrosion like tests were performed with the alumina ball maintained 0.4 mm above the tungsten disk surface in order to evaluate the stirring effect of the solution, induced by the moving ball, on the measured current. After cathodic cleaning at -1.7 V during 300 s and stabilization at open circuit potential during 300 s, first imposed potential was -0.2 V. At this potential for the first 300 s alumina ball was maintained motionless, afterwards the ball was set on motion during 600 s without touching the disk surface in order to simulate the fluid dynamics as in a real tribocorrosion test and during the last 300 s at the same potential the ball was again motionless 0.4 mm above the disk. The test was continued using the same tungsten sample by stepwise increasing potential at -0.1 V, 0.2 V, 0.5 V, 1 V and 1.5 V.

Surface characterization: Secondary electron microscopy SEM (JEOL 6300 microscope) was used to characterise wear patterns. The microscope has the following characteristics: 1-30 kV field emission SEM, nominal resolution 2.0 nm at high kV, 7 nm at 1 kV and the maximum sample size 4" x 4". The main application of this microscope is for the high resolution at 20-30 kV and for enhanced topographical contrast. Accelerating voltage was 5 kV and working distance 12 or 13 mm.

5.2. Results

5.2.1. Friction Behavior

Figure 5.1 shows the evolution of the coefficient of friction with rubbing time for different potentials. From the beginning of rubbing the coefficient of friction reaches a steady state value characterized by periodic fluctuations. The average value of the coefficient of friction during rubbing time is listed in Table 5.1 for each individual experiment. No significant effect of the potential on the average coefficient of friction is observed. The values lie typically within the range 0.25-0.3. Only the most anodic potentials (1 V and 1.5 V) yield slightly lower coefficients of friction (0.21-0.25).

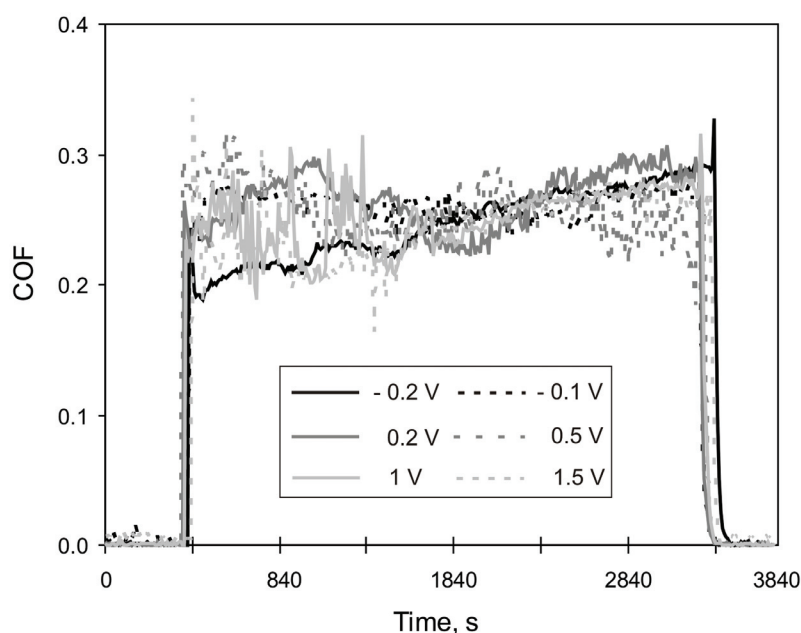


Figure 5.1 Evolution with time of the coefficient of friction (COF) during sliding of a smooth alumina ball against tungsten at imposed different potentials in the 0.01 M H_2SO_4 .

5.2.2. Current in Tribocorrosion Tests

Figure 5.2 shows the changes in current during experiments at different anodic potentials. Values of the current enhancement I_r are listed in Table 5.1. Current recorded during rubbing for potentials up to 0.5 V is stable and increases with imposed potential. For higher potentials current is unstable at the beginning and its value decreases comparing to 0.5 V. In the cathodic region corresponding to the applied potential of -1 V (Figure 5.3), the current before rubbing started and during rubbing has negative values. The reason is that in the cathodic domain metal oxidation reaction does not take place and the cathodic reaction of hydrogen reduction (Equation 2.3) is dominant.

The influence of the ohmic drop phenomena was evaluated and presented in the Appendix A. Low values of the potential drop (Table A-1) indicate negligible influence of ohmic drop phenomena in our tribocorrosion experiments.

Table 5.1

Effect of the imposed electrode potential on the coefficient of friction, current and wear volumes in the standard tribocorrosion test conditions.

E, V	COF	I_r , mA	V_{wt} , mm ³	I_{mt} , mA	I_{wac} , mA	V_{wac} , mm ³
-1.0	0.28	-0.076	0.00022		-	-
-1.0	0.27	-0.123	0.00019	-	-	-
-0.5	0.24	0.000	0.00006		-	-
-0.5	0.27	0.000	0.00003	-	-	-
-0.2	0.25	0.012	0.00019		0.005	0.00025
-0.2	0.25	0.012	0.00012	0.007	0.005	0.00023
-0.1	0.29	0.016	0.00058		0.008	0.00038
-0.1	0.26	0.018	0.00065	0.008	0.010	0.00049
0.2	0.25	0.036	0.00161		0.028	0.00136
0.2	0.27	0.041	0.00161	0.008	0.032	0.00159
0.5	0.26	0.060	0.00313		0.052	0.00256
0.5	0.30	0.077	0.00396	0.008	0.069	0.00340
1.0	0.21	0.012	0.00040		0.004	0.00022
1.0	0.21	0.031	0.00169	0.008	0.023	0.00116
1.5	0.23	0.017	0.00050		0.004	0.00020
1.5	0.25	0.014	0.00045	0.013	0.001	0.00005

Measured values of COF and I_r and calculated values for I_{wac} , V_{wac} and V_{wt} for each tribocorrosion experiment are listed. Average values of two electrochemical experiments for I_{mt} are listed.

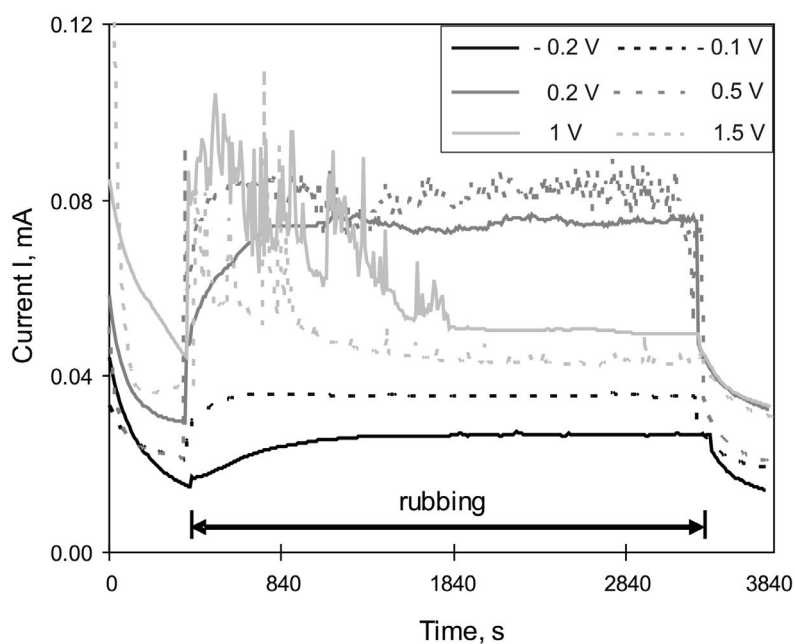


Figure 5.2 Evolution with time of the current during sliding of a smooth alumina ball against tungsten at imposed different potentials in the $0.01\text{ M H}_2\text{SO}_4$. Time zero corresponds to the application of the passive potential. Sliding approximately started at 300 s and stopped at 3300 s .

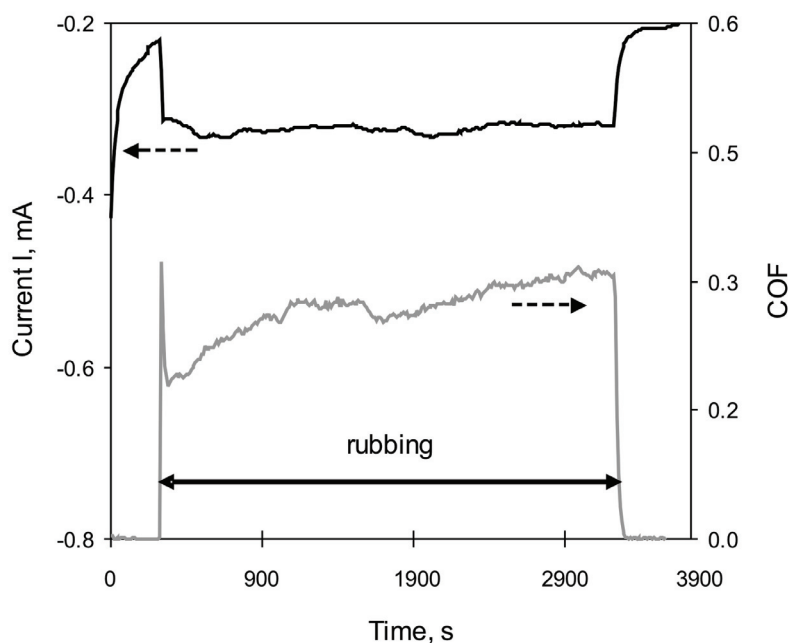


Figure 5.3 Evolution with time of the COF and cathodic current during sliding of a smooth alumina ball against tungsten at imposed potential of -1 V in the $0.01\text{ M H}_2\text{SO}_4$.

5.2.3. Mass Transport Effects in Tribocorrosion Experiments

In tribocorrosion experiments the motion of the ball enhances mass transport [12][22] and thus the dissolution of the tungsten electrode. This fact must be considered in the interpretation of the anodic response during rubbing because two mechanisms may contribute to the enhancement of the current during rubbing. First, the stirring of the solution induced by the ball motion increases the dissolution reaction of the tungsten oxide passive film which kinetics is limited by mass transport. The second mechanism, commonly observed in the tribocorrosion involving passive metal [1], implies the abrasion of the passive film by the alumina ball followed by the repassivation of the bare metal exposed to the solution. This yields an increased corrosion rate of the metal (wear accelerated corrosion).

The current enhancement I_r can be expressed by equation:

$$I_r = I_{wac} + I_{mt} \quad (5.1)$$

where I_{wac} corresponds to the current generated in the wear track by wear accelerated corrosion, while I_{mt} corresponds to the enhanced dissolution of the passive film due to stirring of the solution by the ball. I_{mt} was determined from the test involving the ball moving above the tungsten surface without any contact. Figure 5.4 shows the evolution of current in tribocorrosion like tests with the ball maintained 0.4 mm above the tungsten surface. Table 5.2 shows the values of the current enhancement due to stirring of the solution by the ball, I_{mt} , for different imposed potentials. For each imposed potential average I_{mt} values were calculated by subtracting the average value of current recorded during the period of ten minutes with moving ball by the one half of the sum of the value of current recorded just before the ball was set to motion and the current value recorded 300 s after the motion stopped.

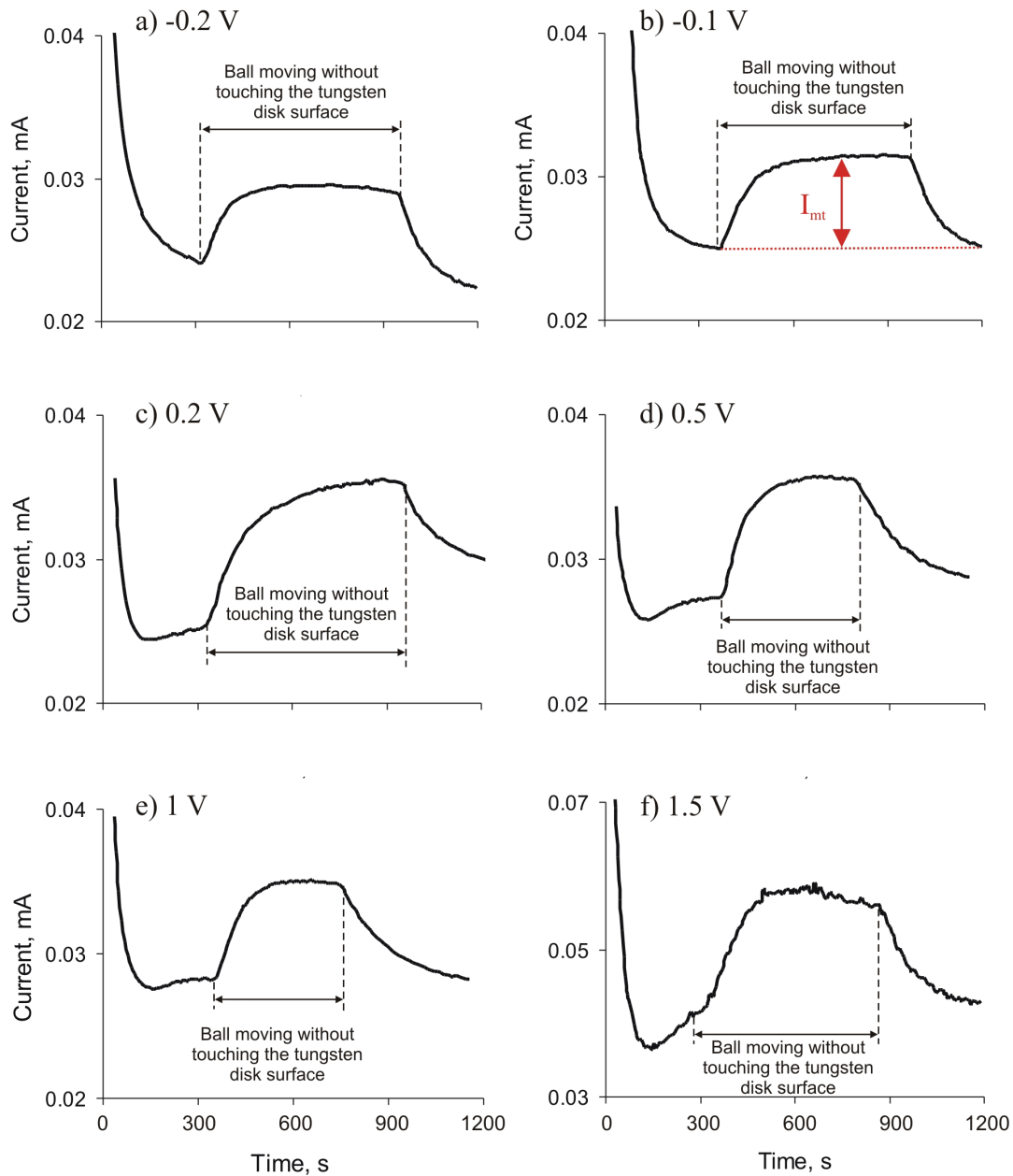


Figure 5.4 Effect of solution stirring by moving ball on the current of tungsten passivated at different potentials: a) -0.2 V, b) -0.1 V, c) 0.2 V, d) 0.5 V, e) 1 V and f) 1.5 V.

Table 5.2

Effect of the imposed electrode potential on the mass transport current, I_{mt} .

E, V	I_{mt} , mA
-0.2	0.006
-0.2	0.008
-0.1	0.006
-0.1	0.009
0.2	0.007
0.2	0.009
0.5	0.007
0.5	0.009
1.0	0.007
1.0	0.009
1.5	0.015
1.5	0.011

Obtained average values of I_{mt} are listed in Table 5.1. The enhancement of the current induced by the motion of the ball, at different imposed potentials, is of the same order of magnitude as the current enhancement measured in tribocorrosion experiments. Thus, enhanced dissolution of the passive film covering the entire tungsten electrode surface must be considered in the interpretation of the electrochemical response under tribocorrosion situations. Wear accelerated corrosion current, I_{wac} , values were obtained by subtracting the I_{mt} values to the measured current I_r :

$$I_{wac} = I_r - I_{mt} \quad (5.2)$$

The metal volume V_{wac} (Table 5.1) removed by anodic oxidation in the wear track was calculated from the measured current using Faraday's law (Chapter 2.4):

$$V_{wac} = \frac{I_{wac} t M}{n F \rho} \quad (5.3)$$

The contribution of I_{mt} to the current enhancement due to rubbing, I_r , in the tribocorrosion tests is given in Figure 5.5.

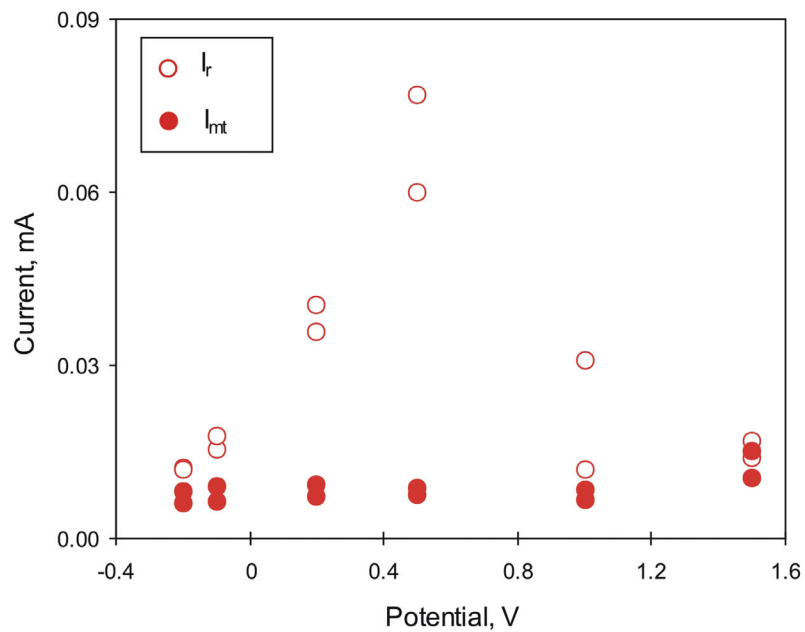


Figure 5.5 Contribution of the mass transport current I_{mt} to the current enhancement due to rubbing I_r in the tribocorrosion tests performed in the 0.01 M H_2SO_4 .

The mass transport current, I_{mt} , slightly changes with imposed electrode potential, but its contribution in the current enhancement, I_r , highly depends on potential, because I_r significantly changes with imposed electrode potential. The wear accelerated corrosion current, I_{wac} , is generated in the wear track, while I_{mt} is generated out of the wear track, due to dissolution of the outer surface film WO_3 of considerable thickness, exposed to solution. The mass transport current can not be generated in the wear track due to the fact that we are continuously activating the metal surface in the wear track. The period of time during which the alumina ball moves from the start to the end point of the wear track during rubbing is 0.375 s. As we have seen from passivation transients at the beginning of tungsten surface oxidation only passivation, i.e. film formation governed by high field conduction occurs and the dissolution appears later. That leads to a conclusion that due to continuous activation of the metal surface and an insufficient thickness of the formed film in between two passages of alumina ball the mass transport controlled dissolution of WO_3 does not have time to appear in the wear track.

5.2.4. Wear Track Characterisation

UBM Laser Profilometry: Tungsten wear tracks' profiles were measured at three different regions of the each track and filtered as explained in Chapter 4.1. Typical wear track profiles for different imposed electrode potentials are given in Figure 5.6. The average values of profiles' depth y and width d for each wear track, together with the wear track surfaces A_{wt} , are given in Table 5.3. The volumes of the wear tracks are listed in Table 5.1. In general higher potential implies higher wear values except at 1 V and 1.5 V where a significant reduction in wear is observed probably because of some protection provided by the layer formation.

Table 5.3

Influence of the electrode potential on the wear track depth (y), width (d) and surface (A_{wt}).

Potential, V	y , μm	d , μm	A_{wt} , mm^2
-1.0	0.195	279	1.1
-1.0	0.167	286	1.1
-0.5	0.075	213	0.9
-0.5	0.064	117	0.5
-0.2	0.227	214	0.9
-0.2	0.146	200	0.8
-0.1	0.593	243	1.0
-0.1	0.722	224	0.9
0.2	1.520	265	1.1
0.2	1.399	288	1.2
0.5	2.860	265	1.1
0.5	3.170	312	1.2
1.0	0.450	221	0.9
1.0	1.870	226	0.9
1.5	0.666	187	0.7
1.5	0.606	185	0.7

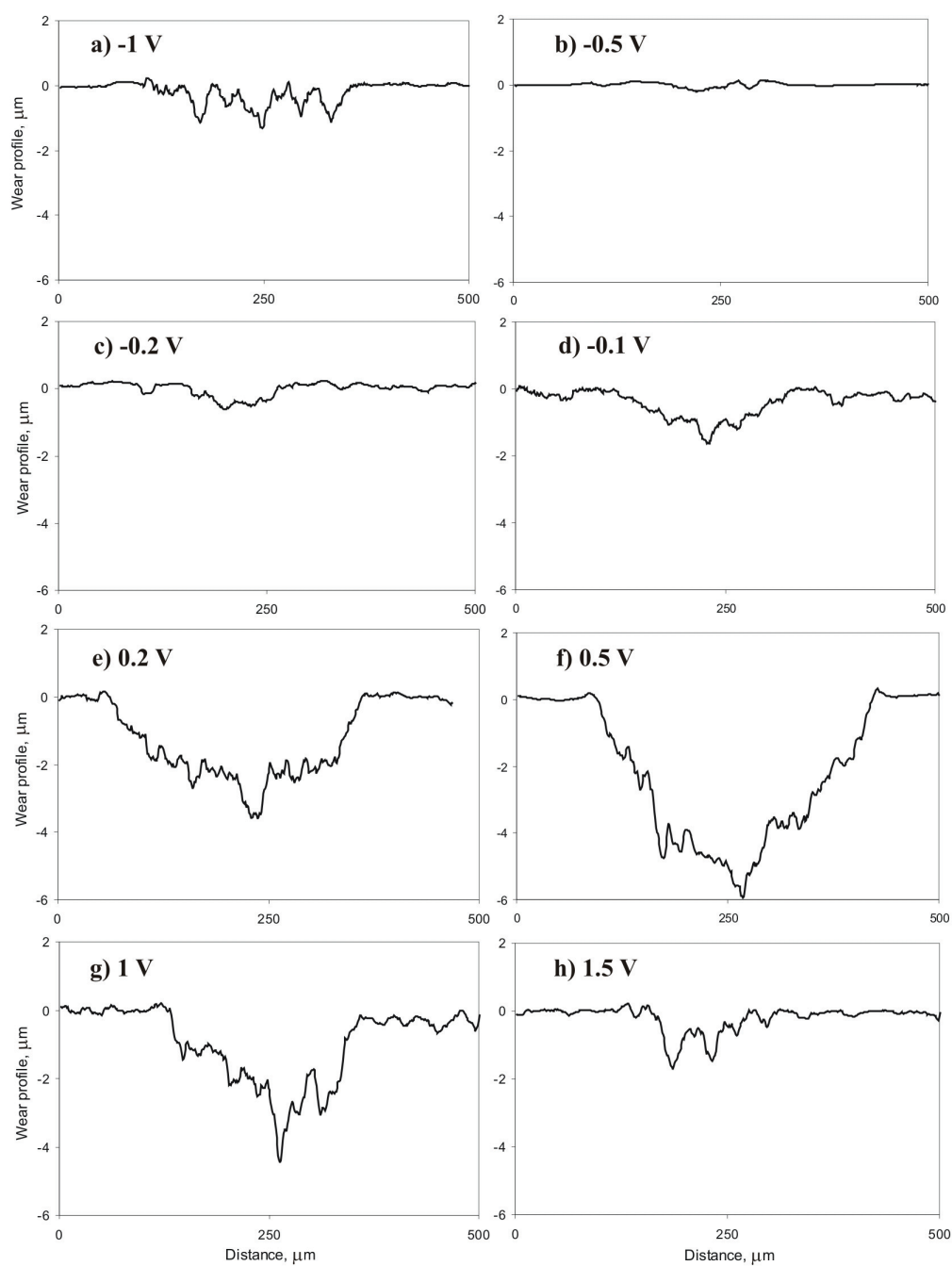


Figure 5.6 UBM wear profiles after rubbing at imposed different electrode potentials: a) -1 V, b) -0.5 V, c) -0.2 V, d) -0.1 V, e) 0.2 V, f) 0.5 V, g) 1 V and h) 1.5 V.

Optical Microscopy Analyses: Information gathered from the images obtained by optical microscopy (Figure 5.7) indicates that wear mechanisms are affected by imposed electrode potential. For the imposed electrode potential of -1 V (Figure 5.7 a), scratches in the direction of sliding and the presence of the debris indicate an abrasive wear mechanism. High roughness in the wear track and low removal rate indicate the presence of a plastic deformation. For the tribocorrosion tests at imposed potential of -0.5 V (Figure 5.7 b) which corresponds to open circuit potential (OCP), the disk surfaces is relatively featureless. Neither intensive scratches nor debris could be observed at the imposed potentials of -0.2 V and -0.1 V (Figure 5.7 c and d respectively). The grain's size and shape can be recognised on the surface both inside and outside the wear tracks. The grain size of $40\ \mu\text{m}$, corresponds to the grain size on the tungsten surface determined by metallographic analysis (Chapter 4.1). For the imposed potentials of 0.2 V and 0.5 V (Figure 5.7 e and f) the wear tracks are more intensive with the presence of debris inside. Wear tracks corresponding to the imposed electrode potentials of 1 V and 1.5 V (Figure 5.7 g and h) are almost completely covered with a tribolayer. The wear of the alumina ball is more visible for the potentials above 0.2 V, as shown in Figure 5.8.

Scanning Electron Microscopy: Figure 5.9 shows typical SEM micrographs taken in the center of the wear tracks formed at different potentials. Surfaces worn at potentials below 0.2 V are rather smooth with some scratches (as shown in Figure 5.9 a and b). At higher potentials some coverage of the wear track surface by a thick, largely cracked layer (tribolayer) can be observed. At 0.2 V and 0.5 V the tribolayer covers only a small fraction of the surface (Figure 5.9 c to f) while at 1 V most of the wear track except the very central zone is covered (Figure 5.9 g and h).

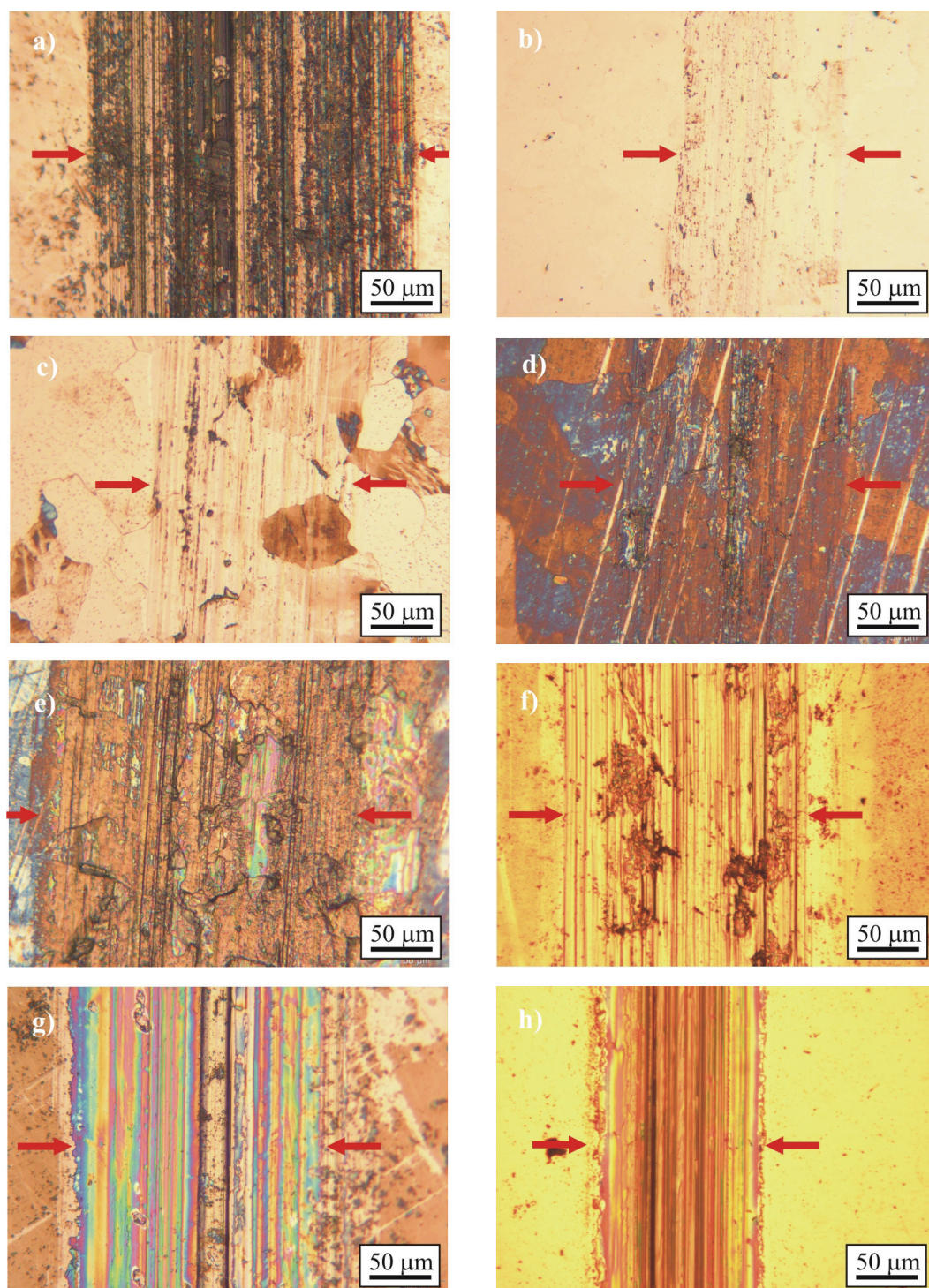


Figure 5.7 Optical micrographs of the wear tracks formed on tungsten after rubbing at imposed different electrode potentials: a) -1 V, b) -0.5 V, c) -0.2 V, d) -0.1 V, e) 0.2 V, f) 0.5 V, g) 1 V and h) 1.5 V.

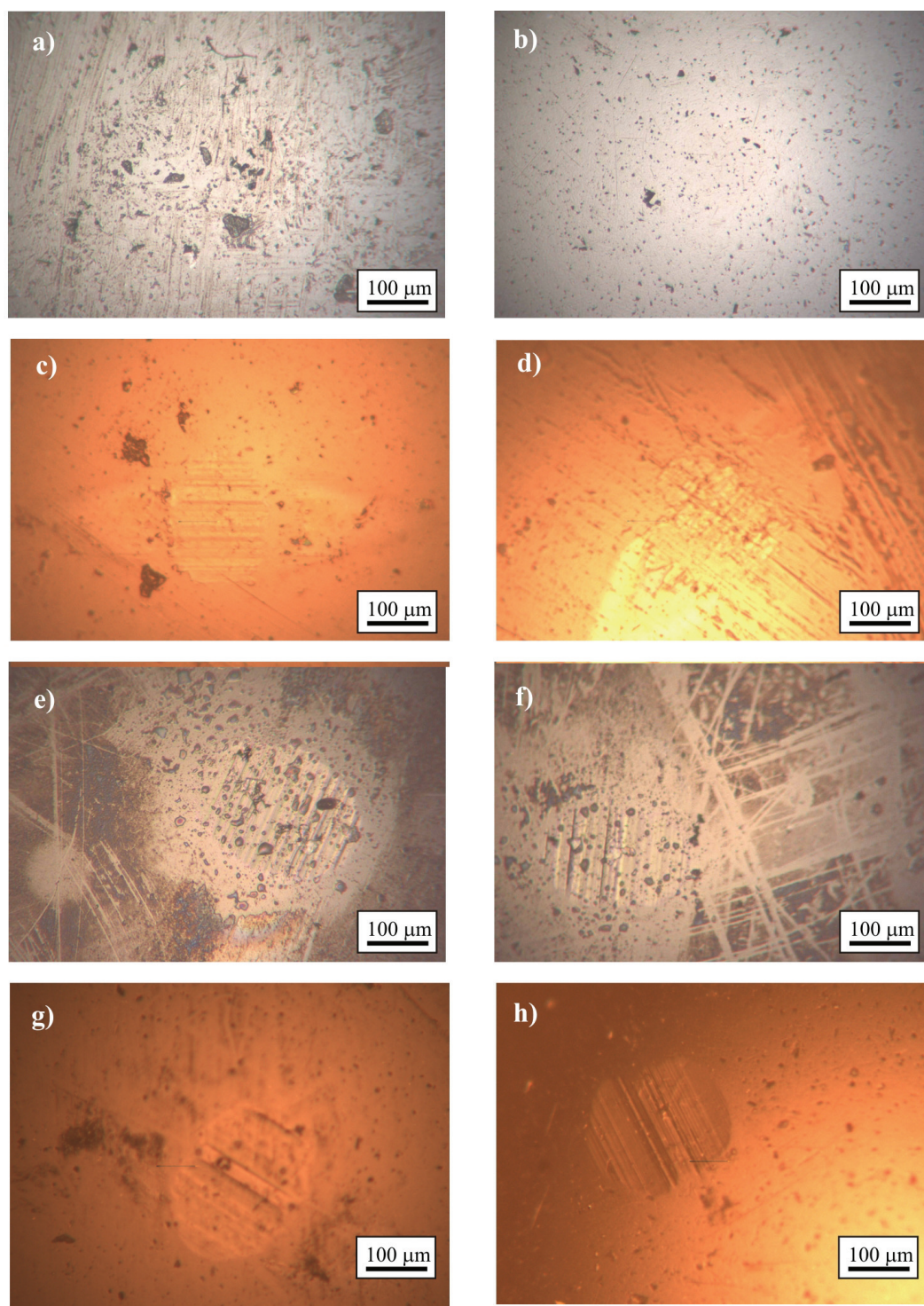


Figure 5.8 Optical micrographs of the alumina balls after rubbing at imposed different electrode potentials: a) -1 V, b) -0.5 V, c) -0.2 V, d) -0.1 V, e) 0.2 V, f) 0.5 V, g) 1 V and h) 1.5 V.

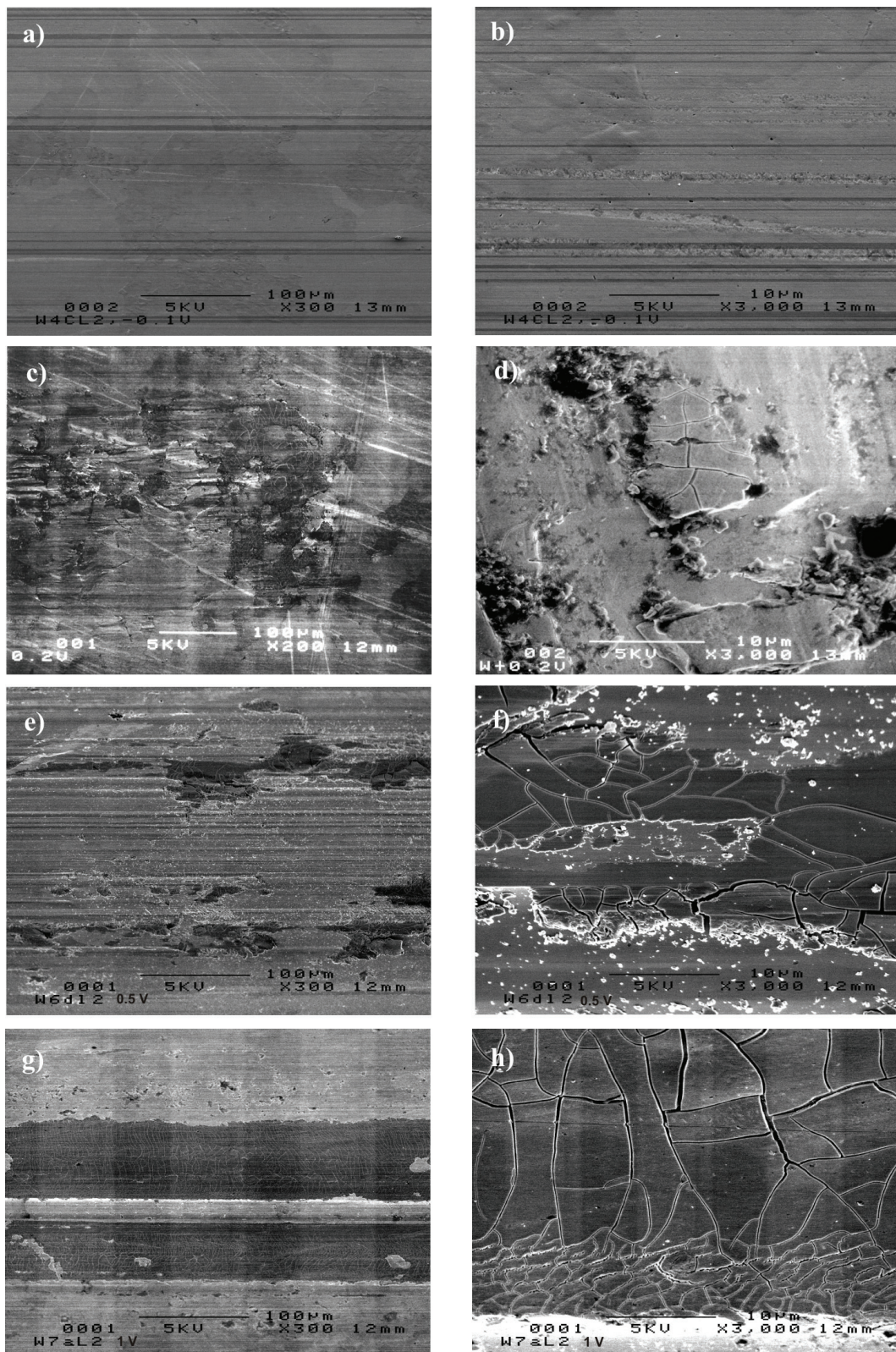


Figure 5.9 SEM images of the wear tracks formed on tungsten after rubbing at imposed potentials of a) and b) -0.1 V, c) and d) 0.2 V, e) and f) 0.5 V and g) and h) 1 V.

AES Analyses: AES depth profiling was performed in the wear track formed at 1 V to identify the nature of the tribolayer. Figure 5.10 shows the depth profiles measured outside and inside the wear track (on a zone covered by the tribolayer).

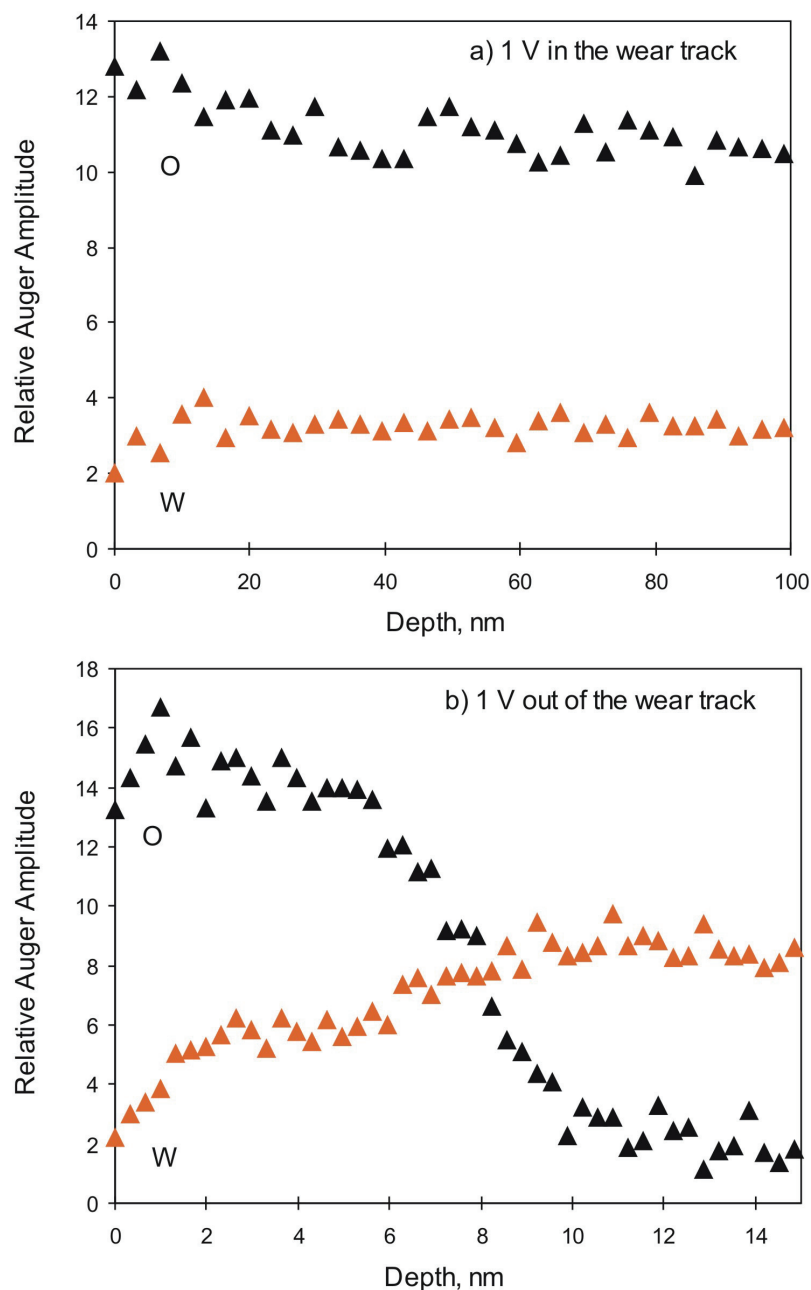


Figure 5.10 AES oxide film thicknesses: a) in and b) out of the wear track for imposed electrode potential of 1 V.

The oxide layer (tribolayer) covering the wear track is much thicker (in excess of 400 nm) than the passive film found outside the wear track. This is also shown in Figure 5.11.

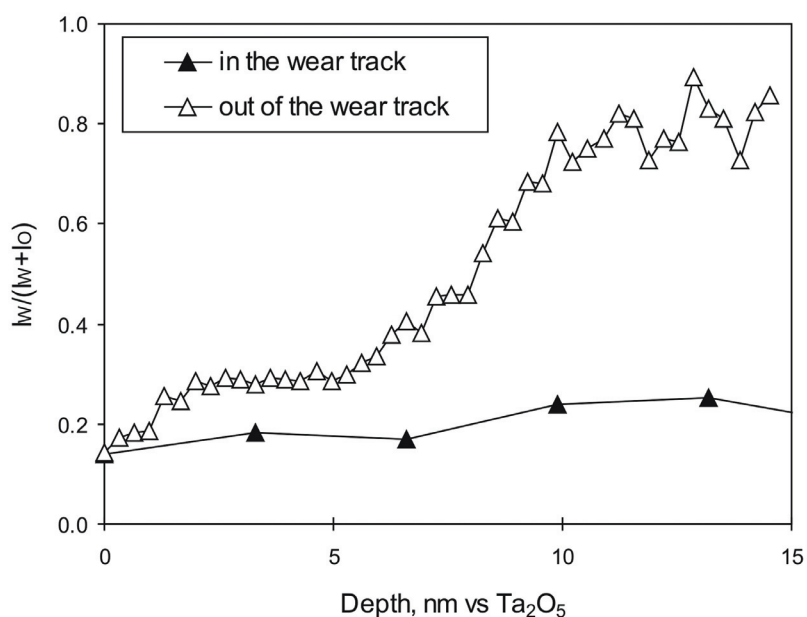


Figure 5.11 AES intensities ratio in and out of the wear track for imposed electrode potential of 1 V in the 0.01 M H_2SO_4 .

Interestingly, as presented in Figure 5.11, the intensity ratio $I_w/(I_w+I_o)$ (where I_w and I_o are the intensities of tungsten and oxygen, respectively) show that both in and out of the wear track from 0 nm up to 2 nm of depth the oxide has the same composition. The oxygen intensity remains high in the wear track. On the contrary, out of the wear track, the oxygen intensity decreases with depth after 2 nm and the ratio $I_w/(I_w+I_o)$ increases approaching the value of 1, which corresponds to the metal state of tungsten. XPS analysis carried out on the layer in the wear track showed that the chemical state of W in the layer corresponds to WO_3 as in the case of passive films.

Micro Hardness Measurements: Tungsten micro hardness was measured inside and outside of the wear tracks using a Leitz Weitzlar 721 300 device. Applied load was 200 g during 15 s. The results from tungsten micro hardness measurements are given in Table 5.4 and in Figure 5.12. Micro hardness measured outside the wear track area does not vary significantly with imposed potential, the hardness lying in the range from 3.8 up to 4.3 GPa. The hardness in the wear track does not differ significantly from the values measured prior to rubbing. Only at potentials of 0.5 V and 1 V a small hardening effect can be observed.

Table 5.4

Surface micro hardness for different imposed potentials, in (H_{wt}) and out (H) of the wear tracks (load 200 g, indentation time 15 s).

Potential, V	H_{wt} , GPa	H , GPa
-1.0	4.4 ± 0.3	4.3 ± 0.1
-0.5	4.3 ± 0.1	3.9 ± 0.1
-0.2	4.2 ± 0.1	4.1 ± 0.1
-0.1	4.4 ± 0.1	4.3 ± 0.1
0.2	4.5 ± 0.3	4.3 ± 0.1
0.5	4.8 ± 0.2	4.3 ± 0.1
1.0	5.1 ± 0.3	4.2 ± 0.1
1.5	4.1 ± 0.1	3.8 ± 0.1

Average values of five measurements for each potential are listed.

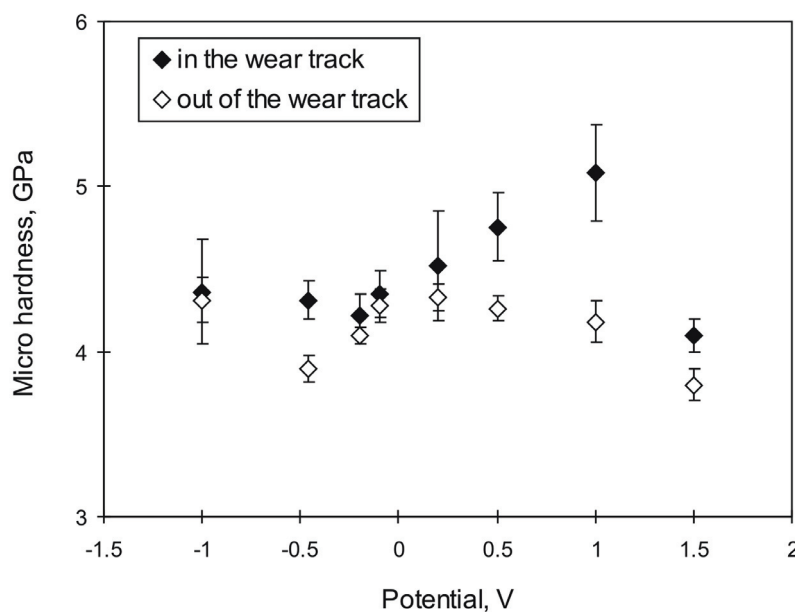


Figure 5.12 Influence of electrode potential on the tungsten surface micro hardness in and out of the wear track.

5.3. Discussion

The obtained V_{wac} values are listed in Table 5.1 and plotted together with the wear track volumes, V_{wt} , as a function of the potential in Figure 5.13. Wear track volumes were

calculated using the Equation (4.2). The obtained values indicate that anodic oxidation accounts for most of the overall material removal from tungsten (V_{wt}) and this for all potentials. Mechanical wear (Equation 2.19) is also present but in a small extent. Only for the electrode potentials of 1 V and 1.5 V, the ratio V_{wt}/V_{vac} increases.

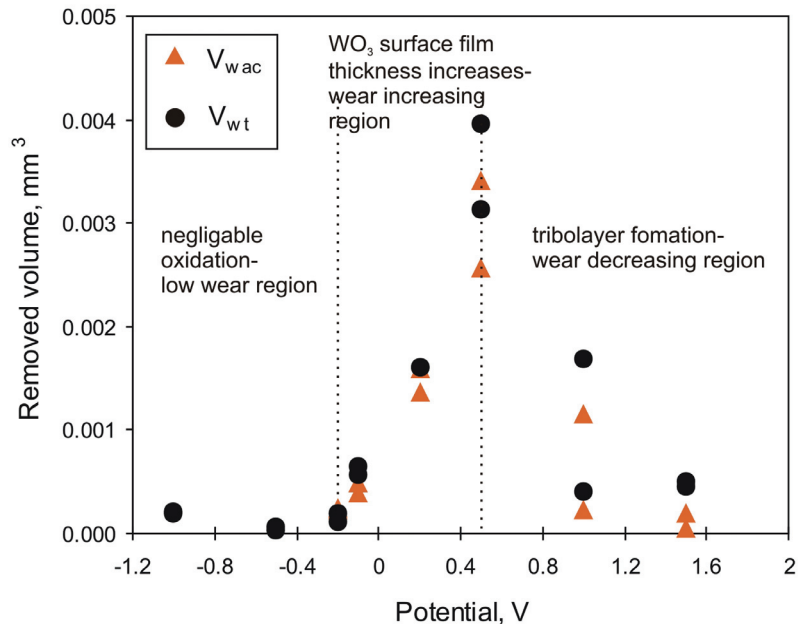


Figure 5.13 Effect of the imposed potential on the volume of removed material.

Three potential domains can be identified in Figure 5.13. Below -0.5 V, a potential corresponding to the open circuit potential, the wear volume remains relatively low and is not significantly affected by the imposed potential. From -0.2 V up to a potential of 0.5 V the wear volume increases with increasing potential. The different dependence of wear with potential found here corresponds well with the observations of Akonko et al [17] (increase of wear for polarization above the open circuit potential).

Below -0.5 V the film thickness is very small and independent on electrode potential (Figure 3.15), while above it the thickness increases rapidly. Since the removal of the oxide film is the determining wear mechanism, rapid increase of wear volume is expected above -0.5 V. At higher potential (1 V, 1.5 V) lower wear values are found. The reason for this transition lies in the formation of the thick WO_3 tribolayer covering the tungsten surface at 1 V and 1.5 V and protecting it against wear. The protective properties of this layer are possibly due to its structure, to its very large thickness or to the strong adherence

to the metal. The growth mechanism of the tribolayer found in the wear track at 1 V and 1.5 V must differ from passive film formation. Indeed, the formation of films thicker than 400 nm would require an anodic potential of approximately 200 V [25], a value much higher than the actual imposed potential. The observed tribolayer could form by agglomeration and compaction of detached WO_3 particles. Indeed, very large anodic currents (and thus wear volume) are observed at the beginning of rubbing at 1 V and 1.5 V (Figure 5.2) indicating the absence of any protective tribolayer. With progressive wear more particles become available to form the layer, which in turn reduces wear and current. The reason why the layer forms only at higher potential is probably complex. Possibly, at higher potentials where passive films are thicker, larger oxide debris particles are spalled off during rubbing. Large particles agglomerate faster than smaller and thus layer formation is facilitated at higher potentials where passive films are thicker (Figure 3.15). Ongoing layer formation is observed at 0.2 V and 0.5 V (Figure 5.9 e to Figure 5.9 f), where passive films are of similar thickness as at 1 V, but not at lower potentials. However, layer formation is not complete at these intermediate potentials thus suggesting that other mechanisms are acting. Tribologically induced formation of thick oxide films was already observed in fretting corrosion experiments involving titanium and was attributed to the continuous mechanical mixing of metal and surface oxides followed by oxidation of the metal exposed to the solution. [41] This mechanism could act in the present situation.

5.4. Conclusions

In this study the effect of electrochemically imposed potential on the tribocorrosion behavior of a tungsten flat disk rubbed by an alumina ball was evaluated in the 0.01 M H₂SO₄ solution.

The obtained results show that the wear of tungsten, under the present experimental conditions, varies with the imposed electrode potential and goes through a maximum for a potential of 0.5 V MSE.

The sliding action of the alumina ball on the tungsten surface causes three wear regions depending on imposed electrode potential.

- Below the first threshold potential (-0.2 V) no removal is observed because the passive film formation is negligible.
- In the second wear region, in between two threshold potentials (from -0.2 V up to 0.5 V MSE) materials deterioration in the rubbed area proceeds by cyclic mechanical removal of the WO₃ passive film followed by repassivation of tungsten. The amount of anodic oxidation corresponds to the overall removed metal volume.
- Beyond the electrode potential of 0.5 V, a thick (more than 400 nm) and compact layer of WO₃, probably formed by agglomeration of oxide particles detached from the metal surface, forms and covers the wear track on tungsten.

The stirring of the solution induced by the motion of the ball and its holder enhances the dissolution of the metal through the passive film in the areas outside the wear track. The current enhancement due to rubbing is corrected for this effect using the procedure developed in this Chapter.

CHAPTER 6

6. Influence of the Chelating Agents on the Tribocorrosion of Tungsten in Sulphuric Acid

Wear volume of tungsten, determined in tribocorrosion tests, was found to depend on the oxidizing power of the solution, simulated by imposing electrode potential by potentiostat (Figure 5.13) and on the passivation kinetics, as investigated in the study presented in Chapter 5. But, for the solutions composed of different chemical compounds (oxidizing agents and additives) with the same value of the open circuit potential, during polishing on CMP machine different removal rates were achieved. This clearly indicates that except potential and passivation kinetics, chemical composition of the solution also affects the tribocorrosion of tungsten.

When increasing imposed electrode potential, thickness of the passive WO_3 on the tungsten surface increases. Chemicals in the solution composition such as chelating agents lactic acid ($C_3H_6O_3$) and phosphoric acid (H_3PO_4), affect film dissolution rates (as shown in Chapter 3) which besides imposed electrode potential (oxidizing power of the solution) determine the total rate of film growth and final film thickness.

The effect of $C_3H_6O_3$ and H_3PO_4 on the tribocorrosion behavior of tungsten is investigated using the experimental techniques from Chapter 5.

6.1. Experiments

Tribocorrosion tests in the solutions presented in Table 6.1 were performed using the standard test conditions (Chapter 4). Applied normal load during rubbing was 6 N. The rubbing lasted 3000 s at the frequency of 1 Hz.

The influence of mass transport on the current enhancement due to solution stirring (see Chapter 5.2.3) was evaluated using the tribocorrosion like tests (explained in Chapter 5.2.3) for all solutions given in Table 6.1. The same surface analysis techniques as in Chapter 5 were used here.

Table 6.1

Solutions and the imposed electrode potentials for the tribocorrosion tests.

Solution	0.2 V	1 V
0.01 M H ₂ SO ₄ +...		
0.1 M C ₃ H ₆ O ₃	x	x
0.25 M C ₃ H ₆ O ₃	x	
0.1 M H ₃ PO ₄	x	x
0.25 M H ₃ PO ₄	x	

6.2. Results

6.2.1. Influence of the Chelating Agents on the Friction Behavior and Current During Rubbing

The coefficient of friction results gathered from tribocorrosion tests are presented in Figure 6.1. The results of two separated experiments are given. As seen in Figure 6.1 a and b, in a presence of 0.1 M C₃H₆O₃, COF during rubbing is unstable and less reproducible for both imposed electrode potentials 0.2 V and 1 V, comparing to rubbing in the presence of 0.25 M C₃H₆O₃ (Figure 6.1 c). During rubbing in the presence of 0.1 M H₃PO₄ at the potential of 1 V (Figure 6.1 e) the COF is more unstable than during rubbing at 0.2 V (Figure 6.1 d and f).

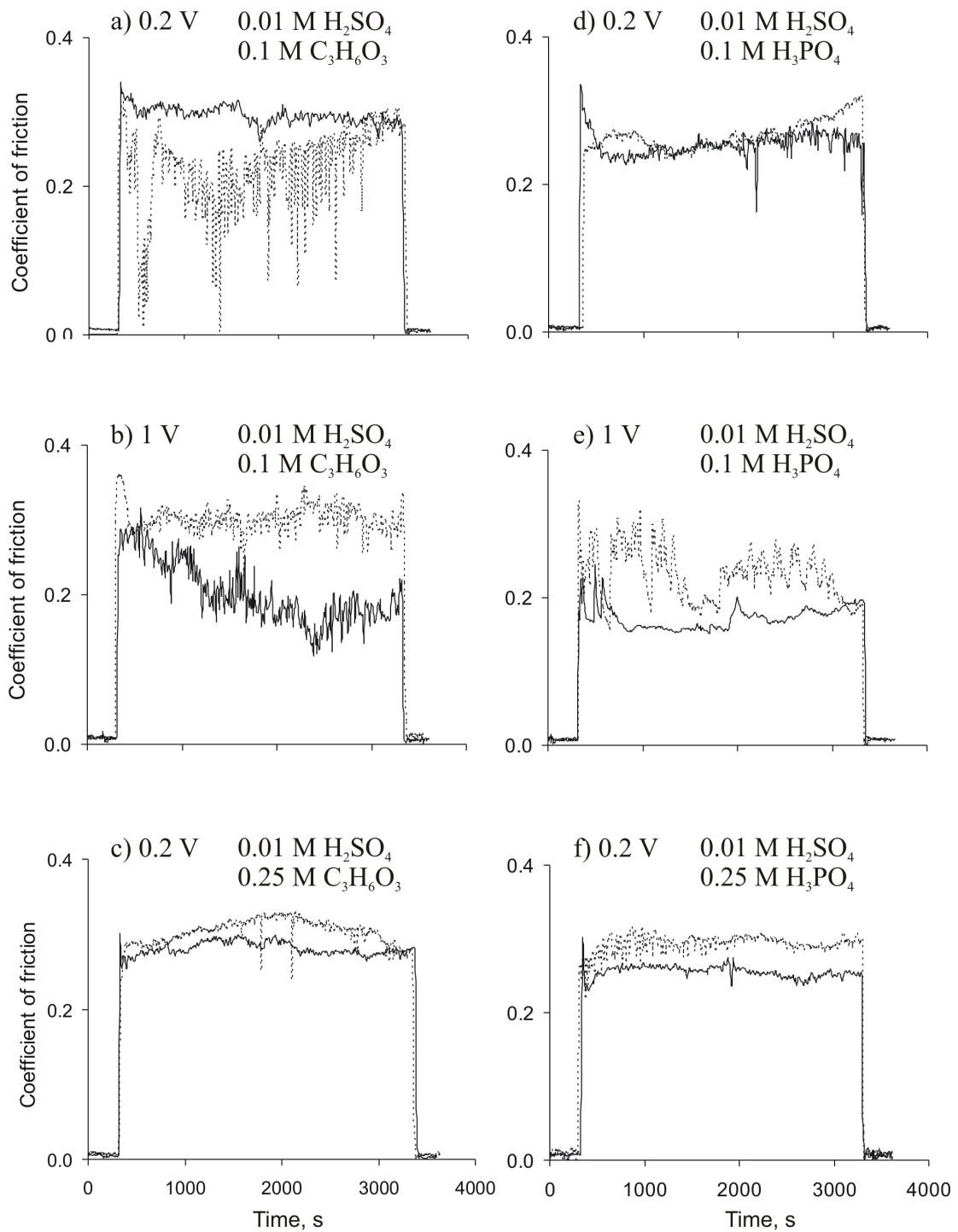


Figure 6.1 Evolution of coefficient of friction with time during sliding of a smooth alumina ball against tungsten in the presence of: a) 0.1 M C₃H₆O₃ at imposed 0.2 V, b) 0.1 M C₃H₆O₃ at imposed 1 V, c) 0.25 M C₃H₆O₃ at imposed 0.2 V, d) 0.1 M H₃PO₄ at imposed 0.2 V, e) 0.1 M H₃PO₄ at imposed 1 V and f) 0.25 M H₃PO₄ at imposed 0.2 V. The results of two independent tests are plotted.

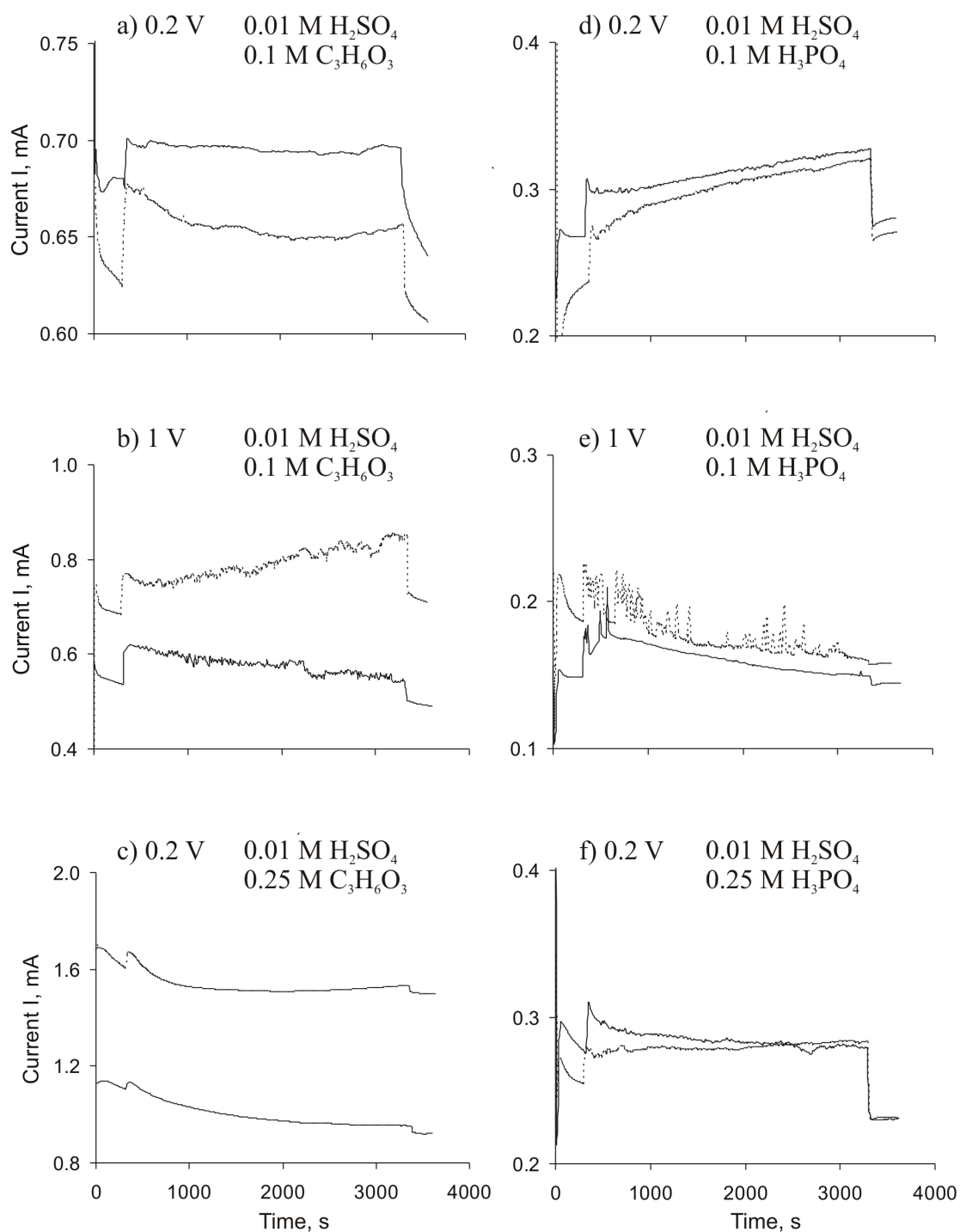


Figure 6.2 Evolution of current with time during rubbing in the presence of: a) 0.1 M $\text{C}_3\text{H}_6\text{O}_3$ at imposed 0.2 V, b) 0.1 M $\text{C}_3\text{H}_6\text{O}_3$ at imposed 1 V, c) 0.25 M $\text{C}_3\text{H}_6\text{O}_3$ at imposed 0.2 V, d) 0.1 M H_3PO_4 at imposed 0.2 V, e) 0.1 M H_3PO_4 at imposed 1 V and f) 0.25 M H_3PO_4 at imposed 0.2 V. The results of two independent tests are plotted.

The current enhancement due to rubbing, I_r , decreases when the concentration of lactic acid changes from 0.1 M to 0.25 M (Figure 6.2 a and c and Table 6.2) at the same electrode potential of 0.2 V. The current enhancement values in the presence of 0.1 M $C_3H_6O_3$ at the potential of 0.2 V are similar to the I_r values in the presence of 0.1 M H_3PO_4 at the same potential (Figure 6.2 a and d and Table 6.2). The current I_r increases in a large extent when the electrode potential is changed from 0.2 V to 1 V in the presence of 0.1 M $C_3H_6O_3$ (Figure 6.2 a and b, Table 6.2 and Table 6.3). On the contrary, in the presence of 0.1 M H_3PO_4 when changing potential from 0.2 V to 1 V, I_r decreases ((Figure 6.2 d and e, Table 6.2 and Table 6.3).

6.2.2. Influence of the Chelating Agents on the Mass Transport Effects in Tribocorrosion Experiments

In order to investigate the effect of potential, a tungsten electrode was polarised stepwise at passive potentials of 0.2 V and 1 V, following the tribocorrosion like tests procedure, explained in Chapter 5.2.3. Figure 6.3 shows the evolution of the current conducted in the tribocorrosion like tests. No change of current when solution stirring started in the tribocorrosion like tests was observed. Therefore, there is no need to correct the current generated during rubbing I_r due to negligible mass transport effects provoked by solution stirring in these solutions. In this case I_{mt} can be considered to have the zero value and I_r is equal to the wear accelerated corrosion current I_{wac} (Equation 5.2). The values of I_{wac} are given in Table 6.2 and Table 6.3, as well as the wear accelerated corrosion values, V_{wac} , calculated using Faraday's law (Chapter 5.2.2).

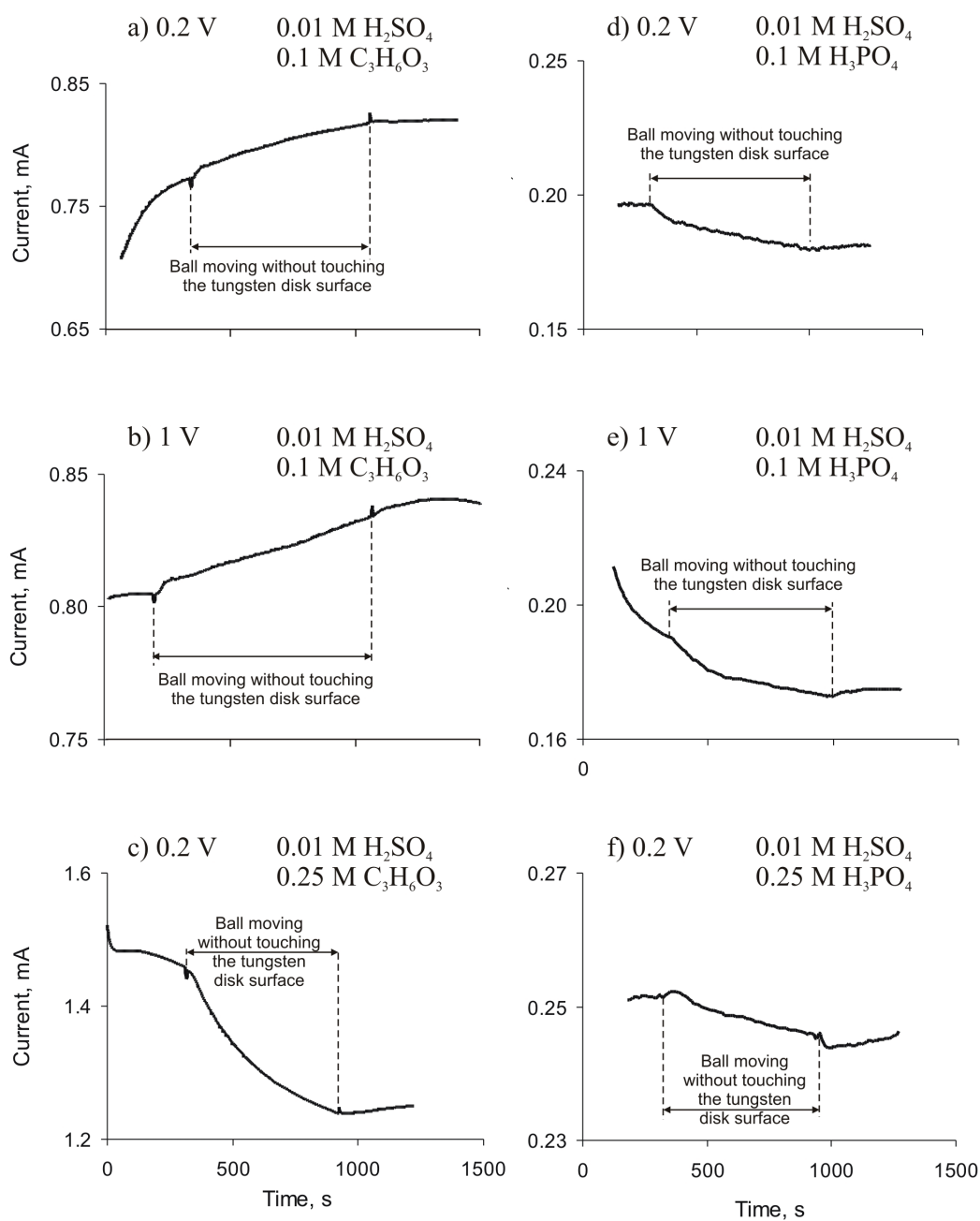


Figure 6.3 Typical evolution of current during tribocorrosion like tests in the presence of: a) 0.1 M $C_3H_6O_3$ at imposed 0.2 V, b) 0.1 M $C_3H_6O_3$ at imposed 1 V, c) 0.25 M $C_3H_6O_3$ at imposed 0.2 V, d) 0.1 M H_3PO_4 at imposed 0.2 V, e) 0.1 M H_3PO_4 at imposed 1 V and f) 0.25 M H_3PO_4 at imposed 0.2 V.

Table 6.2

Effect of the solution composition on the coefficient of friction, current and wear volumes for the imposed electrode potential of 0.2 V in the standard tribocorrosion test conditions.

Solution 0.01 M H ₂ SO ₄ +...	COF	I _{wac} , mA	V _{wt} , mm ³	V _{wac} , mm ³
	0.25	0.036	0.00161	0.00136
	0.27	0.041	0.00161	0.00159
0.1 M C ₃ H ₆ O ₃	0.22	0.040	0.00190	0.00197
0.1 M C ₃ H ₆ O ₃	0.30	0.039	0.00128	0.00193
0.25 M C ₃ H ₆ O ₃	0.28	0.022	0.00155	0.00110
0.25 M C ₃ H ₆ O ₃	0.30	0.016	0.00154	0.00080
0.1 M H ₃ PO ₄	0.25	0.044	0.00260	0.00217
0.1 M H ₃ PO ₄	0.27	0.042	0.00255	0.00207
0.25 M H ₃ PO ₄	0.26	0.038	0.00206	0.00188
0.25 M H ₃ PO ₄	0.29	0.037	0.00277	0.00183

Measured values of COF and calculated values for I_{wac}, V_{wac} and V_{wt} for each tribocorrosion experiment are listed.

Table 6.3

Effect of the solution composition on the coefficient of friction, current and wear volumes for the imposed electrode potential of 1 V in the standard tribocorrosion test conditions.

Solution 0.01 M H ₂ SO ₄ +...	COF	I _{wac} , mA	V _{wt} , mm ³	V _{wac} , mm ³
	0.21	0.012	0.00040	0.00022
	0.21	0.031	0.00169	0.00116
0.1 M C ₃ H ₆ O ₃	0.20	0.066	0.00354	0.00325
0.1 M C ₃ H ₆ O ₃	0.30	0.108	0.00539	0.00533
0.1 M H ₃ PO ₄	0.17	0.020	0.00047	0.00099
0.1 M H ₃ PO ₄	0.23	0.015	0.00073	0.00074

Measured values of COF and calculated values for I_{wac}, V_{wac} and V_{wt} for each tribocorrosion experiment are listed.

6.2.3. Wear Track Characterisation

Optical microscopy images for imposed potential of 0.2 V show almost no wear debris in the tracks obtained in solutions with added lactic acid (Figure 6.4 b and c). Dissolution

of the WO_3 is dominant for tribocorrosion in the solutions containing lactic acid. Traces of debris can be detected in the 0.01 M H_2SO_4 solution (Figure 6.4 a) and in the presence of phosphoric acid (Figure 6.4 d).

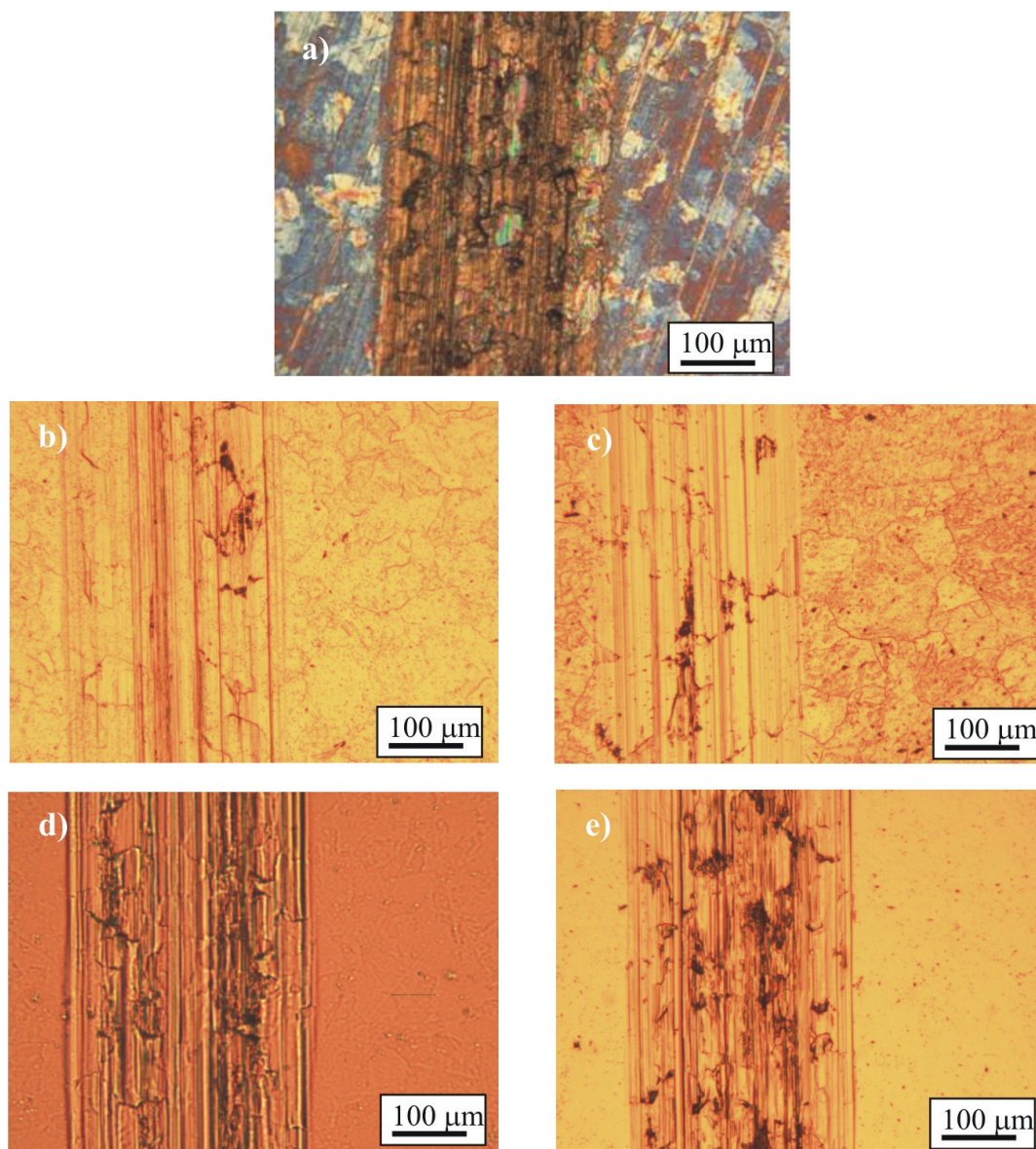


Figure 6.4 Tungsten wear track in different solutions at the imposed electrode potential of 0.2 V: a) 0.01 M H_2SO_4 , b) 0.01 M H_2SO_4 + 0.1 M $\text{C}_3\text{H}_6\text{O}_3$, c) 0.01 M H_2SO_4 + 0.25 M $\text{C}_3\text{H}_6\text{O}_3$, d) 0.01 M H_2SO_4 + 0.1 M H_3PO_4 and e) 0.01 M H_2SO_4 + 0.25 M H_3PO_4 .

Micro hardness in and out of the wear track has similar values for the samples exposed to 0.2 V in the presence of both lactic and phosphoric acid, as presented in Table 6.4. Also, the concentration of lactic and phosphoric acid does not influence the micro hardness

significantly. The micro hardness values of tungsten in and out of the wear track in the 0.01 M H₂SO₄ solution at 0.2 V are higher than those measured in the presence of lactic and phosphoric acid (Table 6.4).

Table 6.4

Effect of the solution composition on the micro hardness in (H_{wt}) and out (H) of the wear tracks at the imposed potentials of 0.2 V and 1 V, in the standard tribocorrosion test conditions.

Solution	H_{wt} , GPa	H , GPa	H_{wt} , GPa	H , GPa
	0.2 V		1 V	
0.01 M H ₂ SO ₄ + ...				
	4.5 ± 0.3	4.3 ± 0.1	5.1 ± 0.3	4.2 ± 0.2
0.1 M C ₃ H ₆ O ₃	3.9 ± 0.2	3.5 ± 0.2	4.5 ± 0.4	3.8 ± 0.2
0.25 M C ₃ H ₆ O ₃	3.5 ± 0.1	3.6 ± 0.2		
0.1 M H ₃ PO ₄	3.8 ± 0.2	3.8 ± 0.2	3.9 ± 0.2	3.8 ± 0.1
0.25 M H ₃ PO ₄	3.7 ± 0.2	3.6 ± 0.2		

Average values of five experiments for each potential are listed.

As previously shown in Chapter 5.2.4, a tribological layer is formed in the wear track after rubbing in the 0.01 M H₂SO₄ solution at higher potentials (Figure 6.5 a and b). This layer, composed of WO₃, is visibly fractured as shown in Figure 6.5 b. Debris is also present out of the wear track. For the samples subjected to the tribocorrosion tests at the imposed potential of 1 V in the presence of 0.1 M C₃H₆O₃, no significant quantities of debris were observed in the wear track (Figure 6.5 c and d). The presence of 0.1 M H₃PO₄ at the potential of 1 V (Figure 6.5 e and f) results in a decrease of a wear track width comparing to the 0.01 M H₂SO₄ solution and to the 0.01 M H₂SO₄ solution in the presence of 0.1 M C₃H₆O₃. Wear track in the presence of 0.1 M H₃PO₄ is partially covered with a tribolayer of the same composition as the tribolayer formed in the 0.01 M H₂SO₄ solution (compacted WO₃ particles). Thickness L_{AES} of this tribolayer is 273 ± 19 nm.

Figure 6.6 shows some abrasion wear at the surface of the alumina balls rubbed at 1 V in 0.01 M H₂SO₄ + 0.1 M C₃H₆O₃ and 0.01 M H₂SO₄ + 0.1 M H₃PO₄.

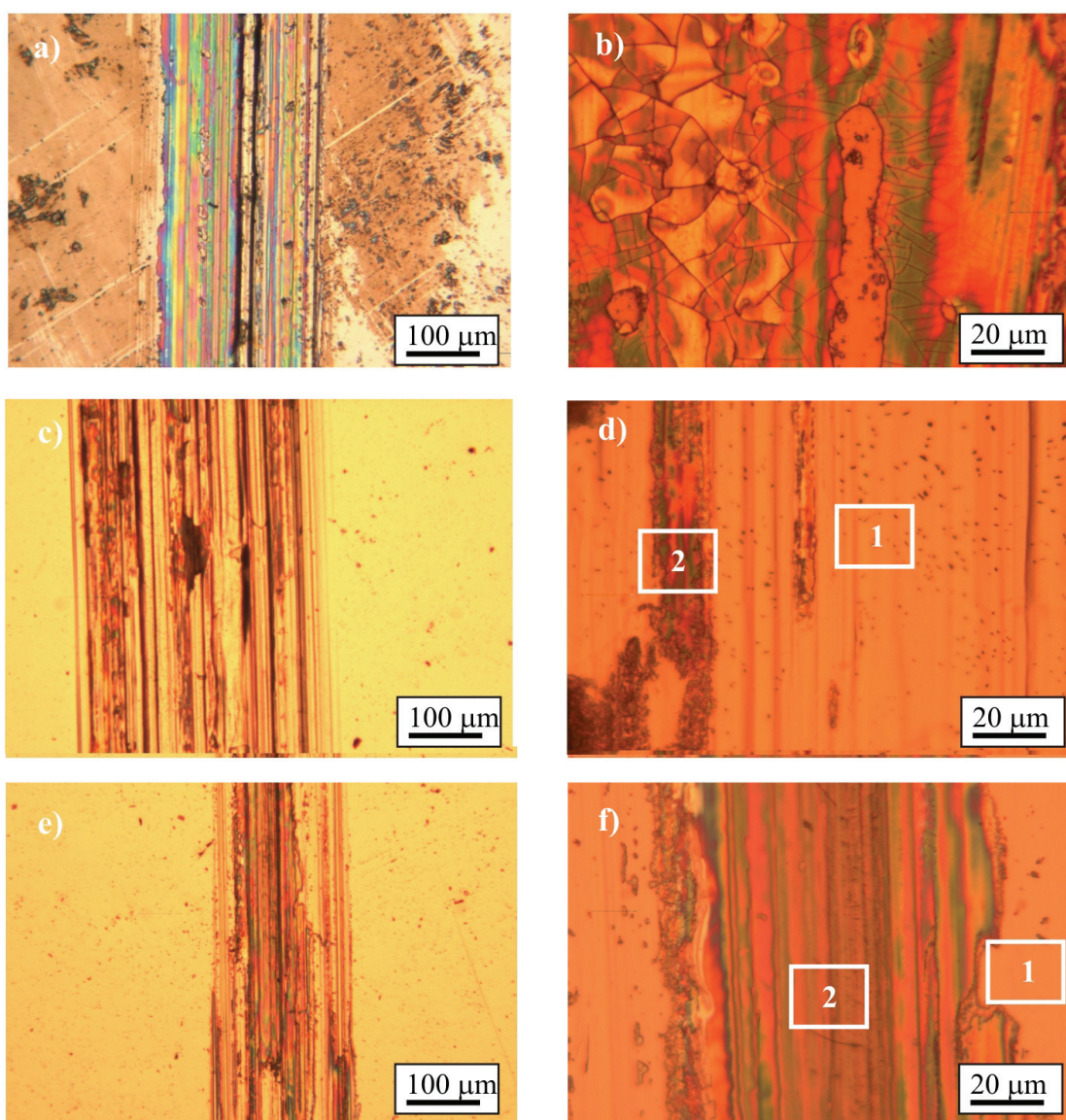


Figure 6.5 Tungsten wear track in different solutions at the imposed electrode potential of 1 V: a) and b) 0.01 M H_2SO_4 , c) and d) 0.01 M H_2SO_4 + 0.1 M $C_3H_6O_3$, e) and f) 0.01 M H_2SO_4 + 0.1 M H_3PO_4 . The areas “1” and “2” correspond to different zones to be analysed.

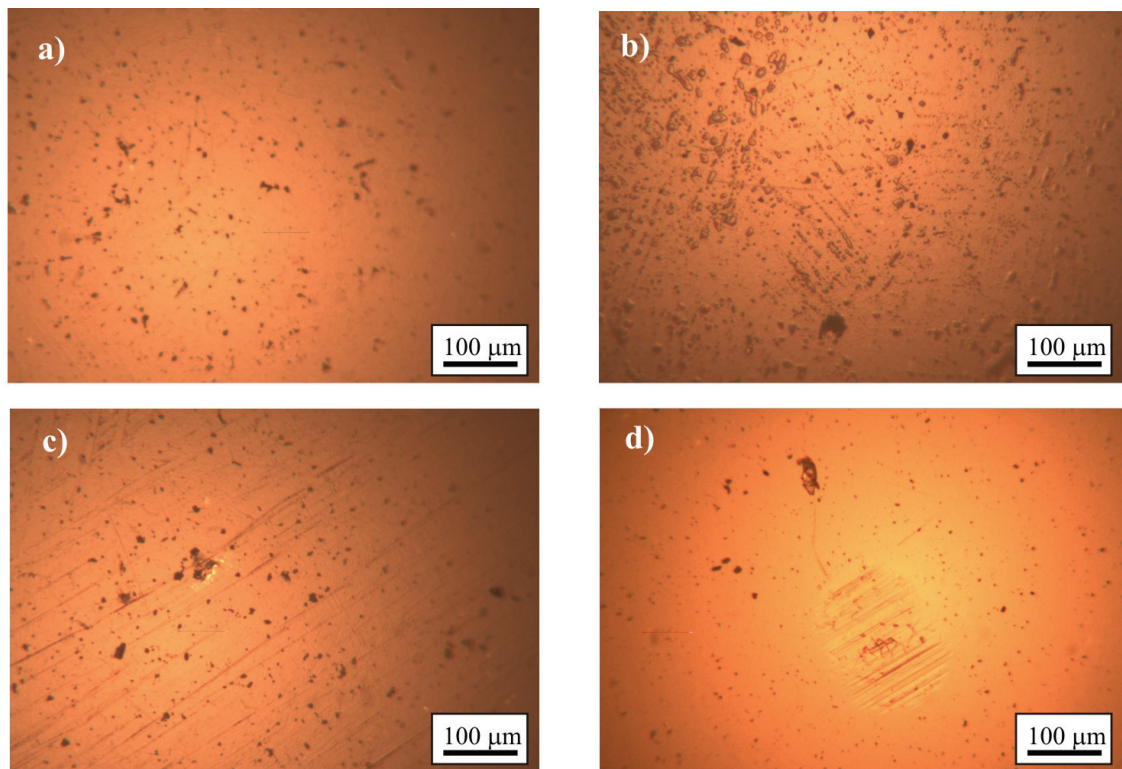


Figure 6.6 Optical micrographs of the alumina balls after rubbing in: a) and b) 0.01 M H_2SO_4 + 0.1 M $C_3H_6O_3$ at 0.2 and 1 V, respectively and c) and d) 0.01 M H_2SO_4 + 0.1 M H_3PO_4 at 0.2 and 1 V, respectively.

Micro hardness in and out of the wear track differs for the samples exposed to 1 V in the 0.01 M H_2SO_4 solution and in the 0.01 M H_2SO_4 solution with lactic and phosphoric acid, as presented in Table 6.4. Hardening in the wear track at the imposed electrode potential of 1 V comparing to 0.2 V is observed in the 0.01 M H_2SO_4 solution (Figure 6.7) due to formation of the tribolayer. Outside the wear track (Figure 6.8) a small hardening effect is observed in the presence of 0.1 M $C_3H_6O_3$ when changing potential from 0.2 V to 1 V. The highest micro hardness is observed in sulphuric acid and the lowest in lactic acid for both potentials. This is in agreement with the thickness of the oxide film formed outside the wear track (Table 3.7). Thicker oxide film implies higher micro hardness out of the wear track.

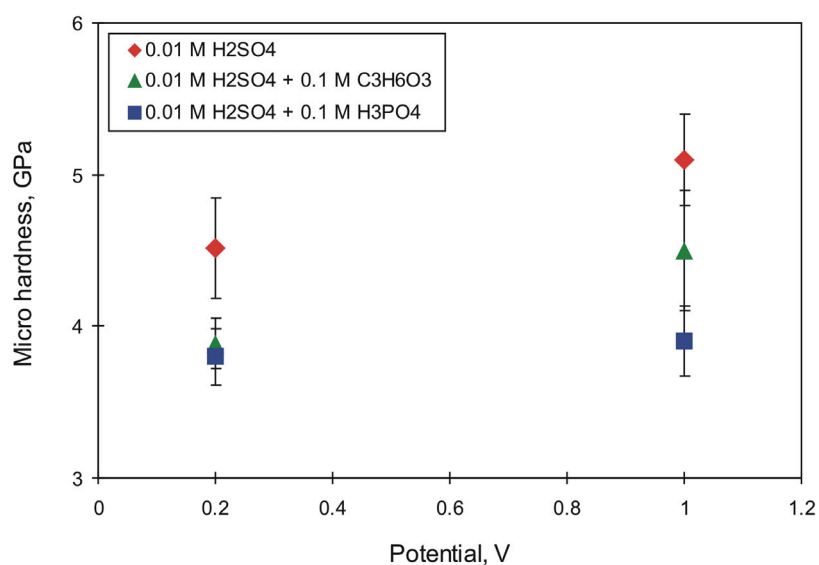


Figure 6.7 Influence of electrode potential and solution composition on tungsten micro hardness in the wear track.

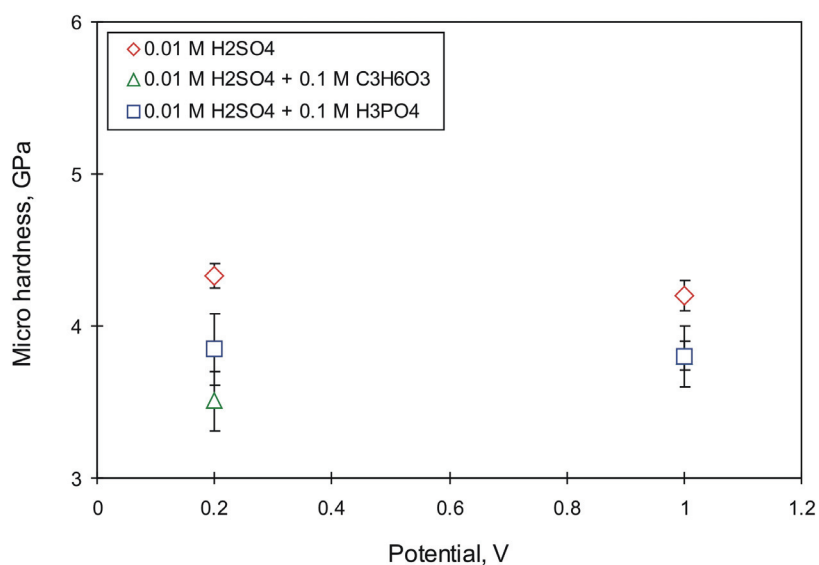


Figure 6.8 Influence of electrode potential and solution composition on tungsten micro hardness outside the wear track.

The values of micro hardness for the area in the wear track marked with a number “1” (Figure 6.5 d and f) which represents the wear track surface not covered with a tribolayer (or compacted particles) are presented in Table 6.5 together with the micro hardness values corresponding to the area “2” covered with tribolayer. Micro hardness of the tribolayer

formed in the presence of 0.1 M H_3PO_4 is lower than that of the tribolayer formed in the 0.01 M H_2SO_4 solution (H_{wt} values for the 0.01 M H_2SO_4 are given in Table 6.4). This is probably due to the decreased thickness of the tribolayer in the presence of 0.1 M H_3PO_4 .

Table 6.5

Effect of the solution composition and wear track morphology on the micro hardness H_{wt} in the wear track, at the imposed potential of 1 V in the standard tribocorrosion test conditions.

Solution	Area 1 H_{wt} , GPa	Area 2 H_{wt} , GPa
0.01 M H_2SO_4 + 0.1 M $\text{C}_3\text{H}_6\text{O}_3$	4.1	5.1
0.01 M H_2SO_4 + 0.1 M H_3PO_4	3.6	3.8

SEM images (Figure 6.9) clearly indicate the difference between the wear tracks obtained in different solutions at imposed potential of 1 V. Wear track obtained in sulphuric acid is covered with tribolayer, while in the presence of 0.1 M $\text{C}_3\text{H}_6\text{O}_3$ wear track is wider and smooth with visible grains of metal. The presence of 0.1 M H_3PO_4 influences the formation of tribolayer similar to one formed in the 0.01 M H_2SO_4 solution (Figure 6.9 a and b) but partially covering the wear track surface.

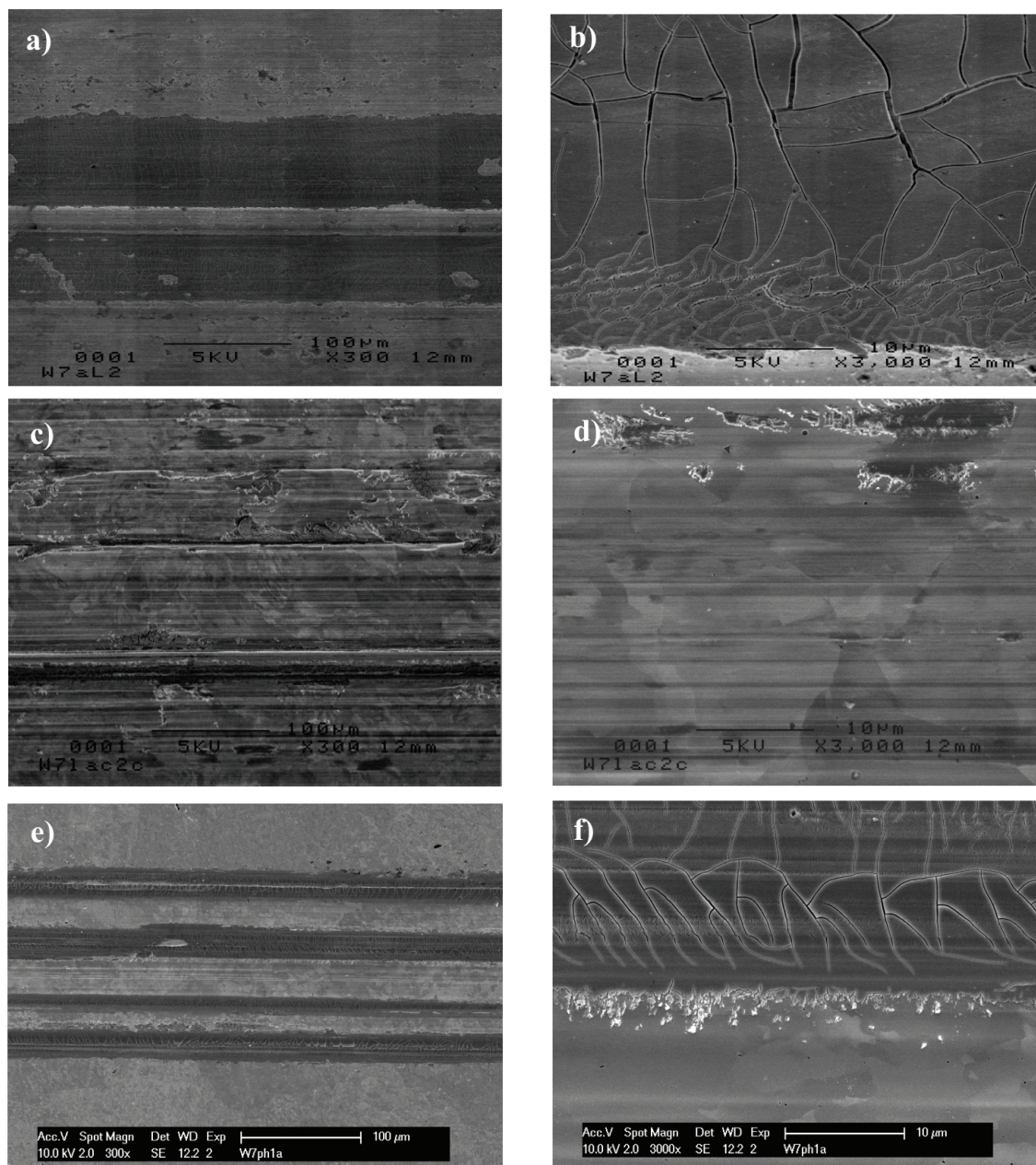


Figure 6.9 SEM images of the tungsten wear tracks obtained at imposed potential of 1 V in different solutions: a) and b) 0.01 M H₂SO₄, c) and d) 0.01 M H₂SO₄ + 0.1 M C₃H₆O₃, e) and f) 0.01 M H₂SO₄ + 0.1 M H₃PO₄.

6.3. Discussion

Measured currents before rubbing and currents during rubbing at imposed electrode potentials of 0.2 V and 1 V (Figure 6.10) are 2-4 times higher in the presence of 0.1 M H₃PO₄ and 10 times higher in the presence of 0.1 M C₃H₆O₃, compared to the 0.01 M

H_2SO_4 solution. The values of current enhancement due to rubbing, I_r , at the imposed potential of 0.2 V are of the same range of magnitude for all solutions. At the imposed electrode potential of 1 V the presence of 0.1 M $\text{C}_3\text{H}_6\text{O}_3$ influences the enhancement of I_r in the large extent.

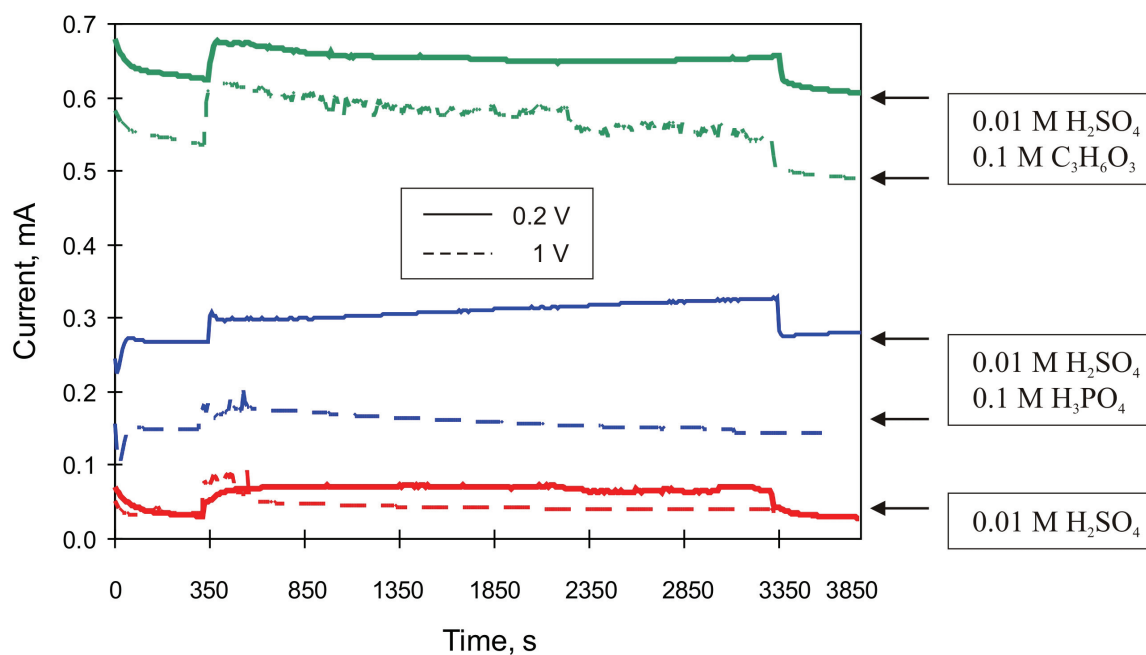


Figure 6.10 Influence of 0.1 M $\text{C}_3\text{H}_6\text{O}_3$ and 0.1 M H_3PO_4 on the measured current during rubbing at imposed electrode potentials of 0.2 V and 1 V.

Wear of tungsten has similar values in the 0.01 M H_2SO_4 solution and in presence of 0.1 M and 0.25 M $\text{C}_3\text{H}_6\text{O}_3$ at the imposed electrode potential of 0.2 V (Figure 6.11). The presence of H_3PO_4 at the imposed potential of 0.2 V increases the wear, compared to the 0.01 M H_2SO_4 solution and solutions containing $\text{C}_3\text{H}_6\text{O}_3$, as presented in Figure 6.11.

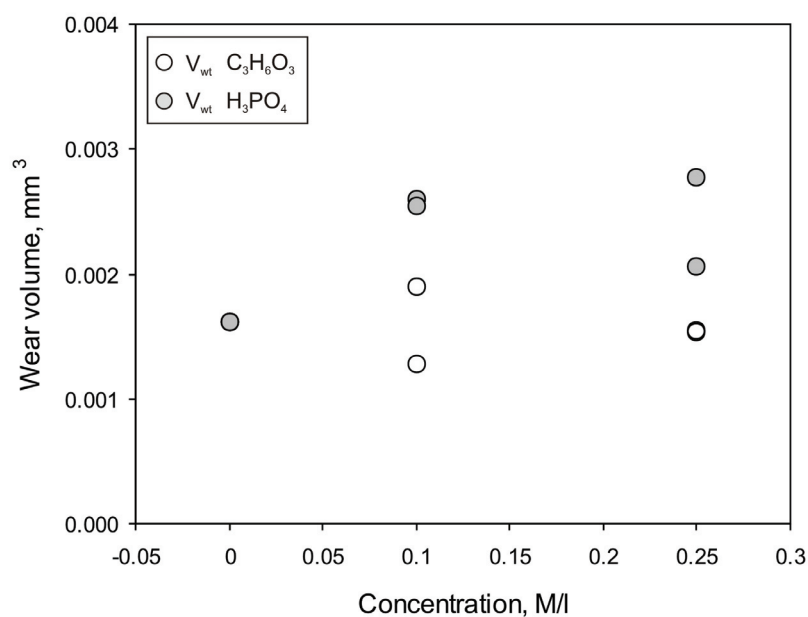


Figure 6.11 Effect of the molar concentration of $\text{C}_3\text{H}_6\text{O}_3$ and H_3PO_4 in the sulphuric acid solution on the wear of tungsten, at the imposed electrode potential of 0.2 V.

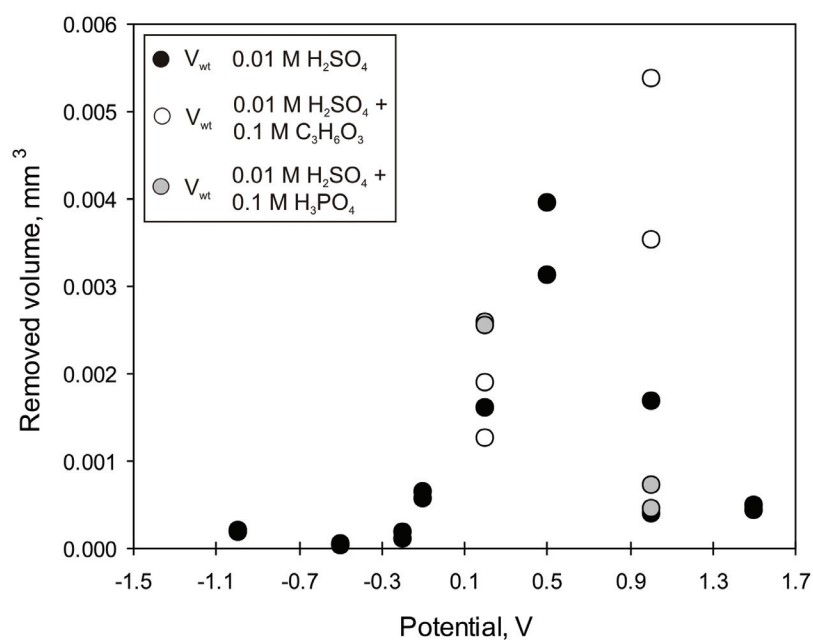


Figure 6.12 Influence of the solution composition and electrode potential on the wear of tungsten.

The ratio V_{wt}/V_{vac} is close to 1 in the presence of 0.1 M lactic and 0.1 M phosphoric acid (Table 6.2 and Table 6.3), implying that the removal proceeds mostly through the

wear accelerated corrosion, while mechanical wear is present in a smaller extent. At the imposed potential of 0.2 V wear is similar in the 0.01 M H₂SO₄ solution and in the presence of 0.1 M C₃H₆O₃ (Figure 6.12). At the imposed potential of 1 V wear increases significantly in the presence of 0.1 M C₃H₆O₃. This is probably due to fast dissolution of WO₃ particles that prevents tribolayer formation. SEM images confirm the absence of a tribolayer on the sample rubbed at potential of 1 V in presence of 0.1 M C₃H₆O₃ (Figure 6.9). On the contrary, the amount of removed material in the solution containing 0.1 M H₃PO₄ (Figure 6.12) decreases when increasing electrode potential from 0.2 V up to 1 V. At imposed potential of 0.2 V wear volumes are slightly higher for the 0.01 M H₂SO₄ solution with 0.1 M H₃PO₄ comparing to the 0.01 M H₂SO₄ solution. At the imposed potential of 1 V wear volumes of tungsten in the 0.01 M H₂SO₄ and in the 0.01 M H₂SO₄ with 0.1 M H₃PO₄ have similar values.

6.4. Conclusions

The values of current enhancement due to rubbing, I_r , are of the same order of magnitude in sulphuric acid solution and in the presence of 0.1 M lactic or phosphoric acids, at the imposed potential of 0.2 V.

The presence of phosphoric or lactic acids in the concentration of 0.1 M does not influence the tungsten wear volume at the imposed potential of 0.2 V.

Wear volume increases significantly in the presence of 0.1 M lactic acid at the imposed potential of 1 V. This is probably due to fast dissolution of WO₃ particles leading to the prevention of the tribolayer formation in the wear track.

In the presence of 0.1 M phosphoric acid at the imposed potential of 1 V the formed tribolayer covers approximately half of the wear track area and reduces wear.

Wear of tungsten does not change significantly when increasing the concentration of lactic or phosphoric acid from 0.1 M to 0.25 M.

CHAPTER 7

7. Tungsten Electrochemical Parameters and Removal Rates in the CMP Practice

Tribocorrosion behavior of tungsten in the 0.01 M H₂SO₄ model solution is found to depend on electrode potential (corresponding to oxidizing power of a solution), on passivation kinetics and on solution composition.

In attempt to identify the relevance of chemical and electrochemical parameters in the CMP practice, the tests on the CMP machine are performed. Open circuit potentials and passivation kinetics of tungsten in the technical CMP slurries are measured in independent laboratory tests.

7.1. Experimental Techniques

7.1.1. Electrochemical Experiments

Open circuit potentials (*OCP*) for tungsten samples were measured using the set up consisted of mercury sulphate reference electrode and Metex multimeter. Open circuit potential values were measured after 60 s, 120 s and 180 s, and the average values were calculated. The used slurries were:

- slurries containing 3 % silica particles and different content of KIO₃ (0 %, 0.1 %, 2 % and 4 %) with pH 5,

- slurries containing 3 % silica particles and different content of KIO_3 (0 %, 0.1 %, 2 % and 4 %) with addition of HCl in order to achieve pH 2,
- slurries containing 3 % silica particles, 5 % H_2O_2 , different content of $\text{Fe}(\text{NO}_3)_3$ (0 %, 0.001 %, 0.02 %, 0.05 %) and HCl in order to adjust the pH. These slurries have pH 2.5, except for 0.02 % $\text{Fe}(\text{NO}_3)_3$, which has pH 3,
- reference slurry (RS) containing 3 % silica particles, 2 % KIO_3 , H_3PO_4 and $\text{C}_3\text{H}_6\text{O}_3$ with a pH 2.75 (adjusted with NH_4OH).

The slurry RS is considered as the reference technical slurry for the Center of Micronanotechnology at the EPFL, concerning removal rate and chemical composition. The size of the silica particles is 12 nm. Slurries composition and pH are given also in Table 7.1 in Chapter 7.2. All the percents of the slurries components are given as weight percents.

Tungsten samples of 5.3 mm diameter were embedded in epoxy resin, polished with grit paper 600, rinsed with alcohol and distilled water and dried with compressed air before carrying out the measurements.

Passivation kinetics was measured using Lab view software for passivation kinetics measurements (explained in Chapter 3.1.1). The potential was switched from cathodic potential of -1 V to passive anodic potential of 0.2 V for all used slurries with repolished tungsten samples. Three independent tests were carried out in the each slurry in order to check the reproducibility.

7.1.2. Polishing on the CMP Machine

Removal rate of tungsten was measured on the CMP machine (type Mecapol E460, manufacturer Alpsitec, Figure 7.1), situated in the Center of Micronanotechnology (CMI) at the Swiss Federal Institute of Technology, EPFL. The principle of polishing on the CMP machine is presented in Figure 2.2. The used samples were CVD tungsten wafers, with a diameter of 101.6 mm (4"). The CMP process includes the following parameters: wafer pressure (pressure on the head), platen speed, head speed, back pressure (pressure on the back of the wafer), slurry flow and polishing time (usually 60 s). These parameters may vary in respect to a material to be polished and used slurry. CMP process parameters for polishing tungsten CVD wafers were:

- Pressure on the head 5 psi,
- Platen speed 50 rpm,
- Head (wafer) speed 60 rpm,
- Back pressure (pressure on the back of the wafer) 0.15 psi,
- Slurry flow 100 ml/min and
- Polishing time 60 s.

Measured CMP removal rates are given in Table 7.1.



Figure 7.1 CMP machine Mecapol E460.

7.2. Results

7.2.1. Open Circuit Potential Measurements for Technical CMP Slurries

Open circuit potentials, measured in slurries prepared with different content of KIO_3 and having different pH, are given in Figure 7.2 and Table 7.1. When the concentration of KIO_3 reaches 1 % the saturation occurs and the *OCP* is stabilizing for both pH. Open circuit potential values are lower for the pH 5 compared to pH 2 values. Open circuit potentials, measured in slurries containing oxidizing agent H_2O_2 and different content of $\text{Fe}(\text{NO}_3)_3$, are given in Figure 7.3 and Table 7.1. When the concentration of $\text{Fe}(\text{NO}_3)_3$ reaches 0.02 % the saturation occurs and the *OCP* is stabilizing.

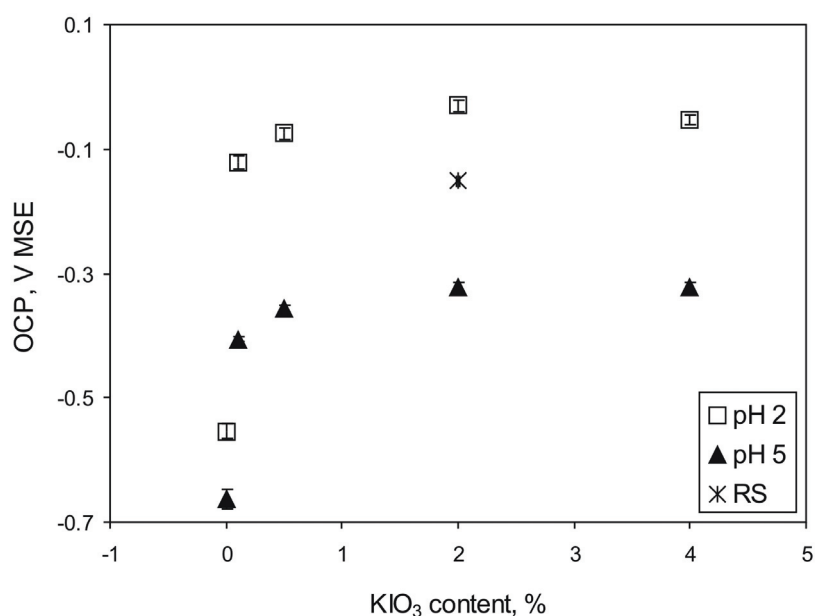


Figure 7.2 Influence of the KIO_3 concentration and slurry pH on the open circuit potential of tungsten.

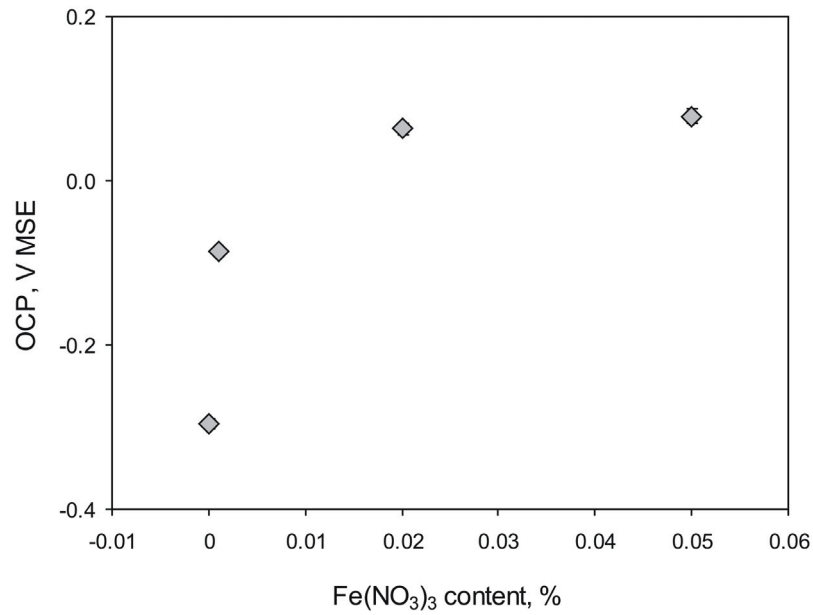


Figure 7.3 Influence of the $Fe(NO_3)_3$ concentration on the open circuit potential of tungsten in H_2O_2 solutions.

7.2.2. Passivation Kinetics for Technical CMP Slurries

The passivation transients in Figure 7.4 a and b are showing the increase of current when increasing the concentration of KIO_3 . From the passivation transients shown in Figure 7.4 c we can not see the clear trend of passive current increase when increasing the concentration of $Fe(NO_3)_3$. Passivation charge densities measured in the technical CMP slurries, Q_{PCMP} are given in Table 7.1. They were calculated by integrating the measured current (Figure 7.4) from the first point acquired after potential change in the potential step experiments from -1 V to 0.2 V, which corresponds to 0.003 s, up to 0.1 s:

$$Q_{PCMP} = \int_{0.003}^{0.1} i \, dt \quad (7.1)$$

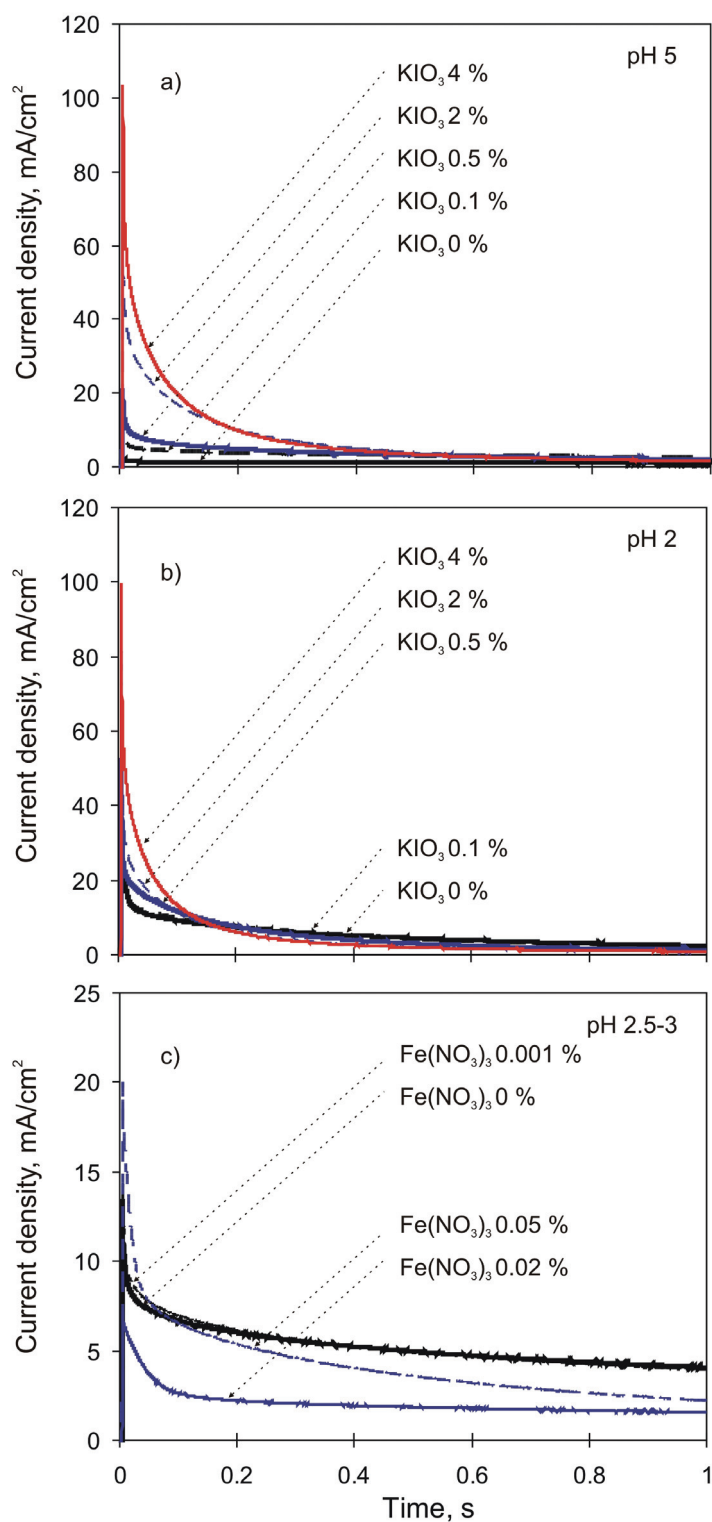


Figure 7.4 Passivation transients for the slurries with different concentration of the oxidizing agent: a) KIO₃ (pH 5), b) KIO₃ (pH 2) and c) Fe(NO₃)₃ (pH 2.5-3).

Table 7.1

Composition of the technical CMP slurries, pH, OCP, $Q_{p, \text{CMP}}$ and CMP removal rates (RR).

Slurry composition		pH	OCP, mV	$Q_{p, \text{CMP}}, \mu\text{C}/\text{mm}^2$	RR, A/min
3 % silica part.	0.0 % KIO ₃	5	-662 ± 15	1 ± 0	40
	0.1 % KIO ₃		-406 ± 3	4 ± 0	140
	0.5 % KIO ₃		-356 ± 5	10 ± 2	750
	2.0 % KIO ₃		-322 ± 7	25 ± 0	1500
	4.0 % KIO ₃		-323 ± 8	33 ± 1	1600
3 % silica part. HCl	0.0 % KIO ₃	2	-554 ± 11	12 ± 1	25
	0.1 % KIO ₃		-121 ± 11	11 ± 1	200
	0.5 % KIO ₃		-75 ± 9	15 ± 0	1150
	2.0 % KIO ₃		-30 ± 9	20 ± 3	1950
	4.0 % KIO ₃		-54 ± 8	25 ± 3	
“RS” 3 % silica part. H ₃ PO ₄ C ₃ H ₆ O ₃ NH ₄ OH	2.0 % KIO ₃	2.75	-150 ± 9	38 ± 2	2300
3 % silica part. 5 % H ₂ O ₂ HCl	0.0 % Fe(NO ₃) ₃	2.5	-296 ± 6	>7 ± 0	300
	0.001 % Fe(NO ₃) ₃	2.5	-85 ± 3	>7 ± 0	
	0.02 % Fe(NO ₃) ₃	3.0	64 ± 7	>4 ± 0	1670
	0.05 % Fe(NO ₃) ₃	2.5	79 ± 9	>9 ± 1	2270

7.3. Discussion

The open circuit potential (OCP) shift to higher values when decreasing pH from 5 to 2 (Figure 7.2 and Figure 7.5) can be explained using the Pourbaix diagram, given in Figure 2.5. In order to calculate the shift of potential due to pH change from 5 to 2 we will use the reaction (2.7). Nernst equation for tungsten oxidation reaction (2.7), at 25°C, can be written as:

$$E_{rev} = -0.119 - 0.059 \text{ pH} \quad (7.2)$$

The equilibrium potential calculated using the Equation (7.2) for the pH 2 is -0.895 V MSE and for pH 5 is -1.072 V MSE. For the pH decrease from 5 to 2 the potential should

change for 180 mV. This is in agreement with the test results shown in Figure 7.2 and Figure 7.5, because the oxidation of tungsten for the pH 5 starts at lower potentials compared to pH 2 (as suggested in Pourbaix diagram for tungsten in Figure 2.5). It is not clear what influences the significant increase of tungsten removal rate for both pH 2 and pH 5 (Figure 7.5) beyond the certain potential value. For the pH 2 this potential (-0.1 V) corresponds to passive region, where WO_3 is already formed, according to Pourbaix diagram (Figure 2.5). For pH 5 and potential of -0.4 V MSE, which is marking significant change of removal rate, only metallic tungsten should be found on the surface. It can be also noticed that for the same slurry composition (KIO_3 slurries) with lower pH, both open circuit potential and removal rate are higher than with pH 5 (Figure 7.5).

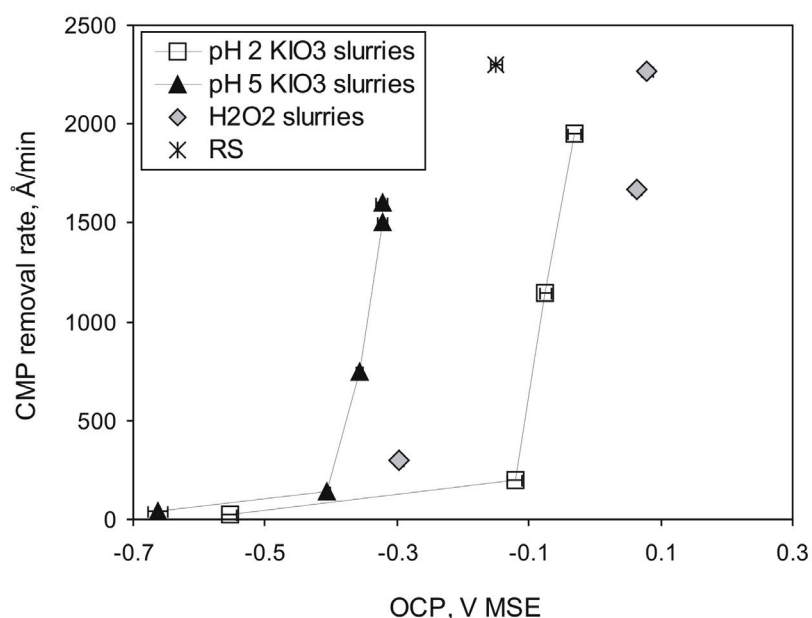


Figure 7.5 Influence of the open circuit potential and pH on the CMP removal rate.

The same trend (higher the *OCP*, higher the removal rate) is observed for the slurry containing H_2O_2 and different concentration of $\text{Fe}(\text{NO}_3)_3$. The slurry RS is also presented in Figure 7.5. High values of removal rates in the case of the slurry RS are probably more related to different chemistry than to its open circuit potential value. In analogy with *OCP* influence, when increasing passivation charge density removal rate increases for both groups of KIO_3 slurries (pH 2 and pH 5), as shown in Figure 7.6. Reference slurry, RS, has the highest removal rate and the highest passivation charge density.

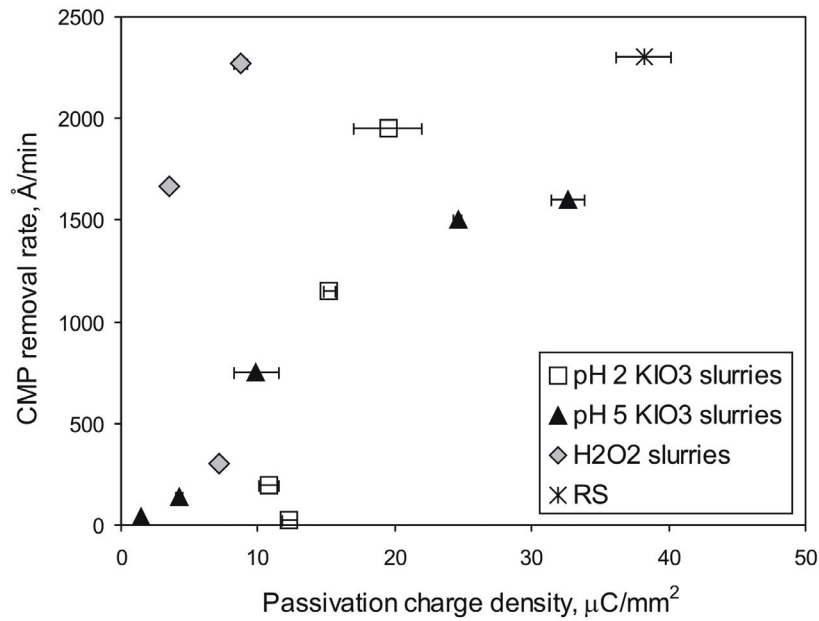
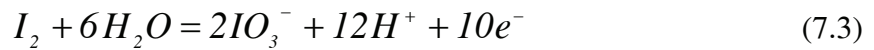


Figure 7.6 Influence of the passivation charge density on the CMP removal rate.

Measured passive current, i , (Figure 7.4) for all the slurries from Table 7.1 is probably highly influenced by the cathodic reaction, as it is explained in the following discussion. According to Pourbaix diagram for I [13] the reaction which is possibly occurring in the presence of KIO_3 slurries is the following one:



The E_{rev} for this reaction are 0.38 V MSE and 0.16 V MSE for pH 2 and pH 5, respectively, according to the equation:

$$E_{rev} = 1.178 - 0.0709\text{pH} + 0.0059 \log \frac{(\text{IO}_3^-)}{(\text{I}_2)} \quad (7.4)$$

As presented in Figure 7.7, the measured current represents the sum of anodic and cathodic currents. The test potential for passivation kinetics measurements was 0.2 V. The influence of the excess cathodic current (reduction of I) can not be neglected for the pH 2. This is schematically shown for the simple electrode in Figure 7.7. On the other hand, for the pH 5, at the potential of 0.2 V the contribution of the anodic current is more important.

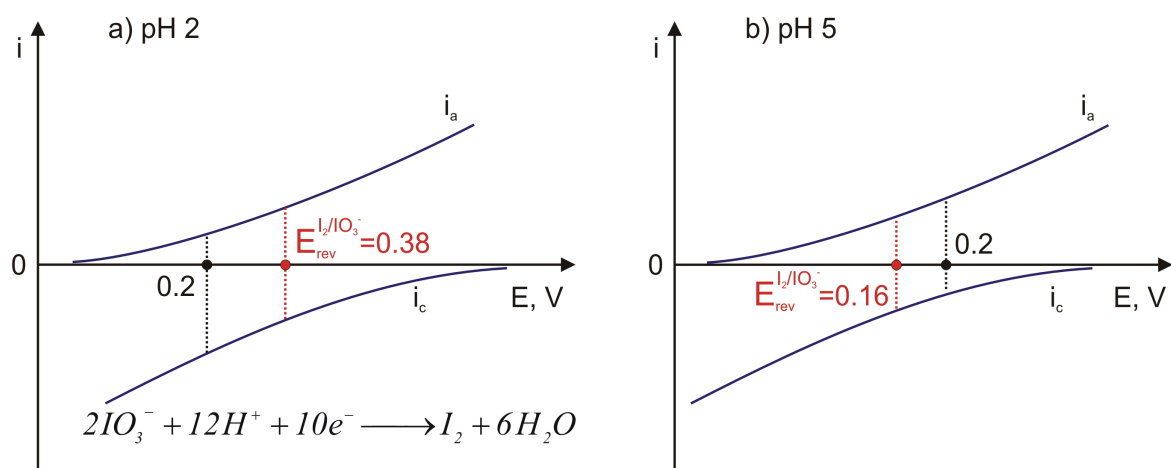


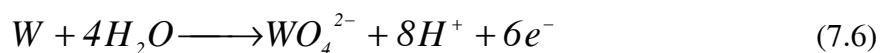
Figure 7.7 Influence of cathodic partial reaction on the resulting current regarding the passivation kinetics measurements undertaken at 0.2 V.

The effect of the important contribution of the i_c in the overall current measured during passivation kinetics measurement is also present in the slurries containing H_2O_2 . Therefore, the calculated Q_{PCMP} values for these slurries (Table 7.1) are underestimated.

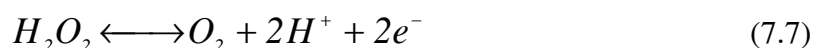
According to Pourbaix diagram [13] for H_2O_2 , the domain where hydrogen peroxide can act as an oxidizing agent and is being reduced to water (Equation 7.5) is situated below the equilibrium potential value (0.93 V MSE) for the reaction:



Acting as oxidizing agent, H_2O_2 can oxidize tungsten to tungstate ions, according to reaction:



Above the potential of -0.09 V MSE which represents the equilibrium potential for the reaction (7.7), hydrogen peroxide can act as a reducing agent with the formation of oxygen:



It can be summarized that hydrogen peroxide is unstable and reducible to water below 0.93 V MSE and unstable and oxidizable to oxygen above the potential of -0.09 V MSE. These two domains of instability have a common area in which hydrogen peroxide is doubly unstable and can decompose into water and oxygen according to the reactions 7.5 and 7.7. The overall reaction for the partial reactions (7.5) and (7.7) is:



Consequently, if slurry containing hydrogen peroxide is in contact with a metallic surface whose electrode potential is situated in this domain of double instability, the hydrogen peroxide can decompose spontaneously into water and oxygen according to the reaction 7.8 [13]. In the performed potential step experiments the imposed electrode potential was 0.2 V MSE which is situated in the hydrogen peroxide double instability region.

The simplifications were made in the passivation kinetics measurements. The imposed potential after the potential change was fixed to 0.2 V (see Chapter 7.1.1). A way to refine the measurements of passivation kinetics should be to take into account the OCP value of the given slurry and to impose the potential corresponding to the OCP of the each slurry augmented by 200 mV. Despite the uncertainty concerning the passivation charge density determination, the influence of passivation kinetics on the removal rate seems to be clear, as shown in Figure 7.6.

7.4. Conclusions

The results of the electrochemical measurements undertaken with technical CMP slurries and removal rates measurements on the CMP machine, show that electrochemical factors (open circuit potential, passivation charge) are strongly influencing the CMP removal rate.

After reaching the threshold potential, the removal rate steadily increases when increasing the *OCP*.

Even though the passivation kinetics measurements for the technical CMP slurries include some simplifications, the tendency of removal rate augmentation with passivation charge increase is observed. This may open a way for the prediction of the removal rate by measuring the open circuit potential and passivation kinetics of the slurry.

CHAPTER 8

8. General Discussion

The existing tribocorrosion models are applied to the tungsten tribocorrosion in sulphuric acid solutions and to the CMP practice. Also, the correlation between the tribocorrosion and the CMP is established.

8.1. Modelling of Tribocorrosion of W in 0.01 M H₂SO₄

The wear of tungsten increases when increasing the thickness of the oxide film in the sulphuric acid solution (Figure 8.1), which is in agreement with the Kaufman's mechanism. Nevertheless, Figure 8.1 shows that the applicability of the Kaufman's mechanism fails in the presence of chelating agents. High wear volumes in the presence of these chelating agents correspond to lower oxide film thicknesses. The Kaufman's mechanism does not consider the possible dissolution accompanying the passive film growth. The thickness presented in Figure 8.1 is measured after 1h of passivation. As we have shown in Chapter 3, during passivation a part of the charge serves for tungsten oxide film growth and part for the dissolution.

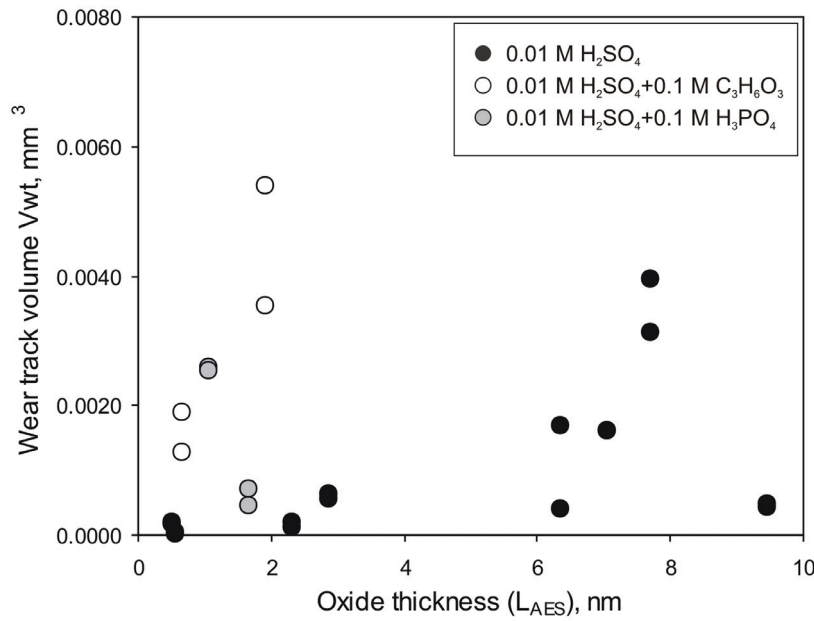


Figure 8.1 Influence of the WO_3 thickness on the total volume of removed material in different solutions.

Tribocorrosion models were developed in the past [1], [40], [43] as shown in Chapter 2.4 to predict the anodic current of passive metals subject to sliding wear in aqueous solutions as a function of passivation charge. Theoretical wear accelerated corrosion current $I_{wac_{th}}$ can be expressed using the following equations:

$$I_{wac_{th}} = R_{dep} Q_p \quad (8.1)$$

For our system composed of two bodies of comparable roughness the value of the exponent b can be taken arbitrarily as of 0.5 (as explained in Chapter 2.4). Using the Equation (2.20) and the Equation (2.21) and taking into account that sliding velocity, v_s , can be expressed as wear track length, l , multiplied by rubbing frequency, f , we can express the depassivation rate as:

$$R_{dep} = K_{st} l f (F_n / H_{wt})^{0.5} \quad (8.2)$$

The wear accelerated corrosion current, $I_{wac_{th}}$, is then equal to:

$$I_{wac_{in}} = K_{st} I_f (F_n / H_{wt})^{0.5} Q_p \quad (8.3)$$

where K_{st} is the proportionality factor whose value so far is not known, F_n is the applied normal load in N, H_{wt} is the micro hardness in the wear track (Table 5.4) and Q_p is the passivation charge density (Table 3.3). To verify the applicability of the model given by Equation (8.1) to our results, the values of I_{wac} obtained in tribocorrosion tests were plotted as a function of the ratio $Q_p / (H_{wt})^{0.5}$ (Figure 8.2). The values Q_p are taken from Table 3.3 (potential step measurements at 0 rpm) and H_{wt} is the micro hardness measured inside the wear track (Table 5.4).

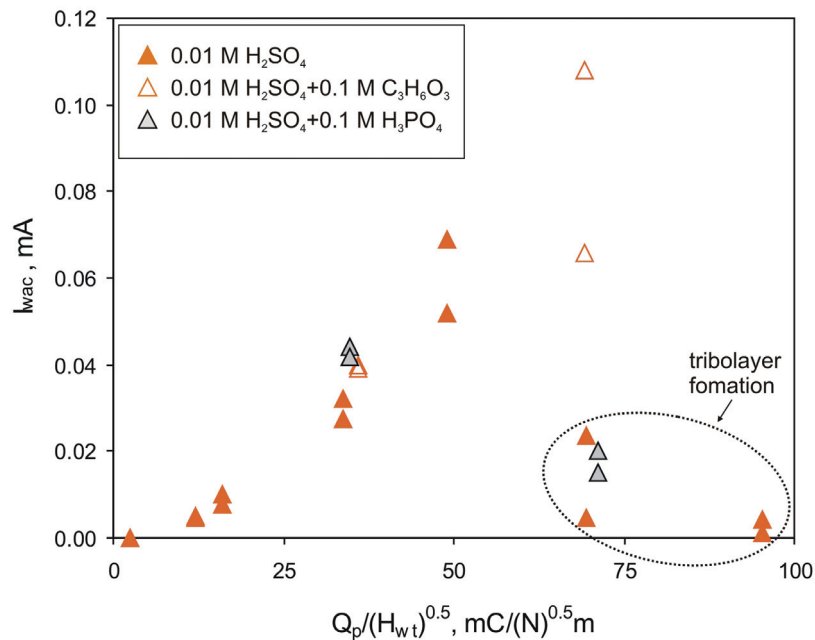


Figure 8.2 Influence of passivation charge density and tungsten micro hardness in the wear track on the wear accelerated corrosion current.

As predicted by Equation (8.3), a linear correlation is found in Figure 8.2, with an exception of the 0.01 M H_2SO_4 and 0.01 M $H_2SO_4 + 0.1$ M H_3PO_4 for the higher values of $Q_p / (H_{wt})^{0.5}$, because of the tribolayer formation in the wear track. The authors [1][40] pointed out that the model does not consider the case of the third body formation. According to Figure 8.2, the amount of removed material can be described by taking into account the passivation charge density, rather than the passive film thickness (Figure 8.1).

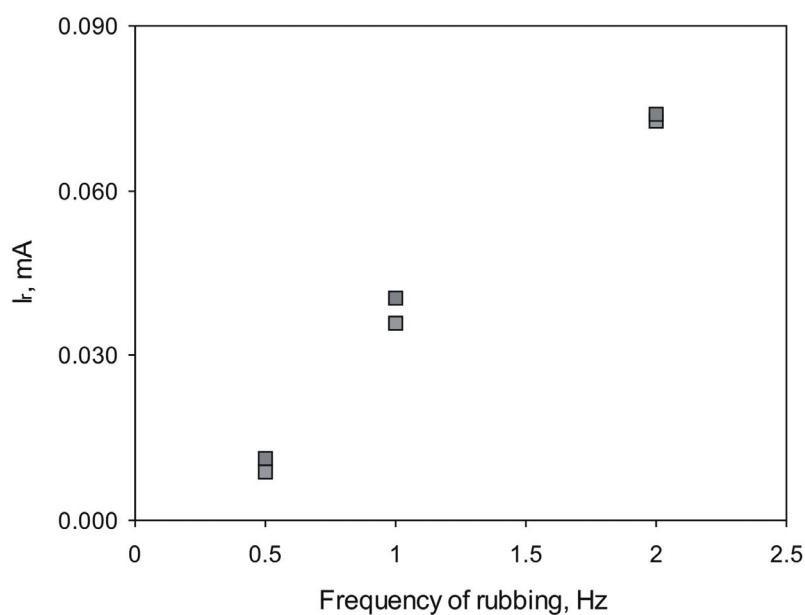


Figure 8.3 Influence of rubbing frequency on the current enhancement due to rubbing in the standard test conditions at the imposed potential of 0.2 V.

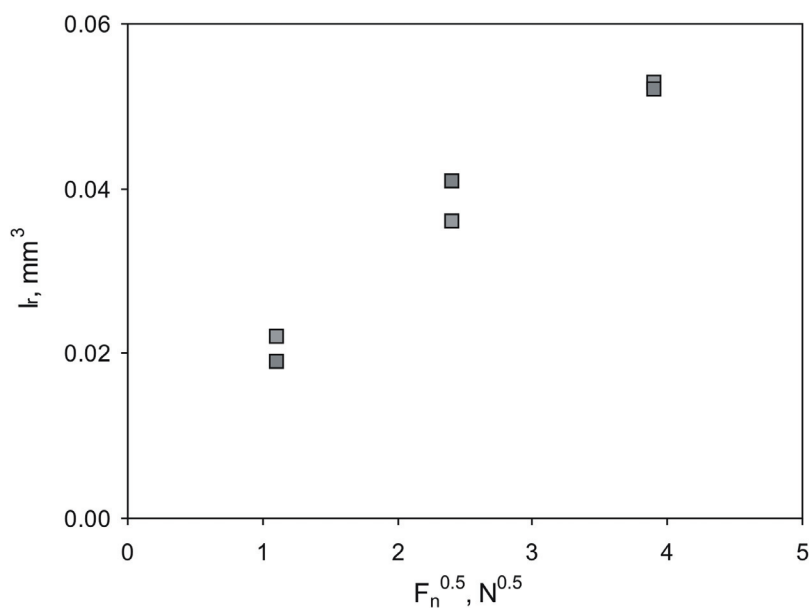


Figure 8.4 Influence of the $F_n^{0.5}$ on the current enhancement due to rubbing in the standard test conditions at the imposed potential of 0.2 V.

Besides the influence of the passivation charge density Q_p on the I_{wac} , the investigated experimental parameters in Chapter 4, frequency of rubbing and normal load, confirmed the applicability and validity of the Mischler's and Landolt's model. The correlation

integrating passive current densities up to the value of 0.5 s. Depassivation rate increases with imposed electrode potential (Figure 8.6) for all the solutions:

$$R_{dep} = f(E) \quad (8.5)$$

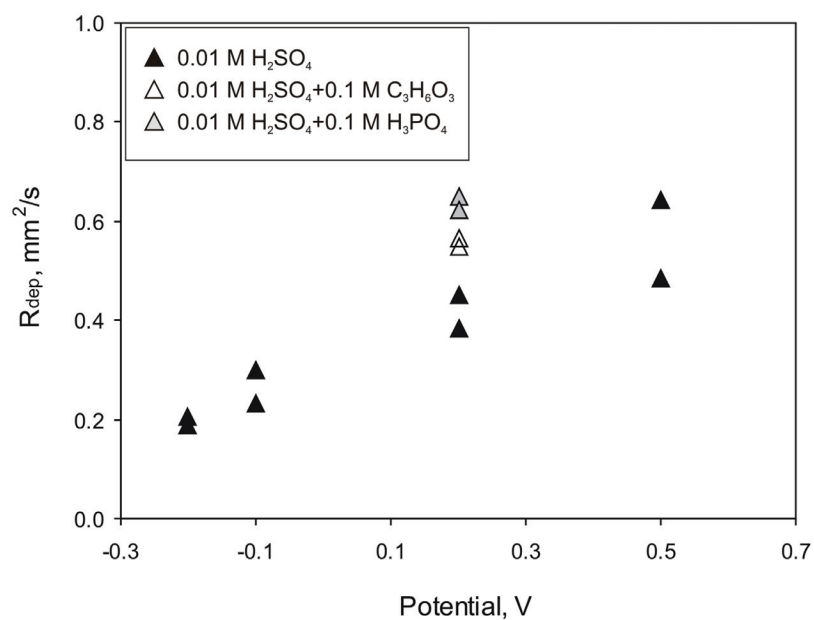


Figure 8.6 Depassivation rate vs. electrode potential.

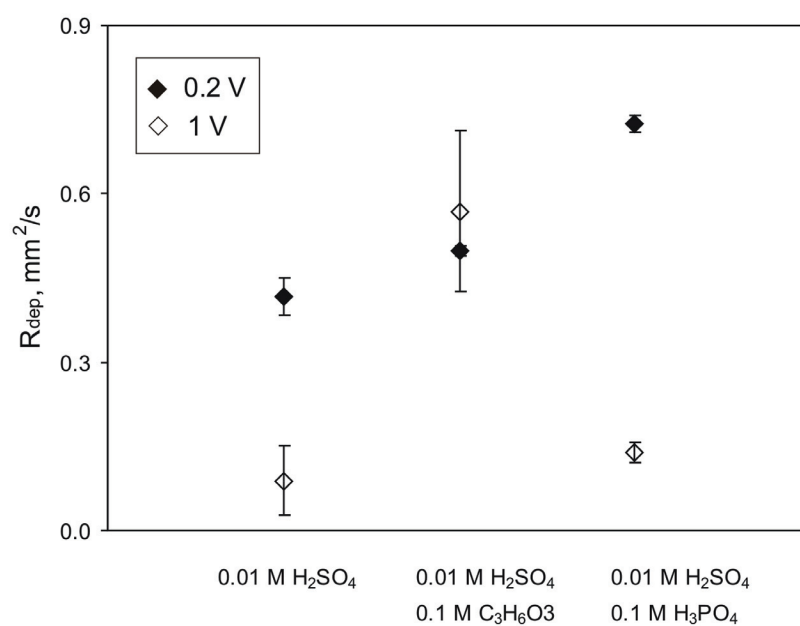


Figure 8.7 Influence of solution composition and electrode potential on depassivation rate.

For the higher potentials (Figure 8.7) R_{dep} decreases due to the formation of the tribolayer in the wear track, except in the presence of lactic acid which suppresses accumulation and compaction of WO_3 rubbed particles in the wear track.

In order to explain the trend of R_{dep} increase with electrode potential, we can take into account the influence of few possible factors: micro hardness in the wear track, proportionality factor K_{st} and internal stresses generated during the passive oxide film formation.

According to the model (Equation 8.2) R_{dep} depends on the micro hardness in the wear track and the increase of R_{dep} could be a result of the decrease in micro hardness with potential. But, this is not in agreement with our micro hardness results (Figure 5.12).

The reason for R_{dep} increase with potential can be explained by the change of the proportionality factor K_{st} . It includes the probability of depassivation of a contacting surface element, in our case the tungsten surface. The model developed by Mischler et al. [40] gave a definition of the K_{st} factor:

$$K_{st} = 2\pi^{-0.5} k_1 (1 - k_2) n_a^{0.5} \quad (8.6)$$

Here, k_1 represents the fraction of the wear track area created by the asperity, becoming effectively depassivated. The factor k_1 depends on the wear mechanism and on the topography of the pin surface. The factor k_2 defines the probability that an asperity contact takes place on an area already depassivated by another asperity. Finally, n_a is the number of asperity contacts determined by the roughness of the rigid body. The model [1] assumes that depassivation is taking place through the plastic deformation at the asperities contact. In our case the alumina ball undergoes wear under certain conditions. This implies the increase of the alumina ball's roughness with potential (Figure 5.8). This results in augmentation of the number of asperities. Hypothetically, higher roughness of the alumina ball augments the probability of depassivation, and according to the Equations (8.2) and (8.5), the R_{dep} increases.

Internal stresses [63] could also have an influence on the R_{dep} change with electrode potential. During the formation of the passive oxide film, generated internal stresses probably depend on the thickness of the formed passive film and in combination with above explained parameters have an effect on the R_{dep} .

In order to estimate the percentage of the depassivated area in the wear track corresponding to one passage of the alumina ball, the maximum wear accelerated corrosion current in the wear track, $I_{wac_{max}}$, was expressed using the Equation (8.7). The maximum depassivation rate, $R_{dep_{max}}$, is equal to $A_{wt}f/2$, where A_{wt} is the wear track surface after rubbing (Table 5.3) and f is the rubbing frequency.

$$I_{wac_{max}} = R_{dep_{max}} Q_p = A_{wt} \frac{f}{2} Q_p \quad (8.7)$$

The percentage of the wear track depassivated during the passage of the alumina ball (Table 8.1) can be expressed as the ratio of the I_{wac} and $I_{wac_{max}}$ for a given potential:

$$\frac{I_{wac}}{I_{wac_{max}}} = \frac{I_{wac}}{A_{wt} \frac{f}{2} Q_p} \quad (8.8)$$

As explained in Chapter 3.2.3, the values of Q_p (Equation 8.8), obtained from the separated potential step measurements, do not absolutely correspond to the real passivation charge necessary to repassivate the activated metal surface after each stoke of alumina ball in the tribocorrosion test. The reason lies in the difficulties related to passivation kinetics' measurements [40]. Therefore these values do not represent the exact in situ repassivation areas but they can be used for comparison purposes.

Table 8.1

Influence of the electrode potential on the estimated percentage of the depassivated area in the wear track corresponding to one passage of the alumina ball.

Potential, V	Depassivated area, %
-0.5	0
-0.5	0
-0.2	50
-0.2	46
-0.1	50
-0.1	64
0.2	69
0.2	81
0.5	84
0.5	111
1.0	6
1.0	33
1.5	6
1.5	2

8.2. Correlation of Tungsten Tribocorrosion Results and CMP Practice

The electrochemical and mechanical differences in the test conditions between the tribocorrosion tests and CMP practice are discussed in Chapter 2.5. One of them relates to the electrode potential. In the tribocorrosion tests the fixed potential is imposed and in the CMP the polishing is performed under the OCP of the slurry. Despite the differences the correlations can be made. The removal mechanism present in both tribocorrosion tests and CMP practice of tungsten corresponds to removal of the oxidized tungsten (Kaufman's mechanism).

In order to compare the rates of material removal in the CMP practice and in tribocorrosion tests, the tungsten tribocorrosion wear rate (WR) was defined as the average thickness change of the tungsten sample during tribocorrosion tests, measured in the wear track, divided by the time of rubbing (Table 8.2). Wear rate was calculated using the values of y , average wear track's depth, expressed in angstroms, and t , rubbing period of 3000 s:

$$WR = \frac{y}{t} \quad (8.9)$$

Table 8.2

Tungsten average wear track's depths and wear rates for different electrode potentials in the 0.01 M H₂SO₄ solution, in the standard tribocorrosion test conditions.

E, V	y, μm	WR, $\text{\AA}/\text{min}$
-1.0	0.19	39
-1.0	0.17	33
-0.5	0.07	15
-0.5	0.06	13
-0.2	0.23	45
-0.2	0.15	29
-0.1	0.59	119
-0.1	0.71	144
0.2	1.52	304
0.2	1.40	280
0.5	2.86	572
0.5	3.17	634
1.0	0.45	90
1.0	1.87	374
1.5	0.67	133
1.5	0.61	121

The values of WR from the tribocorrosion tests are lower than RR from the CMP practice, but the similarities in dependence on the electrode potential are clear. Tungsten removal rate measured on the CMP machine has the same increasing trend with potential increase as the wear rate obtained on the tribometer, as shown in Figure 8.8. Both WR and RR are low up to a threshold potential and beyond they exhibit the linear steady increase. As shown in Table 8.2, WR decreases beyond the potentials of 0.5 V because of the formation of the tribolayer in the wear track. In the tungsten CMP practice these higher potentials can not be reached. The reason lies in difficulties to prepare the technical slurry in which tungsten's open circuit potential will be higher than 0.1 V MSE and to, at the same time, preserve the slurry's stability.

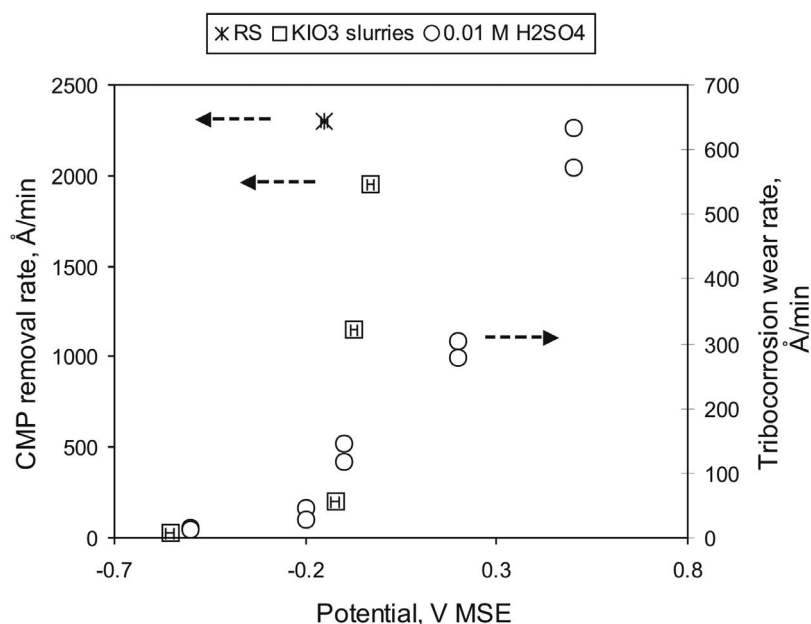


Figure 8.8 Influence of open circuit potential on the removal rate of tungsten obtained during polishing on the CMP machine using technical slurries and on the tribocorrosion wear rate in the 0.01 M H₂SO solution. Note: for the tribocorrosion wear rates obtained in the 0.01 M H₂SO₄ the x-axis values correspond to imposed electrode potential and to OCP for CMP.

The values of the passivation charge evaluated in the CMP slurries and in the sulfuric acid solution can not be directly compared due to uncertainty of their evaluation in the CMP slurries. The choice of integration period influences significantly calculated passivation charge. When the integration limit in the Equation (7.1) instead of 0.1 s is replaced with 0.5 s or 0.05 s the passivation charge changes. In the 0.01 M H₂SO₄ solution passivation charge density was calculated using the Equation (7.1) by integrating the passive current densities gathered from potential step experiments (-1 V MSE to 0.2 V MSE) up to the value of 0.5 s. It is also necessary to pay attention that removal rates obtained on the CMP machine are related to the OCP values of slurries (no potential was imposed on the CMP machine during polishing). The calculated passivation charge (Chapter 7.2.2) is related to the same fixed imposed electrode potential for all the slurries (0.2 V MSE). Also, due to the important influence of the cathodic current during passivation in the CMP slurries, the measured $Q_{p_{CMP}}$ values are underestimated, as

explained in Chapter 7.3. The simplification in the passivation charge evaluation does not diminish the clarity of the increasing trend of the tungsten CMP removal rate (Figure 7.6) and tribocorrosion wear (Figure 8.2) with passivation charge.

8.3. Modelling of Tribocorrosion in CMP

As shown in Chapter 2.1, Preston proposed a mathematical model (Equation 2.1) for the calculation of the removal rate in the CMP process. According to this model, removal rate, *RR*, increases (among other parameters) with normal load increase during polishing. The tribocorrosion model proposed by Landolt and Mischler (Equation 8.3), predicts the augmentation of the material removal with the increase of the real contact pressure. Instead of the macroscopic contact pressure (Preston's equation), the later model relates to microscopic contact pressure.

Table 8.3

Composition of the slurries, calculated V_{wacCMP} , I_{wacCMP} and i_{wacCMP} .

Slurry composition		V_{wacCMP} , mm ³	I_{wacCMP} , mA	i_{wacCMP} , mA/cm ²
3 % silica part.	0.0 % KIO ₃	0.031	32	0
	0.1 % KIO ₃	0.110	111	1
	0.5 % KIO ₃	0.589	597	8
	2.0 % KIO ₃	1.178	1193	15
	4.0 % KIO ₃	1.257	1273	16
3 % silica part. HCl	0.0 % KIO ₃	0.020	20	0
	0.1 % KIO ₃	0.157	159	2
	0.5 % KIO ₃	0.903	915	12
	2.0 % KIO ₃	1.532	1551	20
“RS” 3 % silica part. H ₃ PO ₄ C ₃ H ₆ O ₃ NH ₄ OH	2.0 % KIO ₃	1.806	1830	23
3 % silica part. 5 % H ₂ O ₂ HCl	0.0 % Fe(NO ₃) ₃	0.236	239	3
	0.02 % Fe(NO ₃) ₃	1.312	1328	17
	0.05 % Fe(NO ₃) ₃	1.783	1806	23

As previously presented in Chapter 5.3, tungsten removal mechanism corresponds to the removal of the oxidized metal. The total removed material is approximately equal to the volume of the wear accelerated corrosion, V_{wac} (Figure 5.13). The volume of wear accelerated corrosion in the CMP process (Table 8.3), $V_{wac_{CMP}}$ was obtained by converting the measured removal rates (RR) on the CMP machine as:

$$V_{wac_{CMP}} = RR \cdot t_{CMP} \cdot A_w \quad (8.10)$$

where t_{CMP} is the duration of CMP polishing tests (60 s) and A_w is the surface of the wafer (7854 mm²). Using Faraday's law, the values of $I_{wac_{CMP}}$ (Table 8.3) can be calculated:

$$I_{wac_{CMP}} = \frac{V_{wac_{CMP}} n F \rho}{t_{CMP} M} \quad (8.11)$$

The current density $i_{wac_{CMP}}$ was calculated as $i_{wac_{CMP}} = I_{wac_{CMP}} / A_w$, and given in Table 8.3. Its values are comparable to the values of the current density in the wear track from the tribocorrosion tests, $i_{wac} = I_{wac} / A_{wt}$, calculated using the values I_{wac} and A_{wt} from Table 5.1 and Table 5.3, respectively. The i_{wac} values are in the range from 1 mA/cm² up to 6 mA/cm².

In order to estimate the theoretical current generated by wear accelerated corrosion in the CMP, $I_{wac_{CMP,th}}$, the Equation (8.12) will be used:

$$I_{wac_{CMP,th}} = R_{dep_{CMP}} Q_{p_{CMP}} \quad (8.12)$$

where $R_{dep_{CMP}}$ is the depassivation rate of tungsten in the CMP. In analogy with the Equation (8.2) we can express the $R_{dep_{CMP}}$ as:

$$R_{dep_{CMP}} = K_{st_{CMP}} v_{s_{CMP}} \left(\frac{F_{n_{CMP}}}{H_{CMP}} \right)^{0.5} \quad (8.13)$$

where v_{sCMP} is the linear velocity of any point on the wafer, which can be calculated using the Equation 8.14 proposed by Zantye [3]. In this equation the parameters ω_T and r_{cc} are the rotation rate of the platen holding the pad and the distance of the centers of the wafer and pad, respectively. Pad diameter is 558.8 mm (22") and the value of r_{cc} is taken as constant (140 mm).

$$v_{sCMP} = -|\omega_T r_{cc}| \quad (8.14)$$

Normal load in the CMP can be calculated using the pressure on the wafer head, P , (see Chapter 7.1.2) whose value is 5 psi or 34.5 kPa:

$$F_{nCMP} = PA_w \quad (8.15)$$

Hardness of the tungsten wafer surface layer in the CMP, H_{CMP} , is not a known value, but we can approximately take it as the hardness of our tungsten samples (3.7 GPa).

The K_{sCMP} factor can be defined as in the tribocorrosion modelling:

$$K_{sCMP} = 2\pi^{-0.5} k_1 (1 - k_2) n_{part}^{0.5} \quad (8.16)$$

where n_a , the number of asperities contacts in the tribocorrosion test, is replaced with n_{part} , the number of particles contributing to the depassivation of the wafer surface. We have explained in the analysis of the tribocorrosion results (Figure 8.6 and Equation 8.2) that depassivation rate increases due to increased number of asperities on the counter body (alumina ball). In analogy with the modelling of tribocorrosion of tungsten, we can discuss the hypothesis of the influence of the number of asperities contacts in the CMP micro plastic deformation on R_{depCMP} . In the CMP practice the R_{depCMP} should increase when increasing abrasive particles concentration [64]. If the concentration of abrasive particles increases the R_{depCMP} will increase until a certain value but with excessive augmentation of abrasives the saturation in R_{depCMP} will occur. This, indeed, was observed by Paul et al [64], who showed that initial polishing rate increase was followed by the asymptotic maximum as the abrasive concentration increased.

In order to calculate the $I_{wac_{CMP,th}}$ we will roughly estimate the number of particles n_{part} contributing to the depassivation of the wafer surface. The number of particles contributing the depassivation of the wafer surface, n_{part} is influenced by the separation distance $d_{sep} = f(F_{n_{CMP}}, v_{s_{CMP}}, d_{part})$ between the wafer and the pad during polishing under pressure [65]. Some of the particles can be embedded in the pad [66] and others are captured by asperities [67]. Also, besides the sliding motion, the rolling is taking place for certain number of particles in CMP [59]. Due to these effects the evaluation of the n_{part} is complex and remains the subject of the active studies. For the estimation of n_{part} we can use both Equation (8.17) and (8.18).

The first one, (Equation 8.17) represents the estimation of n'_{part} , the number of particles in the volume of the slurry V_{ml} , corresponding to the thickness of the monolayer of the particles near the wafer surface, d_{part} multiplied by A_w :

$$n'_{part} = \frac{m_{ml}}{m_{part}} = \frac{V_{ml} c_{part}}{V_{part} \rho_{SiO_2}} = \frac{A_w d_{part} c_{part}}{\frac{4}{3} \pi \cdot r_{part}^3 \rho_{SiO_2}} \quad (8.17)$$

where m_{ml} and m_{part} are the mass of all silica particles in the V_{ml} slurry volume and the mass of a single particle, respectively. The volume of the single particle, V_{part} , can be calculated using its radius, $r_{part} = 6$ nm (see Chapter 7). Concentration of the silica particles in the CMP slurries, c_{part} , is given in Table 7.1 (30 g/l). Density of the silica particles, ρ_{SiO_2} , is 2.2 g/cm³.

The second, Equation (8.18) represents the estimation of n''_{part} , the number of particles in V_{CMP} , corresponding to the slurry volume between the wafer and the pad determined with the separation distance, d_{sep} .

$$n''_{part} = \frac{m_{CMP}}{m_{part}} \quad (8.18)$$

$$m_{CMP} = V_{CMP} c_{part} = A_w d_{sep} c_{part} \quad (8.19)$$

where m_{CMP} is the mass of all silica particles in the V_{CMP} slurry volume. The separation distance, d_{sep} , between the wafer and the pad during polishing under pressure was studied by Jeng et al. [65]. According to their results and regarding our values for $F_{n_{CMP}}$, $v_{s_{CMP}}$ and d_{part} , we can approximately take d_{sep} as of 28 μm .

Passivation charge density necessary for the repassivation of the surface activated by the single particle in the CMP, $Q_{p_{CMP}}^*$, could be estimated using the Equation (8.20). Equation (8.21) served for the calculation of the time which one particle takes between two depassivation actions, $t_{part} = 2 \cdot 10^{-7}$ s. The parameter s_{part} refers to the linear distribution of particles contributing the surface depassivation. The peak current density, i_{peak} , is taken from the passivation transients measurements in the CMP slurries (Figure 7.4) for the slurry with pH 2 and 2 % of KIO_3 (81.3 mA/cm^2).

$$Q_{p_{CMP}}^* = i_{peak} t_{part} \quad (8.20)$$

$$t_{part} = \frac{s_{part}}{v_{s_{CMP}}} = \frac{\left(\frac{V_{ml}}{n_{part}}\right)^{1/3}}{v_{s_{CMP}}} \quad (8.21)$$

The $I_{wac_{CMP,th}}$ (Equation 8.12), calculated using the above explained parameters and approximations (assuming that $k_1=1$ and $k_2=0.5$), has the value of 0.2 A for n'_{part} and 9.2 A for n''_{part} , which represent the two extreme cases regarding the number of particles (minimum and maximum). These values are of the same order of magnitude as the $I_{wac_{CMP}}$ (Table 8.3), confirming the applicability of the model to the CMP practice taking into account the chemical, mechanical and material factors.

8.4. Conclusions

The tribocorrosion behavior of tungsten can not be explained using the mechanism of material removal given by Kaufman, which correlates the removal rate only to the thickness of the formed oxide film. Also, the tungsten tribocorrosion behavior does not follow the Quinn's model for oxidative wear which takes into account only the passivation phenomena, because the tribocorrosion of tungsten is found to be a specific case where the dissolution interferes. Therefore, by applying the tribocorrosion model developed by Landolt and Mischler [1][40], the good agreement with experimental data is found, in both tribocorrosion tests and CMP practice.

Tungsten removal rate obtained on the CMP machine and the wear rate obtained on the tribometer have similar increasing trends when increasing open circuit potential (electrode potential) and passivation charge density. These findings approve the chosen approach to investigate the tribocorrosion of tungsten using the model tests, rather than using the real CMP machine, and give a possibility to extrapolate the tribocorrosion tests results to the CMP.

The presented model for the CMP is in semi quantitative agreement with the CMP practice. The limits are related to the passivation charge density determination in the CMP slurries and to the nature of the contact.

CHAPTER 9

9. Conclusions

Parameters influencing the removal of tungsten are various with complex interactions among them. The presented study contributes to the better understanding of the influence of firstly, the electrode potential and secondly, the solution chemistry (chelating agents) on the tribocorrosion of tungsten in the chemical – mechanical polishing (CMP).

9.1. Contribution of This Work

Corrosion of Tungsten in Sulphuric Acid Solutions

The thickness of the WO_3 found using the surface analyses techniques (XPS, AES) on the tungsten surface in the whole electrode potential range from -1 V up to 1.5 V MSE is increasing with potential.

Passivation charge in the initial period of passivation increases linearly when increasing electrode potential and is not affected by mass transport (neither by the presence of chelating agents nor by rotation rate).

The mass transport controlled dissolution of the formed passive film on tungsten occurs after the initial period of passivation. It is induced by the rotation and the presence of chelating agents, and not by the electrode potential. Therefore, the formed oxide film on tungsten is thinner in the presence of chelating agents compared to its thickness in 0.01 M H_2SO_4 .

Tribocorrosion of Tungsten in Sulphuric Acid Solutions

The approach combining the electrochemical and tribological techniques, which was not used by many researches, is chosen here to study the tribocorrosion behavior of tungsten. It allows us to distinguish the volume of chemically removed metal volume from the volume of mechanically removed metal.

Tribocorrosion of tungsten is critically affected by electrochemical (corrosion) conditions. The wear of tungsten in the 0.01 M H₂SO₄ solution depends on electrode potential. Two threshold potentials can be observed, at -0.5 V and 0.5 V.

Below -0.5 V, wear is nearly independent of electrode potential because only negligible oxidation occurs in this potential region.

In the region of potentials from -0.5 V up to 0.5 V wear increases with potential because WO₃ passive film thickness increases with potential. Material deterioration in the rubbed area proceeds by cyclic mechanical removal of the WO₃ passive film followed by repassivation of tungsten.

Above 0.5 V wear volume decreases due to formation of a tribolayer in the wear track, formed by compaction of WO₃ debris particles, which reduces wear and chemical activity.

The amount of anodic oxidation corresponds to the overall removed metal volume indicating that tungsten is removed as oxidized metal. Only small part of the tungsten wear volume represents the mechanical wear.

The mass transport controlled dissolution of tungsten through the passive WO₃ film formed out of the wear track increases under solution stirring (provoked by the motion of the alumina ball and its holder). Current enhancement due to rubbing should be corrected taking into account the contribution of the mass transport current in order to correctly evaluate the wear accelerated corrosion current, proportional to the oxidation of tungsten.

Lactic acid suppresses tribolayer formation in the wear tracks at the potential of 1 V by accelerating the dissolution process and thinning the oxide film. At the same potential in the presence of phosphoric acid a tribolayer, similar to one formed in the 0.01 M H₂SO₄ solution, forms in the wear track area and reduces wear. At lower potentials, chelating agents lactic and phosphoric do not have a significant impact on tribocorrosion behavior of tungsten.

Tungsten in the CMP Practice

Electrochemical parameters (*OCP*, passivation charge) are strongly influencing the CMP removal rate. Tungsten removal rate obtained on the CMP machine and the wear rate obtained on the tribometer have similar increasing trends when increasing open circuit potential (electrode potential). Similar correlation is observed for the passivation charge density influence on the removal and wear rate, despite the uncertainties in the passivation kinetics measurements in the CMP slurries. These findings approve the chosen approach to investigate the tribocorrosion of tungsten using model tests together with the real CMP machine. Under given CMP polishing conditions (known open circuit potential, passivation kinetics and slurry composition) it would be possible to rationalize the industrial CMP outcome based on the developed scientific criteria.

Modelling the Tungsten Tribocorrosion and the CMP Practice

The original Kaufman's mechanism predicts wear to be proportional to the tungsten oxide film thickness formed on the metal surface and we have shown that this prediction is not always applicable, such as in the presence of additives in the solution (lactic and phosphoric acid).

Tribocorrosion behavior of tungsten in all the solutions is in a good qualitative and quantitative agreement with established tribocorrosion models, taking into account the passivation charge, frequency of rubbing and normal load.

The model can be as well successfully applied to tungsten CMP practice. The assumption is made that the number of asperities in tribocorrosion contact corresponds to the number of abrasive particles in the CMP slurry contributing to the depassivation of tungsten wafer's surface.

Both the Preston and tribocorrosion model are in agreement regarding the influence of the normal load and sliding velocity on the CMP removal rate.

The advantage of the tribocorrosion model is that it allows to semi quantitatively predict the effect of (electro)-chemical and material parameters, such as passivation charge, on the tungsten removal phenomena in CMP, with a reasonable approximation.

9.2. Outlook

This PhD project rationalises the possibility to improve tungsten CMP removal rate by placing the open circuit potential (*OCP*) of the solution in the potential region corresponding to a maximal wear rate. The problem of adjusting slurry's *OCP* caused by its instability in the presence of abrasive particles could be overcome in the electrochemical-mechanical polishing (ECMP), where the oxidizing conditions are established by using the external power source instead of oxidizing agents. The ECMP offers the possibility of the slurry chemistry's simplification. This requires the installation of the potentiostat on the CMP machine. Adjustment of the imposed electrode potential to each metal to be polished could be a significant advantage of the ECMP process.

CHAPTER 10

10. References

- [1] D. Landolt, S. Mischler, M. Stemp, *Electrochim. Acta* 46 (2001) 3913.
- [2] M. Ziomek-Moroz, A. Miller, J. Hawk, K. Cadien, D.Y. Li, *Wear* 255 (2003) 869.
- [3] P. B. Zantye, A. Kumar, A. K. Sikder, *Mater. Sci. Eng. R* 45 (2004) 89, A Review Journal
- [4] F.B. Kaufman, D. B. Thompson, R. E. Broadie, M. A. Jaso, W.L. Guthrie, D. J. Pearson, M. B. Small, *J. Electrochem. Soc.* 138 (1991) 3460.
- [5] S. Mischler, *Tribol. Int.* 41 (2008) 573.
- [6] IBM Patent, No. 4 944 836 (1990)
- [7] D. Tamboli, S. Seal, V. Desai, *Mat. Res. Soc. Symp. Proc. Vol. 566* (2000) 89.
- [8] J. M. Steigerwald, S. P. Murarka, R. J. Gutmann, John Wiley & Sons, Inc., New York (1997)
- [9] US Patent, No. 5500234 (2005)
- [10] US Patent, No. 5996127 (2003)
- [11] *Handbook of Chemistry and Physics*, 73rd Ed. D. R. Lide (1992-1993)
- [12] D. Landolt, *Corrosion and Surface Chemistry of Metals*, Lausanne, EPFL Press, distributed by CRC Press (2007)
- [13] M. Pourbaix, *Atlas of Electrochemical Equilibria in Aqueous Solutions*, National Association of Corrosion Engineers (1974)
- [14] J. W. Johnson, C. L. Wu, *J. Electrochem. Soc.* 118 (1971) 1909.
- [15] F. Di Quarto, A. Di Paola, C. Sunseri, *J. Electrochem. Soc.* 127 (1980) 1016.
- [16] A. Di Paola, F. Di Quarto, C. Sunseri, *Corros. Sci.* 20 (1980) 1067.
- [17] S. B. Akonko, D. Y. Li, M. Ziomek-Moroz, J. Hawk, A. Miller, K. Cadien, *Wear* 259 (2005) 1299.
- [18] M. Anik, K. Osseo-Asare, *J. Electrochem. Soc.* 149, No. 6 (2002) B224.
- [19] M. Anik, *Turk. J. Chem.* 26 (2002) 915.
- [20] M. Anik, T. Cansizoglu, *J. Appl. Electrochem.* 36 (2006) 603.

- [21] D. Tamboli, S. Seal, V. Desai, A. Maury, J. Vac. Sci. Technol. A 17, No. 4 (1999) 1168.
- [22] C.-O. A. Olsson, M.-G. Vergé, D. Landolt, J. Electrochem. Soc. Vol. 151, No. 12 (2004) B652.
- [23] D. D. Macdonald, E. Sikora, J. Sikora, Electrochim. Acta, Vol. 43 (1998) 2851.
- [24] C.-O. A. Olsson, M. Stemp, Electrochim. Acta, Vol. 49 (2004) 2145.
- [25] M.-G. Vergé, Institut des matériaux, Ecole Polytechnique Fédérale de Lausanne, Doctoral thesis No 2791 (2003)
- [26] M.-G. Vergé, C.-O. A. Olsson, D. Landolt, Corros. Sci. 46 (2004) 2583.
- [27] K. Osseo-Asare, M. Anik, J. DeSimone, Electrochem. Solid-State Lett. 2, No. 3 (1999) 143.
- [28] M. Anik, Corr. Science 48 (2006) 4158.
- [29] I. M. Hutchings, *Tribology, Friction and Wear of Engineering Materials*, Edward Arnold (1992)
- [30] B. Ivkovic, A. Rac, *Tribology*, Yugoslav Tribology Society, Kragujevac (1995)
- [31] P. J. Blau, *ASM Handbook: Friction, Lubrication, and Wear Technology*, Vol. 18 (1992) ASM International, 175.
- [32] K.-H. Zum Gahr, *Microstructure and wear of materials*, Elsevier (1987) 80.
- [33] K. Holmberg, A. Matthews, *Coating Tribology*, Elsevier (1994) 49.
- [34] D. Landolt, S. Mischler, M. Stemp, S. Barril, Wear 256 (2004) 517.
- [35] D. Landolt, J. Phys. D: Appl. Phys. 39 (2006) 3121.
- [36] P. Jemmely, S. Mischler, D. Landolt, Wear 237 (2000) 63.
- [37] S. Mischler, E. A. Rosset, D. Landolt, *Thin films in Tribology*/D.Dowson at al. (Editors) (1993) 245.
- [38] P. Pontiaux, F. Wenger, D. Drees, J.P. Celis, Wear 156 (2004) 459.
- [39] S. Mischler, P. Ponthiaux, Wear 248 (2001) 211.
- [40] S. Mischler, S. Debaud, D. Landolt, J. Electrochem. Soc. Vol. 145, No. 3 (1998) 750.
- [41] S. Barril, S. Mischler, D. Landolt, Wear 256 (2004) 963.
- [42] M. Stemp, S. Mischler, D. Landolt, Wear 255 (2003) 466.
- [43] J. Jiang, M. M. Stack, Wear 261 (2006) 954.
- [44] C.-W. Liu, W.-T. Tseng, B.-T. Dai, C.-Y. Lee, C.-F. Yeh, CMP-MIC Conference (1996) 138.
- [45] R. Singh, R. Bajaj, MRS Bulletin Vol. 27. No. 10 (2002) 743.
- [46] S. Perry, H. C. Galloway, P. Cao, E. J. R. Mitchell, D. C. Koeck, C. L. Smith, M. S. Lim, Appl. Surf. Sci. 180 (2001) 6.
- [47] E. A. Kneer, C. Raghunath, S. Raghavan, J. S. Jeon, J. Electrochem. Soc. 143, No. 12 (1996) 4095.
- [48] M. Anik, K. Osseo-Asare, Electrochemical Society Proceedings Volume 37 (1999) 354.
- [49] Y.-J. Seo, N.-H. Kim, W.-S. Lee, Microelectron. Eng. 83 (2006) 428.
- [50] Y.-J. Seo, N.-H. Kim, W.-S. Lee, Mater. Lett. 60 (2006) 1192.

- [51] Y.-J. Seo, W.-S. Lee, *Mater. Sci. Eng. B* 118 (2005) 281.
- [52] Y.-J. Seo, W.-S. Lee, *Microelectron. Eng.* 77 (2005) 132.
- [53] Y.-J. Seo, *Microelectron. Eng.* 84 (2007) 2769.
- [54] C. Raghunath, K. T. Lee, A. Kneer, V. Mathew, S. Raghavan, *Electrochemical Society Proceedings Volume 22* (1996) 1.
- [55] H. Liang, F. Kaufman, R. Sevilla, S. Anjur, *Wear* 211 (1997) 271.
- [56] US Patent, No. 6689692 (2004)
- [57] M. Biemann, U. Mahajan, R. Sigh, P. Agarwal, S. Mischler, E. Rosset, D. Landolt, *Mat. Res. Soc. Symp. Proc. Vol. 566* (2000) 97.
- [58] D. J. Stein, D. Hetherington, T. Guilinger, J. Cecchi, *J. Electrochem. Soc.* Vol. 145, No. 9 (1998) 3190.
- [59] D. Sun, J. A. Wharton, R. J. K. Wood, L. Ma, W. M. Rainforth, *Tribol. Int.* 42 (2009) 99.
- [60] S. Mischler, H. J. Mathieu, D. Landolt, *Surf. Interface Anal.* 11 (1988) 182.
- [61] S. Tanuma, C. J. Powell, D. R. Penn, *Surf. Interface Anal.* 35 (2003) 268.
- [62] *Handbook of X-ray Photoelectron Spectroscopy*, Perkin-Elmer Corporation, Physical Electronics Division (1992)
- [63] J.-D. Kim, S.-I. Pyun, R. A. Orian, *Electrochim. Acta*, Vol. 40 No. 9 (1995) 1171.
- [64] E. Paul, J. Horn, Y. Li, S. V. Babu, *Electrochem. Solid-State Lett.* 10 (4) (2007) H131.
- [65] Y.-R. Jeng, P.-Y. Huang, W.-C. Pan, *J. Electrochem. Soc.* 150, No. 10 (2003) G630.
- [66] W. Choi, S.-M. Lee, J. Abiade, R. K. Sing, *J. Electrochem. Soc.* 151, No. 5 (2004) G368.
- [67] J. Luo, D. Dornfeld, *IEEE T Semiconduct M*, Vol. 14, No. 2 (2001) 112.
- [68] H. J. Pearson, G. T. Burstein, R. C. Newman, *J. Electrochem. Soc.* 128, No. 11 (1981) 2297.
- [69] M. Stemp, *Institut des matériaux, Ecole Polytechnique Fédérale de Lausanne, Doctoral thesis No 2292* (2001)

Appendix A: Ohmic Drop Influence

The current passing between the working electrode and counter electrode in the three electrode cell leads to formation of the potential gradient in the electrolyte resulting in the ohmic potential drop between the reference electrode and the working electrode. This drop is always included in the measured potential of the working electrode.

Therefore, the measured potential in three electrode electrochemical cell, $E_{measured}$, is not exactly equal to the potential imposed by potentiostat, E , because of the ohmic potential drop $I \cdot R_{\Omega}$:

$$E_{measured} = E + IR_{\Omega} \quad (A.1)$$

The ohmic potential drop can often be a practical limit to the precision of potential measurement. In order to reduce the potential drop it is important to place the reference electrode as close as possible to the working electrode (for example by using the Luggin tip).

During the measurement of an open circuit potential (potential measurement without any current flowing), the ohmic drop is always zero, and the position of the reference electrode is not of importance.

The modelling of repassivation during tribocorrosion has shown that the ohmic resistance could have a significant effect on the overall wear of the system. [36]

Influence of the ohmic drop phenomena on the potential drop in tribocorrosion test

The influence of ohmic drop phenomena on an eventual potential drop in our tribocorrosion test was evaluated. The ohmic resistance was calculated using the equation derived by Pearson et al. [68] for a rectangular strip electrode.

$$R_{\Omega} = \frac{1}{2 \cdot \pi \cdot \kappa \cdot b} \ln \left\{ 2 \left[\left(1 + \frac{b^2}{a^2} \right)^{0.5} + \frac{b}{a} \right] \right\} \quad (\text{A.2})$$

where κ is the electrolyte conductivity, a is half the width of the wear track and b is half the length of the wear track.

Table A-1

Calculated ohmic resistance (R_{Ω}) and potential drop (E_{Ω}) values as a function of imposed electrode potential.

Potential, V	R_{Ω} , Ω	E_{Ω} , mV
-0.2	60.1	1.3
-0.2	59.9	1.5
-0.1	55.5	1.9
-0.1	56.1	1.9
0.2	52.5	3.6
0.2	52.2	3.9
0.5	52.2	4.2
0.5	50.6	5.4
1.0	54.9	2.5
1.0	54.7	3.7
1.5	57.1	3.0
1.5	57.3	2.8

Low values of the potential drop E_{Ω} indicate negligible influence of ohmic drop phenomena in our tribocorrosion experiments.

The limitation of this equation is the neglect of the counter part effect, but as we haven't observed the wear of alumina ball after the tribocorrosion tests, the use of the Equation (A.1) is justified. As previously given in Chapter 3.1.1 the conductivity, κ , of the solution the 0.01 M H₂SO₄ has the value of 6.22 mS/cm. The calculated ohmic resistance R_{Ω} is given in Table D-1. The ohmic drop E_{Ω} (Table A-1) was calculated using the following equation:

$$E_{\Omega} = I \cdot R_{\Omega} \quad (\text{A.3})$$

where I is the overall measured current during rubbing for each imposed electrode potential.

Calculated ohmic resistance and ohmic drop correspond to the measured values for the similar system [69].

Appendix B: Tungsten Samples Preparation Prior to Tribocorrosion Experiments

Before polishing tungsten samples were cleaned in ultrasonic acetone bath for 3 min, rinsed with distilled water and dried using dry air.

Mechanical polishing was performed on an automatic polishing machine ABRAMIN Struers, using grit paper 80, 220, 320, 1000, 2400 and 4000. Polishing with each paper lasted for 20 minutes, at rotation speed of 150 rpm and applied force of 400 N. The lubricant was water.

The samples mounted in the polishing support were rinsed with acetone and distilled water and dried using dry air before changing the type of a grit paper.

Diamond sprays DP 1 μm and $\frac{1}{4}$ μm were used for the following polishing steps, respectively, each during 15 min. Used polishing cloths for this step were DP Mol cloths. Every 2 min the cloth surface was sprayed and every 1 min lubricant Struers DR Red was applied. Rotating speed of polishing was 300 rpm and applied force was 400 N.

After polishing and prior to tribocorrosion experiments tungsten samples were cleaned in ultrasonic ethanol bath for 5 min, rinsed with distilled water and dried using an argon jet.

Al_2O_3 ball preparation for tribocorrosion experiments consisted of cleaning in ultrasonic ethanol bath for 5 min and drying with an argon jet.

Appendix C: Hertzian Initial Point Contact and Pressure

When a sphere of an elastic material is pressed against a plane under a normal load F_n , contact will occur between the two over a circular area of radius a . The size of the contact surface is determined by the applied normal load and deformational properties of both materials in contact.

The radius, a^* , of a contact area can be calculated using an equation given by Hertz [29]:

$$a^* = \left(\frac{3F_n r}{4E^*} \right)^{1/3} \quad (\text{C.1})$$

where r is the radius of the sphere and E^* is an effective Young's modulus. E^* depends on Young's moduli of both materials in contact, E_1 and E_2 , and on their Poisson's ratios, ν_1 and ν_2 :

$$\frac{1}{E^*} = \left(\frac{1-\nu_1^2}{E_1} \right) + \left(\frac{1-\nu_2^2}{E_2} \right) \quad (\text{C.2})$$

The tribological system used in this PhD thesis was composed of alumina ball (3 mm radius) and tungsten disk, whose Young's moduli and Poisson's ratios are given in Chapter 2.2, respectively. Using the Equations (C.1) and (C.2) we have calculated the radius of a contact area, which has the value of $0.04 \cdot 10^{-3}$ m.

Mean Hertzian contact pressure of 1.19 GPa was obtained by dividing normal force of 6 N used in tribocorrosion experiments by the area of contact ($a^{*2}\pi = 0.005 \cdot 10^{-6}$ m²).

List of Symbols

a	half width of the wear track, mm
a^*	radius of a Hertzian contact area, mm
A_{wt}	surface of the wear track after rubbing, mm ²
A_w	surface of the wafer, mm ²
b	half length of the wear track, mm
B'	high field constant, nm/V
c_i	concentration of the species i , mol/m ³
c_{part}	concentration of the silica particles in the CMP slurries, g/l
C_{met}	atomic concentration of W in the metal, mol/m ³
C_{ox}	atomic concentration of W in the passive oxide film, mol/m ³
COF	coefficient of friction
d	width of the wear track, μm
d_{sep}	separation distance between the wafer and the pad during polishing under pressure, μm
D_B	coefficient of diffusion, m ² /s
E	electrode potential, V
E_b	transpassivation potential, V
E_{cor}	corrosion potential, V
E_p	passivation potential, V
E_{rev}	equilibrium potential, V

List of Symbols

E_{Ω}	potential drop due to ohmic resistance, mV
E^*	effective Young's modulus, GPa
f	frequency of rubbing, Hz
F	Faraday's constant, C/mol
F_n	applied normal load, N
F_t	friction force, N
$F_{n_{CMP}}$	applied normal load in CMP, N
H	micro hardness out of the wear track, GPa
H_{CMP}	micro hardness in the CMP, GPa
H_s	hardness of the softer of the two materials in contact, GPa
H_{wt}	micro hardness in the wear track, GPa
i	current density, mA/cm ²
i_a	anodic partial current density, mA/cm ²
i_c	cathodic partial current density, mA/cm ²
i_l	anodic limiting current density, mA/cm ²
i_0'	current parameter, mA/cm ²
i_{diss}	ionic current density corresponding to metal-ion dissolution, mA/cm ²
i_{gr}	current density leading to film growth, mA/cm ²
i_{peak}	peak current density, mA/cm ²
I	overall measured current during rubbing, mA
I_{mt}	current enhancement due to stirring of the solution by the ball, mA
I_O	AES oxygen intensity
I_p	repassivation current, mA

List of Symbols

I_{peak}	peak current, maximal current in passivation transients measurements, mA
I_r	current enhancement due to rubbing (excess current), mA
I_w	AES tungsten intensity
I_{wac}	current generated in the wear track by wear accelerated corrosion, mA
$I_{wac_{CMP}}$	current generated by wear accelerated corrosion in CMP, mA
$I_{wac_{CMP,th}}$	theoretical current generated by wear accelerated corrosion in CMP, mA
$I_{wac_{max}}$	maximum wear accelerated corrosion current in the wear track, mA
$I_{wac_{th}}$	theoretical current generated by wear accelerated corrosion, mA
k_1	fraction of the wear track area becoming effectively depassivated
k_2	probability that asperity contact takes place on an area already depassivated by another asperity
k_L	oxidation rate constant
k_w	wear coefficient
$K_{st_{CMP}}$	proportionality factor in CMP
K_p	Preston's coefficient
K_{st}	proportionality factor
l	length of the wear track, mm
l_{sl}	sliding distance, mm
L	passive oxide film thickness, nm
L_{crit}	critical thickness of the oxide layer, nm
n	charge number for the oxidation reaction
n_a	number of asperity contacts determined by the roughness of the rigid body
n_{part}	number of particles contributing to the depassivation of the wafer surface

List of Symbols

n'_{part}	number of particles in the volume of the slurry V_{ml}
n''_{part}	number of particles in the volume of the slurry V_{CMP}
m_{ml}	mass of all silica particles in the V_{ml} slurry volume, g
m_{part}	mass of a single silica particle, g
M	molar mass, g/mol
P	applied downward pressure in CMP, Pa
r_{cc}	distance of the centers of the wafer and pad, mm
r_{part}	radius of the silica particle, nm
R	peak area ratio between metallic and oxidized W signal in the W_{4f} spectrum
R_a	arithmetic average surface roughness, μm
R_{dep}	rate of generation of depassivated area (depassivation rate), mm^2/s
$R_{dep_{CMP}}$	depassivation rate in CMP, mm^2/s
$R_{dep_{max}}$	maximum depassivation rate, mm^2/s
RR	removal rate in CMP, $\text{\AA}/\text{min}$
R_{Ω}	ohmic resistance, Ω
Q	electric charge, mC
Q_p	passivation charge density, $\mu\text{C}/\text{mm}^2$
$Q_{p_{CMP}}$	passivation charge density for the technical CMP slurries, $\mu\text{C}/\text{mm}^2$
$Q_{p_{CMP}}^*$	passivation charge density necessary for the repassivation of the surface activated by the single particle in the CMP, mC/mm^2
S_{part}	linear distribution of particles contributing the surface depassivation, mm
t	duration of rubbing, s

List of Symbols

t_{CMP}	duration of CMP polishing tests, s
t_{part}	time between two depassivation actions of one particle, s
$t_{WO_3}^{AES}$	sputtering time estimated at the half height of oxygen atomic content, min
T	temperature, °C
v_s	sliding velocity, mm/s
v_{sCMP}	linear velocity of any point on the wafer, mm/s
V	linear velocity of the wafer relative to the polishing pad, mm/s
V_{ch}	volume of metal transformed by anodic oxidation (according to [1]), mm ³
V_{CMP}	slurry volume between the wafer and the pad, dm ³
V_{ml}	slurry volume corresponding to the thickness of the monolayer of the particles near the wafer surface, dm ³
V_m	mechanical wear volume, mm ³
V_{ox}	specific oxide volume, cm ³ /mol
V_{part}	volume of the single silica particle, cm ³
V_w	wear rate (Archard's law), m ³ /s
V_{wac}	metal volume removed by anodic oxidation in the wear track, mm ³
V_{wacCMP}	volume of wear accelerated corrosion in the CMP process, mm ³
V_{wt}	wear track volume, mm ³
WR	tribocorrosion wear rate, Å/min
y	mean depth of the wear track, μm
δ	thickness of the Nernst diffusion layer, μm
Θ	escape angle with respect to the surface normal, °

List of Symbols

λ_{met}	electron mean free path in the metallic tungsten, nm
λ_{ox}	electron mean free path in the tungsten oxide, nm
μ	coefficient of friction
κ	electrolyte conductivity, mS/cm
ρ	density, g/cm ³
σ_{met}	photo-electron cross section in the metallic tungsten, m ² /atom
σ_{ox}	photo-electron cross section in the tungsten oxide, m ² /atom
ν	Poisson's ratio
$V_{Ta_2O_5}$	sputtering rate of Ta ₂ O ₅ , Å/min
Φ	electric potential, V
ω	angular velocity, rad/s
ω_T	rotation rate of the platen holding the pad, rpm

Curriculum Vitae

Jelena STOJADINOVIĆ

Born May 15, 1974 in Kragujevac, Serbia

- 2005 – 2009 Doctoral student and assistant in the Laboratory of Metallurgical Chemistry at the Swiss Federal Institute of Technology, Lausanne (EPFL) – *Switzerland*, under the supervision of Dr. Stefano Mischler
- 2004 – 2005 Industrial Marketing Manager at Interdrvo and Ema Knić, *Serbia*
- 2004 M.Sc. of Technical Sciences, field Tribology, Faculty of Mechanical Engineering, University of Kragujevac, *Serbia*
- 2002 – 2004 Project Research and Design Engineer at Zastava Arms, Research and Development, Kragujevac, *Serbia*
- 1998 – 2001 Assistant Researcher, Centre of Tribology, Faculty of Mechanical Engineering, University of Kragujevac, *Serbia*
- 1998 B.Sc. (recognized as M.Sc. of Technical Sciences since 2007 according to Bologna convention), field Energy and Process Engineering, Faculty of Mechanical Engineering, University of Kragujevac, *Serbia*

